

INFORMATION TO USERS

This manuscript has been reproduced from the microfilm master. UMI films the text directly from the original or copy submitted. Thus, some thesis and dissertation copies are in typewriter face, while others may be from any type of computer printer.

The quality of this reproduction is dependent upon the quality of the copy submitted. Broken or indistinct print, colored or poor quality illustrations and photographs, print bleedthrough, substandard margins, and improper alignment can adversely affect reproduction.

In the unlikely event that the author did not send UMI a complete manuscript and there are missing pages, these will be noted. Also, if unauthorized copyright material had to be removed, a note will indicate the deletion.

Oversize materials (e.g., maps, drawings, charts) are reproduced by sectioning the original, beginning at the upper left-hand corner and continuing from left to right in equal sections with small overlaps.

Photographs included in the original manuscript have been reproduced xerographically in this copy. Higher quality 6" x 9" black and white photographic prints are available for any photographs or illustrations appearing in this copy for an additional charge. Contact UMI directly to order.

Bell & Howell Information and Learning
300 North Zeeb Road, Ann Arbor, MI 48106-1346 USA
800-521-0600





FAST ELECTROMAGNETIC MODELING OF MULTILAYER
MICROSTRIP ANTENNAS AND CIRCUITS

BY
FENG LING

B. S., Nanjing University of Science and Technology, 1993
M. S., Nanjing University of Science and Technology, 1996

THESIS

Submitted in partial fulfillment of the requirements
for the degree of Doctor of Philosophy in Electrical Engineering
in the Graduate College of the
University of Illinois at Urbana-Champaign, 2000

Urbana, Illinois

UMI Number: 9971123

UMI[®]

UMI Microform 9971123

**Copyright 2000 by Bell & Howell Information and Learning Company.
All rights reserved. This microform edition is protected against
unauthorized copying under Title 17, United States Code.**

**Bell & Howell Information and Learning Company
300 North Zeeb Road
P.O. Box 1346
Ann Arbor, MI 48106-1346**

UNIVERSITY OF ILLINOIS AT URBANA-CHAMPAIGN

THE GRADUATE COLLEGE

JANUARY 2000

(date)

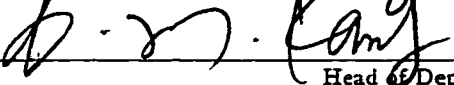
WE HEREBY RECOMMEND THAT THE THESIS BY

FENG LING

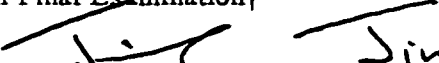
ENTITLED **FAST ELECTROMAGNETIC MODELING OF
MULTILAYER MICROSTRIP ANTENNAS AND CIRCUITS**

BE ACCEPTED IN PARTIAL FULFILLMENT OF THE REQUIREMENTS FOR
THE DEGREE OF **DOCTOR OF PHILOSOPHY**

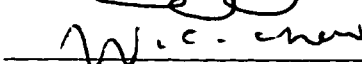
 Jin
Director of Thesis Research

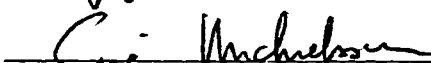
 Feng
Head of Department

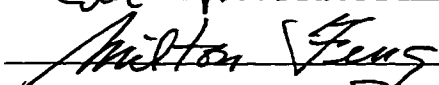
Committee on Final Examination†

 Jin
Chairperson









† Required for doctor's degree but not for master's.

ABSTRACT

Rigorous full-wave electromagnetic modeling techniques play a significant role in the design of integrated circuits (ICs). The integral equation-based method is very attractive to deal with the ICs in a multilayer medium environment.

In this thesis, the method of moments (MoM) solution of multilayer microstrip antennas and circuits is presented. The multilayer Green's functions are evaluated by the discrete complex image method (DCIM). The surface-wave contribution is extracted recursively by a novel multilevel contour integral in the complex k_p plane. An interpolation scheme is employed to further reduce the computer time to calculate the Green's functions. The higher-order interpolatory basis functions defined on curvilinear triangular elements are applied. The curvilinear triangular elements provide great flexibility to discretize arbitrary shapes. The higher-order basis functions offer a better convergence rate than does the lower-order ones.

To achieve the fast frequency sweep, the model-order reduction technique is incorporated into this MoM analysis, in which the asymptotic waveform evaluation (AWE) is employed to obtain the Padé approximant at an expansion point. A binary search scheme is developed to automatically determine locations of expansion points.

To handle large-scale problems, two fast algorithms have been applied. One is the fast Fourier transform (FFT) accelerated algorithm. This method can be traced back to the well-known conjugate gradient FFT (CGFFT) method, which is restricted to the uniform discretization. To overcome this limitation, the adaptive integral method (AIM) is proposed, which retains the advantages of the CGFFT method as well as the excellent modeling capability offered by the triangular elements. The other fast algorithm is the multilevel fast multipole algorithm (MLFMA), which is combined with the DCIM for an efficient analysis of microstrip structures. Both of the algorithms reduce the computational complexity to $O(N \log N)$.

With these techniques together, a fast integral equation solver for microstrip structures in multilayer media is developed. Examples of circuits and antennas are presented to demonstrate the accuracy and efficiency of this solver.

To my parents

ACKNOWLEDGMENTS

Foremost, I would like to thank my thesis advisor, Professor Jianming Jin. He has been a constant source of advice and motivation since the day I came here. Without his support, this thesis would not have been possible.

I would also like to thank Professor Weng Cho Chew for establishing the stimulating laboratory environment in which I completed my research and for always making himself available for my questions. My appreciation also goes to Professors Andreas Cangellaris, Shun-Lien Chuang, Milton Feng, Eric Michielssen, and Jose Schutt-Aine for their time and valuable suggestions. I could not have gotten this far without Professor Da-Gang Fang at Nanjing University of Science and Technology, who introduced me to the realm of electromagnetics.

I would like to thank all my colleagues at the Center for Computational Electromagnetics and the Electromagnetics Laboratory. You know who you are. Thanks to all of you for your friendship. In particular, I thank Dr. Jiming Song, Dr. Chao-Fu Wang, Kalyan Donepudi, Bin Hu, Dan Jiao, and Jian Liu, who have worked closely with me and whose contributions have enhanced a number of the sections of this thesis.

I also wish to thank Dr. Can-Yun Wang at Schlumberger-Doll Research and Dr. Sharad Kapur and Dr. David E. Long at Bell Labs for mentoring me in the course of my internships.

My deepest gratitude goes to my greatest source of support: my wife, Jun. For her love and confidence I am most grateful.

TABLE OF CONTENTS

CHAPTER	PAGE
1 OVERVIEW	1
2 GREEN'S FUNCTIONS FOR MULTILAYER MEDIA	6
2.1 Introduction	6
2.2 Spectral Domain Green's Functions for Electric and Magnetic Fields	7
2.3 Spectral Domain Green's Functions for Potentials	11
2.4 Discrete Complex Image Method	13
2.5 Green's Function Interpolations	19
2.6 Transmission Line Green's Functions	21
2.7 Conclusion	24
3 MOM SOLUTION FOR MULTILAYER MICROSTRIP STRUCTURES	25
3.1 Introduction	25
3.2 MPIE Formulation	25
3.3 Excitation and Parameter Extraction	29
3.4 Numerical Results	30
3.4.1 Convergence behavior of higher-order methods	30
3.4.2 Antenna and circuit examples	31
3.5 Conclusion	38
4 REDUCED-ORDER MODEL	40
4.1 Introduction	40
4.2 AWE Implementation	41
4.3 Numerical Results	42
4.4 Conclusion	47
5 ADAPTIVE INTEGRAL METHOD	48
5.1 Introduction	48
5.2 AIM Formulation	49
5.3 Accuracy and Complexity	52
5.4 Numerical Results	52

5.5 Conclusion	60
6 MULTILEVEL FAST MULTIPOLE ALGORITHM	61
6.1 Introduction	61
6.2 FMM Formulation	62
6.3 Numerical Results	63
6.4 Conclusion	66
7 SUMMARY AND FUTURE WORK	67
REFERENCES	69
VITA	82

LIST OF TABLES

TABLE		PAGE
2.1 Two decoupled sets of transmission line equations in (u, v, z) coordinates		10
4.1 Comparison of the CPU time using the direct calculation and AWE		43

LIST OF FIGURES

FIGURE	PAGE
2.1 A multilayer medium with source and field points in layer m and layer n , respectively, and its transmission line representation.	7
2.2 Coordinate rotation from (x, y) to (u, v)	9
2.3 Magnitude of \tilde{G}^Φ in the first and fourth quadrants of the complex k_ρ -plane for a five-layer medium. The frequency is 30 GHz. Unit for thickness is mm.	16
2.4 Magnitude of \tilde{G}^Φ in the first and fourth quadrants of the complex k_ρ -plane for a shield three-layer medium. The frequency is 20 GHz. Unit for thickness is mm.	17
2.5 Magnitude of Green's functions G_{xx}^A and G^Φ for a five-layer medium. The frequency is 30 GHz. Unit for thickness is mm. (a) $z' = 0.4, z = 1.4$. (b) $z' = 0.4, z = 0.4$	18
2.6 Magnitude of Green's functions, G_{xx}^A , G_{zz}^A , G_{xz}^A , and G^Φ for a five-layer medium. The frequency is 30 GHz. Unit for thickness is mm. (a) $z' = 0.4, z = 1.4$. (b) $z' = 0.4, z = 0.4$	20
2.7 Magnitude of Green's functions, G_{xx}^A , G_{zz}^A , G_{xz}^A , and G^Φ for a shielded three-layer medium. The frequency is 20 GHz. $z = z' = 0.762$. Unit for thickness is mm.	21
3.1 A curvilinear patch in (x, y, z) and (ξ_1, ξ_2, ξ_3) coordinates.	26
3.2 The zeroth-order basis function.	28
3.3 The first-order basis function.	28
3.4 Convergence behavior of the high-order basis function. (a) Relative error versus number of unknowns. (b) CPU time versus number of unknowns.	31
3.5 Backscatter RCS ($\sigma_{\theta\theta}$) versus frequency for a rectangular microstrip patch antenna. $L = 36.6$ mm, $W = 26$ mm, $h = 1.58$ mm, $\epsilon_r = 2.17$, $\theta^i = 60^\circ$, $\phi^i = 45^\circ$	32
3.6 S-parameters of a microstrip periodic filter. $\epsilon_r = 10.5$, $h = 0.635$ mm. The line width is 0.686 mm. The patch size is 2.54 mm \times 2.54 mm. The spacing is 5.08 mm.	33

3.7 Input impedance for a proximity-coupled microstrip antenna. $\epsilon_{r1} = 1.0$, $\epsilon_{r2} = \epsilon_{r3} = 2.62$, $h_2 = h_3 = 1.59$ mm, $w = 4.372$ mm, $c = 17.5$ mm, $d = 17.5$ mm. The frequency is from 2.80 GHz to 3.15 GHz with increment 0.05 GHz.	34
3.8 Current distributions and S-parameters of microstrip meander line. $\epsilon_r = 9.978$, $h = 0.635$ mm. The line width is 0.61 mm. The gap is 0.305 mm wide and 2.44 mm deep.	35
3.9 S-parameters for a branch line coupler (dimensions in mm). $\epsilon_r = 2.2$, $h = 0.794$ mm.	36
3.10 S-parameters of an annular-ring power-divider. $\epsilon_r = 2.2$, $h = 0.79$ mm. The line width is 2.4 mm. The inner and outer radii of the annular ring are 1.5 mm and 7.2 mm, respectively. The angle between port 1 and port 2 is 60°.	37
3.11 S-parameters of a spiral inductor. $\epsilon_r = 9.6$, $h = 2.0$ mm. The line widths and spacings are all 2.0 mm. The height and the span of the air bridges are 1.0 mm and 6.0 mm, respectively.	38
3.12 S-parameters of a spiral inductor. $\epsilon_r = 9.8$, $h = 0.635$ mm.	39
4.1 Current distributions and S-parameters for a microstrip double-stub. $\epsilon_r = 9.9$, $h = 0.127$ mm. The line width is 0.122 mm. The stub length is 2.921 mm. The spacing between two stubs is 0.757 mm.	44
4.2 Current distributions and S-parameters for a two-port asymmetric antenna.	45
4.3 S-parameters for an overlap-gap-coupled microstrip filter. $\epsilon_{r1} = 1.0$, $\epsilon_{r2} = 9.8$, $\epsilon_{r3} = 2.2$, $h_2 = h_3 = 0.01$, $l_1 = 0.2752$, $l_2 = 0.2542$, $l_3 = 0.2851$, $x_1 = 0.0516$, $x_2 = 0.0152$, $x_3 = 0.0106$. Unit of dimension: inch.	46
5.1 Translation of RWG basis functions to rectangular grids. The highlighted triangular basis function on the left is approximated by $(M + 1)^2 = 9$ rectangular grids. The highlighted triangular basis function on the right is approximated by $(M + 1)^2 = 16$ rectangular grids.	50
5.2 Matrix elements Z_{Ij} ($j = 1, 2, \dots, 80$) calculated by the conventional MoM and the AIM.	53

5.3 Complexity of the AIM. The CPU time per iteration is close to $9 \times 10^{-6}N \log N$ and the memory requirement is close to $7 \times 10^{-3}N$.	54
5.4 Current distributions and S-parameters for the radial stub. $\epsilon_r = 10.0$, $h = 0.635$ mm, width = 0.6 mm, radius = 5.0 mm, and angle = 60°. (a) Current distribution at $f = 8.0$ GHz. (b) Current distribution at $f = 11.0$ GHz. (c) S-parameters.	55
5.5 Current distributions and S-parameters for the parallel-coupled band-pass filter. $\epsilon_r = 10.0$, $h = 0.635$ mm. (a) Current distribution at $f = 9.0$ GHz. (b) Current distribution at $f = 11.0$ GHz. (c) S-parameters.	56
5.6 Current distributions and S-parameters for the cascaded microstrip radial stub. $\epsilon_r = 10.0$, $h = 0.635$ mm. The spacing between stubs is 7.5 mm. (a) Current distribution at $f = 9.0$ GHz. (b) Current distribution at $f = 11.0$ GHz. (c) S-parameters.	57
5.7 Current distribution and radiation patterns of the corporate-fed microstrip antenna array. $\epsilon_r = 2.2$, $h = 1.59$ mm, $l = 10.08$ mm, $w = 11.79$ mm, $d_1 = 1.3$ mm, $d_2 = 3.93$ mm, $l_1 = 12.32$ mm, $l_2 = 18.48$ mm, $D_1 = 23.58$ mm, $D_2 = 22.40$ mm. (a) Current distribution at $f = 9.42$ GHz. (b) $\phi = 0^\circ$. (c) $\phi = 90^\circ$.	58
5.8 Backscatter RCS ($\sigma_{\theta\theta}$) for microstrip antenna arrays with various sizes as a function of frequency.	59
6.1 Matrix elements Z_{lj} ($j = 1, 2, \dots, 80$) calculated by the conventional MoM and the MLFMA.	64
6.2 Complexity of the MLFMA. The CPU time per iteration is close to $9 \times 10^{-6}N \log N$ and the memory requirement is close to $7 \times 10^{-3}N$.	65
6.3 Radiation patterns of the corporate-fed microstrip antenna array. $\epsilon_r = 2.2$, $h = 1.59$ mm, $l = 10.08$ mm, $w = 11.79$ mm, $d_1 = 1.3$ mm, $d_2 = 3.93$ mm, $l_1 = 12.32$ mm, $l_2 = 18.48$ mm, $D_1 = 23.58$ mm, $D_2 = 22.40$ mm. $f = 9.42$ GHz.	65

CHAPTER 1

OVERVIEW

In the past decades, integrated circuits (ICs) have undergone impressive advancements. Planar passive components are extensively used in IC systems, such as IC packages, printed circuit boards (PCBs), and multichip module (MCM) interconnections. Accurate electromagnetic (EM) analysis of the planar components becomes very important because it provides accurate models for the IC design.

To develop a reliable computer-aided design (CAD) tool for this purpose, several aspects have to be considered. First, with the increased complexity of those structures, multilayer media are often employed to allow more versatile designs. This fact necessitates that the modeling be capable of dealing with planar components in multilayer media. Second, as the operating frequency of ICs increases, the empirical formulas and quasi-static models are unable to provide accurate results. Consequently, it is desirable to develop a rigorous full-wave EM modeling. Third, the ability to tackle electrically large problems becomes necessary to perform the integrated simulation.

There have been a variety of full-wave EM methods developed to accomplish the goal mentioned above, and these methods can be divided into two broad classes: the differential equation approach and the integral equation approach. The differential equation approach includes finite difference time domain (FDTD) [1]–[8], and finite element method (FEM) [9]–[12]. In the integral equation approach, the method of moments (MoM) is employed to solve the integral equation [13]–[54]. The integral equation approach is more attractive for multilayer medium problems since the method allows one to apply Green’s theorem to reduce volume integrals to surface integrals, thus reducing the matrix dimension significantly because of the use of surface discretization rather than volume discretization. Different variations of this method have been implemented and investigated. The MoM analysis can be carried out either in the spectral domain [13]–[32] or the spatial domain [37]–[54]. In the spectral domain MoM, the Green’s function can be analytically derived by using the spectral domain approach (SDA) [34], [35]. This approach is often applied to

regularly shaped structures since the basis functions are usually chosen to be those that have analytical Fourier transforms, such as the roof-top and piece-wise sinusoidal basis functions, although the Fourier transform of triangular basis function is also available [33]. The drawback of this approach is the time-consuming evaluation of the double infinite integration to generate the impedance matrix. However, when this approach is employed to deal with shielded structures [26]–[32] or periodic structures, the double integral is replaced by the double summation. The efficiency of this approach can be improved by using the fast Fourier transform (FFT) [28]–[32].

In contrast, the spatial domain MoM provides better physical insight since the problem remains in the physical domain. The basis functions can be arbitrary, which renders the approach very versatile. The efficiency of this approach depends on the evaluation of the spatial Green’s function, which is expressed in terms of the Sommerfeld integral (SI). Generally speaking, the analytical solution of the SI is not available, and the numerical integration is time consuming since the integrand is both highly oscillating and slowly decaying. Several efficient techniques have been proposed to speed up this numerical integration [39]. The scheme that employs the tabulation and interpolation techniques is popularly used [44], [45], [50], [53]. To further accelerate the computation, several approaches have been developed, such as the fast Hankel transform (FHT) approach [52]–[54], the steepest-descent path (SDP) approach [55], the window function approach [56], and the discrete complex image method (DCIM) [57]–[66].

In this work, we employ the spatial domain MoM. The evaluation of Green’s functions and the choice of basis functions are crucial to obtaining an accurate and efficient solution. Chapter 2 addresses the efficient evaluation of Green’s functions. First, the spectral domain Green’s functions for multilayer media is derived from a simple transmission line perspective. Then, the DCIM is employed to efficiently evaluate the SIs, resulting in closed form spatial domain Green’s functions. The controversial issue of surface-wave extraction is discussed. For the far-field Green’s functions, it is necessary to extract surface waves to approximate $1/\sqrt{\rho}$ asymptotic behavior. In the previous work of the DCIM, the surface-wave contribution is treated analytically by using residue calculus, which makes it difficult to extend to multilayer cases. Here, the surface-wave contribution is obtained by performing the contour integral recursively in the complex k_ρ plane [121]. Finally, to make the Green’s function evaluation more efficient, especially for 3-D structures, the interpolation scheme is employed, which is able to restore the Green’s function at the same order

of time as that in free-space problems.

In Chapter 3, the choice of basis functions is discussed. Traditional numerical modeling employs roof-top functions for rectangular discretization or Rao-Wilton-Glisson (RWG) functions [73] for triangular discretization. These functions are complete to the zeroth order. As a result, a very fine discretization is often required to yield an accurate solution. This leads to a large matrix equation, which is expensive to solve. In addition, the numerical solution converges slowly to the exact one when the discretization is made finer. As a solution to this problem, the interpolatory higher-order basis functions defined on the curvilinear discretization [75] are employed, which have a better convergence rate and can yield an accurate solution with a rather coarse discretization. Combining the higher-order basis functions with the DCIM yields an efficient and accurate MoM analysis. Several scattering, radiation, and circuit problems are investigated in Chapter 3.

In many cases, frequency responses of microstrip structures are needed over a wide frequency band. Using the frequency domain-based method, we have to repeat the calculation at each frequency. This can be computationally intensive for devices with complicated frequency responses. To rapidly evaluate the frequency response over a band of interest, a reduced-order model is presented in Chapter 4. In this work, asymptotic waveform evaluation (AWE) [85] is employed to obtain the Padé approximant at the expansion point. Then, the frequency response near the expansion point can be easily obtained. In some cases, one expansion point is not enough, so a simple binary search algorithm, as done in [89], is employed to automatically determine the expansion points and obtain the accurate solution over the entire broadband. The numerical results show that the method using AWE is 8 to 22 times faster than the direct calculation.

To simulate large-scale problems, it is often necessary to employ a large number of unknowns. This MoM algorithm becomes prohibitive even on the most powerful computers because the memory requirement of this algorithm is proportional to $O(N^2)$, where N denotes the number of unknowns, and the direct matrix inversion solver requires $O(N^3)$ floating-point operations. Even when an iterative solver such as the conjugate gradient (CG) method is employed for solving the MoM matrix equation, the operation count is $O(N^2)$ per iteration because of the need to evaluate the matrix-vector product. This operation count is too high for an efficient simulation.

To make the iterative method more efficient, we have to rapidly evaluate the matrix-vector multiplication. Three fast schemes have been proposed in the past.

One is the FFT-accelerated scheme [95]–[107]. When this is combined with the CG method, the resulting algorithm is called the conjugate gradient fast Fourier transform (CGFFT) method [95]–[103], in which the memory requirement is of $O(N)$ and the CPU time per iteration is of $O(N \log N)$. However, CGFFT requires a uniform discretization to make use of the translational invariance of the Green’s functions. This limits the applicability of the method to complex geometries. The method to alleviate this problem is the adaptive integral method (AIM) [104], [105], which retains the advantages of the CGFFT method as well as the excellent modeling capability offered by the RWG basis functions. Similar approaches include the sparse-matrix/canonical grid method [108] and the precorrected-FFT method [109].

Another fast scheme is the multipole-accelerated scheme, which is originally proposed to evaluate particle simulations [110] and later extended to solve electromagnetic problems [111]–[115]. Some successful examples using this technique include Fastcap [111], which applies the fast multipole method (FMM) to extract capacitance for objects in homogeneous media, and FISC (Fast Illinois Solver Code) [115], which uses the multilevel fast multipole algorithm (MLFMA) to deal with free-space scattering problems. Because the FMM is derived from the free-space Green’s function, its extension to microstrip problems is not straightforward. One approach is to combine the FMM with the DCIM [117]–[119]. In [117] and [118], the equivalent problem is set up by adding N_c images at the corresponding complex coordinates, and therefore, represented by $N(N_c+1)$ basis functions. In the FMM implementation, the translation is different for different images. Also, static problems and 2-D problems are treated in [117] and [118], respectively. In [119], both the 2-D and 3-D FMMs are employed, one is applied to the surface-wave part and the other to the complex image part. The multilevel algorithm is not implemented in those analyses. The other FMM approach is to express the Green’s function in terms of a rapidly converging steepest descent integral, and evaluate the Hankel function arising in the integrand by the FMM [120], [121].

The third fast scheme is the singular value decomposition (SVD) based integral equation solver for 3-D problems (IES³) [122], [123]. Unlike the kernel-specific algorithms such as the FMM, this method does not depend on a particular form of Green’s function. However, it does require the kernel to be asymptotically smooth.

In this thesis, both the AIM and FMM are investigated and extended to microstrip structures. In Chapter 5, the AIM is successfully extended with the aid of the DCIM [107]. The resulting algorithm has the memory requirement scaled as $O(N)$ and CPU

time per iteration scaled as $O(N \log N)$. In Chapter 6, the MLFMA combined with the DCIM is presented for efficient analysis of microstrip structures. Instead of being treated separately, the image sources are grouped with the original source. By the use of the multilevel algorithm, the complexity is reduced to $O(N \log N)$. The algorithm requires little extra computation compared with that applied to free-space problems.

CHAPTER 2

GREEN'S FUNCTIONS FOR MULTILAYER MEDIA

2.1 Introduction

The method of moments (MoM) solution of integral equations has received intense attention to tackle the multilayer medium problems. In this method, the evaluation of Green's functions and the choice of basis functions are crucial to obtaining an accurate and efficient solution.

In this chapter, the discrete complex image method (DCIM) is presented to evaluate the Green's functions for multilayer media. The basic idea of the DCIM is to approximate the spectral kernel of a Green's function by a sum of complex exponentials extracted using either the Prony method or the generalized pencil-of-function (GPOF) method [67]. Then, the Sommerfeld integral (SI) is evaluated in closed forms via the Sommerfeld identity. This method has been extensively employed to analyze microstrip structures. However, most of the work is confined to single-layered or double-layered structures since the surface-wave contribution has to be extracted analytically using residue calculus, which makes the DCIM difficult to extend to multilayer media. Therefore, to use the DCIM for multilayer media, the surface waves are often not extracted [62]. This approximation is only valid for the thin multilayer configurations, where the surface-wave contribution is insignificant. However, for general multilayer media with a strong surface-wave contribution, the lack of the surface-wave extraction often results in errors in the far-field region since the surface waves behave in the manner of cylindrical waves and it is physically inappropriate to approximate such waves by spherical waves. For a general-purpose algorithm, especially for the MoM analysis of electrically large structures, the surface waves have to be extracted. In this work, the surface-wave extraction is carried out numerically by doing a multilevel contour integral in the complex k_p plane [121].

This chapter is organized as follows. First, the spectral domain Green's functions for multilayer media are derived by using the transmission line analogy. Then, the DCIM is employed to efficiently evaluate the SIs, resulting in closed form spatial domain Green's functions. The surface-wave extraction is performed by the contour

integral in the complex k_p plane. Finally, the interpolation scheme is presented to further reduce the evaluation time in the MoM analysis.

2.2 Spectral Domain Green's Functions for Electric and Magnetic Fields

Consider a general multilayer medium, as shown in Fig. 2.1. The medium is assumed to be laterally infinite. Layer i is characterized by relative permittivity ϵ_{ri} , relative permeability μ_{ri} , and conductivity σ_i . In the following formulations, ϵ_{ri} is the effective relative permittivity $\epsilon_{ri} + \frac{\sigma_i}{j\omega\epsilon_0}$, which includes the effect of the finite conductivity.

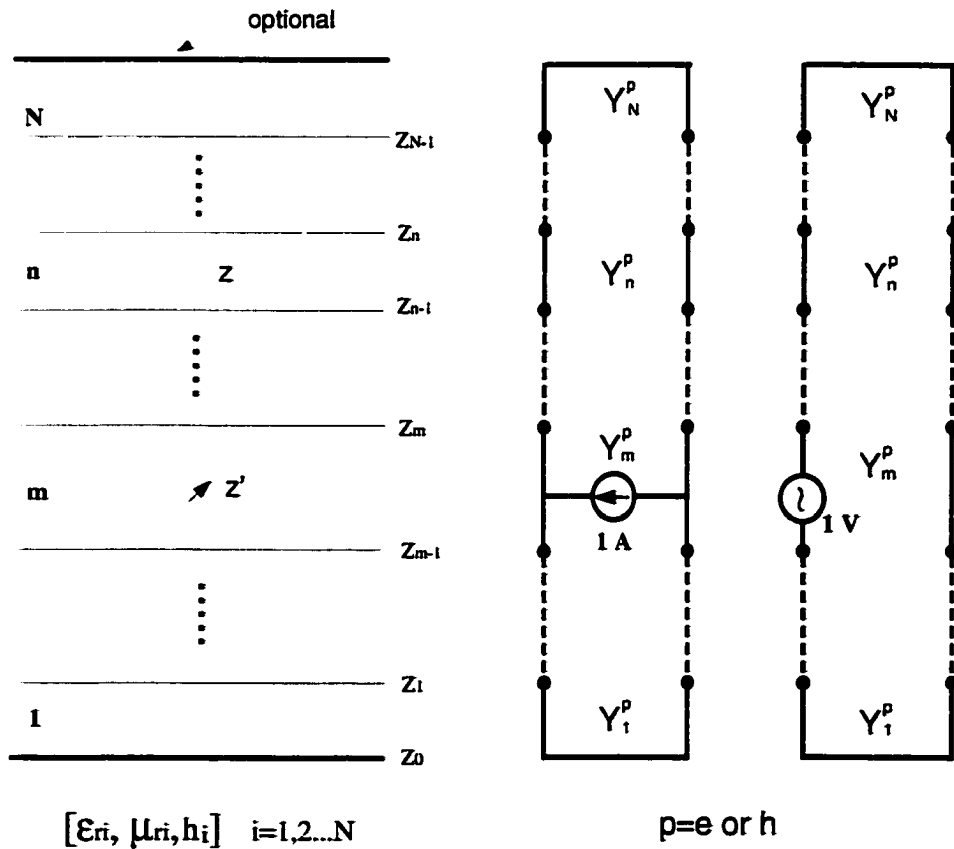


Figure 2.1 A multilayer medium with source and field points in layer m and layer n , respectively, and its transmission line representation.

The fields (\mathbf{E}, \mathbf{H}) due to a specified current (\mathbf{J}, \mathbf{M}) are governed by Maxwell's

equations

$$\begin{aligned}\nabla \times \mathbf{E} &= -j\omega\mu_0\mu_r\mathbf{H} - \mathbf{M} \\ \nabla \times \mathbf{H} &= j\omega\epsilon_0\epsilon_r\mathbf{E} + \mathbf{J}\end{aligned}\quad (2.1)$$

The technique most often used is to formulate the problem in the transformed spectral domain, in which the transverse and longitudinal components are decomposed and the transverse coordinate $\rho = \hat{x}x + \hat{y}y$ is replaced by the spectral counterpart $\mathbf{k}_\rho = \hat{x}k_x + \hat{y}k_y$, according to the Fourier transform

$$\tilde{g}(\mathbf{k}_\rho, z) = \int_{-\infty}^{\infty} \int_{-\infty}^{\infty} g(\rho, z) e^{j\mathbf{k}_\rho \cdot \rho} dx dy \quad (2.2)$$

$$g(\rho, z) = \frac{1}{(2\pi)^2} \int_{-\infty}^{\infty} \int_{-\infty}^{\infty} \tilde{g}(\mathbf{k}_\rho, z) e^{-j\mathbf{k}_\rho \cdot \rho} dk_x dk_y \quad (2.3)$$

As we will see later, the Fourier transform pair can be expressed as the Fourier-Bessel transform pair

$$\tilde{g}(\mathbf{k}_\rho, z) = \frac{1}{2\pi} \int_0^{\infty} g(\rho, z) J_0(k_\rho \rho) \rho d\rho \quad (2.4)$$

$$g(\rho, z) = \frac{1}{2\pi} \int_0^{\infty} \tilde{g}(\mathbf{k}_\rho, z) J_0(k_\rho \rho) k_\rho dk_\rho \quad (2.5)$$

by introducing the Bessel function

$$J_0(k_\rho \rho) = \frac{1}{2\pi} \int_0^{2\pi} e^{-jk_\rho \rho} d\alpha, \quad \mathbf{k}_\rho = \hat{x}k_\rho \cos\alpha + \hat{y}k_\rho \sin\alpha \quad (2.6)$$

We can rewrite Maxwell's equations as [71]

$$\frac{d}{dz} \tilde{\mathbf{E}}_\rho = \frac{1}{j\omega\epsilon_0\epsilon_r} (k_0^2 \mu_r \epsilon_r - \mathbf{k}_\rho \mathbf{k}_\rho \cdot) (\tilde{\mathbf{H}}_\rho \times \hat{z}) + \frac{\tilde{J}_z}{\omega\epsilon_0\epsilon_r} \mathbf{k}_\rho - \tilde{\mathbf{M}}_\rho \times \hat{z} \quad (2.7)$$

$$\frac{d}{dz} \tilde{\mathbf{H}}_\rho = \frac{1}{j\omega\mu_0\mu_r} (k_0^2 \mu_r \epsilon_r - \mathbf{k}_\rho \mathbf{k}_\rho \cdot) (\hat{z} \times \tilde{\mathbf{E}}_\rho) + \frac{\tilde{M}_z}{\omega\mu_0\mu_r} \mathbf{k}_\rho - \hat{z} \times \tilde{\mathbf{J}}_\rho \quad (2.8)$$

$$-j\omega\epsilon_0\epsilon_r \tilde{E}_z = j\mathbf{k}_\rho \cdot (\tilde{\mathbf{H}}_\rho \times \hat{z}) + \tilde{J}_z \quad (2.9)$$

$$-j\omega\mu_0\mu_r \tilde{H}_z = j\mathbf{k}_\rho \cdot (\hat{z} \times \tilde{\mathbf{E}}_\rho) + \tilde{M}_z \quad (2.10)$$

If the spectral domain transverse components in the (x, y) coordinate are rotated by an angle α to the new coordinate (u, v) , as shown in Fig. 2.2,

$$\begin{bmatrix} \hat{u} \\ \hat{v} \end{bmatrix} = \begin{bmatrix} \cos\alpha & \sin\alpha \\ -\sin\alpha & \cos\alpha \end{bmatrix} \begin{bmatrix} \hat{x} \\ \hat{y} \end{bmatrix}, \quad \cos\alpha = \frac{k_x}{k_\rho}, \quad \sin\alpha = \frac{k_y}{k_\rho}, \quad (2.11)$$

then, we obtain two decoupled sets of transmission line equations, as shown in Table 2.1. \tilde{E}_u, \tilde{H}_v can be interpreted as voltage and current (V^e, I^e) on a transverse magnetic (TM) transmission line. \tilde{E}_v, \tilde{H}_u can be interpreted as voltage and current (V^h, I^h) on a transverse electric (TE) transmission line. Also, we can find that

$(\tilde{J}_z, \tilde{M}_u, \tilde{M}_v)$ are associated with series voltage sources on a transmission line, and $(\tilde{M}_z, \tilde{J}_u, \tilde{J}_v)$ are associated with shunt current sources on a transmission line. Therefore, we use (V_v^p, I_v^p) to represent the voltage and current on the p -type transmission line due to the voltage source and use (V_i^p, I_i^p) to represent the voltage and current on the p -type transmission line due to the current source, $p = e$ or h .

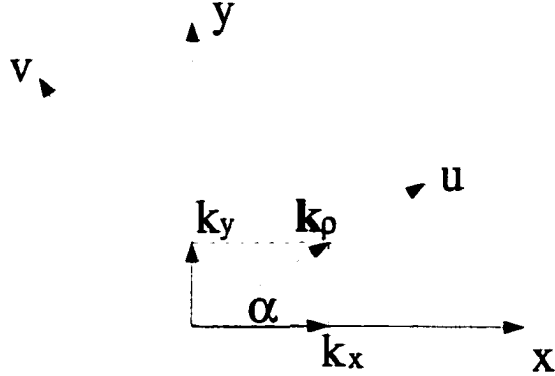


Figure 2.2 Coordinate rotation from (x, y) to (u, v) .

Now we can write the spectral domain dyadic Green's functions in the (u, v, z) coordinate system

$$\bar{\bar{G}}^{EJ}(\mathbf{k}_p, z|z') = \begin{bmatrix} -V_i^e & 0 & \frac{k_p}{\omega\epsilon_0\epsilon_r'} V_v^e \\ 0 & -V_i^h & 0 \\ \frac{k_p}{\omega\epsilon_0\epsilon_r'} I_i^e & 0 & \frac{1}{j\omega\epsilon_0\epsilon_r'} \left[\frac{k_p^2}{j\omega\epsilon_0\epsilon_r'} I_v^e - \delta(z - z') \right] \end{bmatrix} \quad (2.12)$$

$$\bar{\bar{G}}^{HJ}(\mathbf{k}_p, z|z') = \begin{bmatrix} 0 & I_i^h & 0 \\ -I_i^e & 0 & \frac{k_p}{\omega\epsilon_0\epsilon_r'} I_v^e \\ 0 & -\frac{k_p}{\omega\mu_0\mu_r} V_i^h & 0 \end{bmatrix} \quad (2.13)$$

$$\bar{\bar{G}}^{EM}(\mathbf{k}_p, z|z') = \begin{bmatrix} 0 & -V_v^e & 0 \\ V_v^h & 0 & -\frac{k_p}{\omega\mu_r} I_i^h \\ 0 & \frac{k_p}{\omega\epsilon_0\epsilon_r'} I_v^e & 0 \end{bmatrix} \quad (2.14)$$

$$\bar{\bar{G}}^{HM}(\mathbf{k}_p, z|z') = \begin{bmatrix} -I_v^h & 0 & \frac{k_p}{\omega\mu_0\mu_r'} I_i^h \\ 0 & -I_v^e & 0 \\ \frac{k_p}{\omega\mu_0\mu_r} V_v^h & 0 & \frac{1}{j\omega\mu_0\mu_r'} \left[\frac{k_p^2}{j\omega\mu_0\mu_r} V_i^h - \delta(z - z') \right] \end{bmatrix} \quad (2.15)$$

Using the relationship between (u, v) and (x, y) , we can obtain the spectral domain dyadic Green's functions in the (x, y, z) coordinate system through a transformation. These spectral domain Green's functions can be employed in the method of

Table 2.1 Two decoupled sets of transmission line equations in (u, v, z) coordinates

TM (e)	TE (h)
$\frac{d}{dz} \tilde{E}_u = -jk_z Z^e \tilde{H}_v + \frac{k_p}{\omega \epsilon_0 \epsilon_r} \tilde{J}_z - \tilde{M}_v$ $\frac{d}{dz} \tilde{H}_v = -jk_z Y^e \tilde{E}_u - \tilde{J}_u$ $\tilde{E}_z = -\frac{1}{j\omega \epsilon_0 \epsilon_r} (jk_p \tilde{H}_v + \tilde{J}_z)$	$\frac{d}{dz} \tilde{E}_v = -jk_z Z^h \tilde{H}_u + \tilde{M}_u$ $\frac{d}{dz} \tilde{H}_u = -jk_z Y^h \tilde{E}_v - \frac{k_p}{\omega \mu_0 \mu_r} - \tilde{J}_v$ $\tilde{H}_z = \frac{1}{j\omega \mu_0 \mu_r} (jk_p \tilde{E}_v - \tilde{M}_z)$
$Z^e = \frac{1}{Y^e} = \frac{k_z}{\omega \epsilon_0 \epsilon_r}, k_z = \sqrt{k_0^2 \epsilon_r \mu_r - k_p^2}$	$Z^h = \frac{1}{Y^h} = \frac{\omega \mu_0 \mu_r}{k_z}, k_z = \sqrt{k_0^2 \epsilon_r \mu_r - k_p^2}$

moments. There are two different ways to carry out this method. One is to write the integral equation in the spectral domain so that the spectral domain Green's functions can be used directly and the basis function has to be Fourier transformable. This approach can be traced back to the well-known spectral domain approach (SDA) [34], [35] and has been widely employed [13]–[32]. This approach is often applied to regularly shaped structures since the basis functions are usually chosen to be those which have analytical Fourier transforms, such as the roof-top and piecewise sinusoidal basis functions, although the Fourier transform of the triangular basis function is also available [33]. The double infinite integration is time consuming to evaluate even with some efficient algorithms [16], [17], [36]. However, when this approach is employed to deal with shielded structures [26]–[32] or periodic structures, the double integral is replaced by the double summation. The efficiency of this approach can be improved by using the fast Fourier transform (FFT) [28]–[32].

The other approach is to solve the integral equation in the spatial domain, and the spectral domain Green's functions have to be transformed to the spatial domain. In this approach, the mixed potential integral equation is more attractive than the electric field integral equation because of the lower singularity; we then derive the Green's functions for the potentials.

2.3 Spectral Domain Green's Functions for Potentials

As we know, the fields can be expressed in terms of vector and scalar potentials by the following equations:

$$\mathbf{E} = -j\omega \mathbf{A} - \nabla \Phi \quad (2.16)$$

$$\mathbf{H} = \frac{1}{\mu_0 \mu_r} \nabla \times \mathbf{A} \quad (2.17)$$

The Lorentz gauge is

$$\Phi = -\frac{1}{j\omega \epsilon_0 \epsilon_r \mu_0 \mu_r} \nabla \cdot \mathbf{A} \quad (2.18)$$

Using Green's functions, we have the following equations:

$$\mathbf{H} = \langle \bar{\mathbf{G}}^{HJ}; \mathbf{J} \rangle \quad (2.19)$$

$$\mathbf{A} = \mu_0 \langle \bar{\mathbf{G}}^A; \mathbf{J} \rangle \quad (2.20)$$

where the notation \langle , \rangle is used for integrals of products of two functions separated by a comma over their common spatial support, with a dot over the comma indicating vector dot product. Hence, the Green's function for vector potential is associated with the magnetic field by

$$\bar{\mathbf{G}}^{HJ} = \frac{1}{\mu_r} \nabla \times \bar{\mathbf{G}}^A \quad (2.21)$$

Note that $\bar{\mathbf{G}}^A$ is not uniquely defined in layered medium problems, as discussed in [70]. Here, the traditional form of $\bar{\mathbf{G}}^A$ is chosen:

$$\bar{\mathbf{G}}^A = \begin{bmatrix} G_{xx}^A & 0 & 0 \\ 0 & G_{yy}^A & 0 \\ G_{zx}^A & G_{zy}^A & G_{zz}^A \end{bmatrix} \quad (2.22)$$

In the spectral domain, the nabla operation is $\bar{\nabla} = -jk_x \hat{x} - jk_y \hat{y} + \hat{z} \frac{d}{dz}$. The $\bar{\mathbf{G}}^{HJ}$ can be derived from (2.13). Therefore, the components of $\bar{\mathbf{G}}^A$ can be written as

$$\bar{G}_{xx}^A = \frac{1}{j\omega \mu_0} V_i^h \quad (2.23)$$

$$\bar{G}_{yy}^A = \frac{\mu_r k_x}{jk_p^2} (I_i^h - I_i^e) \quad (2.24)$$

$$\bar{G}_{zy}^A = \frac{\mu_r k_y}{jk_p^2} (I_i^h - I_i^e) \quad (2.25)$$

$$\bar{G}_{zz}^A = \frac{\mu_r}{j\omega \epsilon_0 \epsilon_r} I_u^e \quad (2.26)$$

Once $\bar{\mathbf{G}}^A$ is available, the electric field can be obtained by using (2.16)

$$\mathbf{E} = -j\omega \mu_0 \left(\bar{\mathbf{I}} + \frac{1}{k^2} \nabla \nabla \cdot \right) \langle \bar{\mathbf{G}}^A; \mathbf{J} \rangle \quad (2.27)$$

which involves only the vector potential. Because of the difficulty associated with the nabla operator in the MoM implementation, the scalar potential is introduced to transfer the nabla operator to the current. For this reason, we have to find a scalar function G^Φ , which satisfies the following equation:

$$\frac{1}{\epsilon_r \mu_r} \nabla \cdot \bar{\mathbf{G}}^A = -\nabla' G^\Phi \quad (2.28)$$

As discussed in [69], the scalar potentials associated with the horizontal electric dipole (HED) and vertical electric dipole (VED) are different in layered media. We can use G_h^Φ and G_v^Φ to distinguish the scalar potentials due to HED and VED, respectively. By matching the three components of (2.28) in the spectral domain, we obtain the scalar potentials as

$$\tilde{G}_h^\Phi = \frac{j\omega\epsilon_0}{k_p^2} (V_i^e - V_i^h) \quad (2.29)$$

$$\tilde{G}_v^\Phi = \frac{1}{j\omega\epsilon_0\epsilon_r\epsilon'_r k_z'^2} \frac{d^2}{dz dz'} I_v^e = \frac{\omega\epsilon_0}{jk_z'^2} V_i^e \quad (2.30)$$

The different forms of HED and VED, however, bring more work when we deal with 3-D structures. The reason is that in the transformation of the nabla operator, a Guass theorem is applied:

$$\int_s \nabla' G^\Phi(\mathbf{r}, \mathbf{r}') \mathbf{J}(\mathbf{r}') d\mathbf{r}' = - \int_s G^\Phi(\mathbf{r}, \mathbf{r}') \nabla' \cdot \mathbf{J}(\mathbf{r}') d\mathbf{r}' + \int_l G^\Phi(\mathbf{r}, \mathbf{r}') \mathbf{J}(\mathbf{r}') \cdot \hat{n} dl \quad (2.31)$$

We observe that the undesirable line integral on the common edge of two patches will not disappear if different scalar potential Green's functions are employed. To overcome this problem, a correction vector function is introduced in addition to the scalar potential Green's function, as done in [70]. Different choices of this correction function give different features. The detailed discussion in [70] shows that it is preferable to choose the correction vector function as $C^\Phi \hat{z}$. With this, Equation (2.28) is modified as

$$\frac{1}{\epsilon_r \mu_r} \nabla \cdot \bar{\mathbf{G}}^A = -\nabla' G^\Phi + C^\Phi \hat{z} \quad (2.32)$$

From this relation, we can find \tilde{G}^Φ and \tilde{C}^Φ as

$$\tilde{G}^\Phi = \frac{j\omega\epsilon_0}{k_p^2} (V_i^e - V_i^h) \quad (2.33)$$

$$\tilde{C}^\Phi = \frac{k_0^2 \mu_r'}{k_p^2} (V_v^e - V_v^h) \quad (2.34)$$

The electric field can be expressed as

$$\mathbf{E} = -j\omega\mu_0 (\bar{\mathbf{G}}^A; \mathbf{J}) + \frac{1}{j\omega\epsilon_0} \nabla (\langle G^\Phi, \nabla' \cdot \mathbf{J} \rangle + \langle C^\Phi \hat{z}; \mathbf{J} \rangle) \quad (2.35)$$

Combining the first and third terms gives the following equation

$$\mathbf{E} = -j\omega\mu_0 \langle \bar{\mathbf{K}}^A; \mathbf{J} \rangle + \frac{1}{j\omega\epsilon_0} \nabla (\langle G^\Phi, \nabla' \cdot \mathbf{J} \rangle) \quad (2.36)$$

where the new vector potential Green's function $\bar{\mathbf{K}}^A$ can be expressed as

$$\bar{\mathbf{K}}^A = \begin{bmatrix} G_{xx}^A & 0 & G_{xz}^A \\ 0 & G_{xx}^A & G_{yz}^A \\ G_{zx}^A & G_{zy}^A & G_{zz}^A \end{bmatrix} \quad (2.37)$$

Here, G_{xx}^A , G_{xz}^A , and G_{zy}^A have the same forms as those in (2.22), respectively. The spectral domain counterparts of G_{xz}^A , G_{yz}^A , and G_{zz}^A can be written as

$$\tilde{G}_{xz}^A = \frac{\mu'_r k_x}{jk_\rho^2} (V_v^h - V_v^e) \quad (2.38)$$

$$\tilde{G}_{yz}^A = \frac{\mu'_r k_y}{jk_\rho^2} (V_v^h - V_v^e) \quad (2.39)$$

$$\tilde{G}_{zz}^A = \frac{1}{j\omega\epsilon_0} \left[\left(\frac{\mu_r}{\epsilon'_r} - \frac{\mu'_r k_z^2}{\epsilon_r k_\rho^2} \right) I_v^e + \frac{k_0^2 \mu_r \mu'_r}{k_\rho^2} I_v^h \right] \quad (2.40)$$

The G_{xz}^A and G_{yz}^A are related to G_{xx}^A and G_{zy}^A by

$$G_{xz}^A(\rho, z|z') = -\frac{\mu'_r}{\mu_r} G_{xx}^A(\rho, z'|z) \quad (2.41)$$

$$G_{yz}^A(\rho, z|z') = -\frac{\mu'_r}{\mu_r} G_{zy}^A(\rho, z'|z) \quad (2.42)$$

Therefore, the Green's functions required in this method are G_{xx}^A , G_{zz}^A , G_{xz}^A , G_{zy}^A , and G^Φ . Also, G_{xz}^A and G_{zy}^A have the same kernels so that a total of four Green's functions are required to be evaluated.

2.4 Discrete Complex Image Method

From the inverse Fourier-Bessel transform (2.5), we can write the spatial domain Green's function as

$$G(\rho, z|z') = \frac{1}{2\pi} \int_0^\infty \tilde{G}(\mathbf{k}_\rho, z|z') J_0(k_\rho \rho) k_\rho dk_\rho \quad (2.43)$$

That is the well-known Sommerfeld integral (SI). Therefore, G_{xx}^A , G_{zz}^A , and G^Φ can be directly written in the form of SI. The G_{xz}^A and G_{zy}^A can be obtained by transforming k_x and k_y in the spectral domain to their derivatives in the spatial domain, which gives

$$\begin{aligned} G_{zt}^A &= \frac{1}{2\pi} \frac{\partial}{\partial t} \int_0^\infty \frac{\mu_r}{k_\rho^2} (I_i^h - I_i^e) J_0(k_\rho \rho) k_\rho dk_\rho, \quad t = x, y \\ &= -\frac{1}{2\pi} \frac{\cos \phi}{\sin \phi} \int_0^\infty \frac{\mu_r}{k_\rho^2} (I_i^h - I_i^e) J_1(k_\rho \rho) k_\rho^2 dk_\rho \end{aligned} \quad (2.44)$$

Evaluation of Sommerfeld integrals is essential for the spatial domain approach, which is very time consuming because of the highly oscillating and slowly decaying behavior of the integrand. Although some techniques have been proposed for fast evaluation of the SI, the numerical integration is still the bottleneck for a fast algorithm. The DCIM obviates the numerical integration and represents the SI in a closed form. In the original work of the DCIM, the quasi-static and surface-wave contributions are first extracted from the spectral domain kernel, so the remaining kernel is approximated by a sum of complex exponentials, and finally the closed-form is obtained via the Sommerfeld identity. This method has been extensively employed to analyze microstrip structures. However, most of the work is confined to single-layered or double-layered structures since the surface-wave contribution is extracted analytically using residue calculus, which makes the DCIM difficult to extend to multilayer media. Therefore, to use the DCIM for multilayer media, the surface waves are often not extracted [62]. This approximation is only valid for the thin multilayer configurations, where the surface-wave contribution is insignificant. However, for a general multilayer media with strong surface-wave contribution, the lack of the surface-wave extraction results in significant errors in the far field since the surface waves behave in the manner of cylindrical waves and it is physically inappropriate to approximate such waves by spherical waves. For a general-purpose algorithm, especially for the MoM analysis of electrically large structures, the surface waves have to be extracted. In this work, the surface-wave extraction is carried out numerically by evaluating a multilevel contour integral in the k_ρ -plane in the following steps. First, evaluate the contour integral along an enclosed box in the k_ρ -plane and check the value. If it is nonzero, subdivide the region into four subregions. Evaluate the contour integral for each subregion. The process is repeated until the precise pole locations and residues are determined.

Let us rewrite the spectral domain Green's function in a simple form as

$$\tilde{G} = A \frac{F}{2jk_{zm}} \quad (2.45)$$

where A is a constant, which has the value of μ_{rm} , μ_{rn} , μ_{rn} , $1/\epsilon_{rm}$ for G_{xx}^A , G_{zt}^A , G_{zz}^A , and G_h^Φ , respectively. As the first step of the DCIM, the primary field term F_{pr} can be extracted from F when the source and observation points are in the same layer. Notice that there is no primary field term in \tilde{G}_{zs}^A . The static contributions F_{st} , which dominate as $k_\rho \rightarrow \infty$, are also extracted, which makes the remaining kernel decay to zero for sufficiently large k_ρ . For the TE case they approach $(\mu_i - \mu_{i+1})/(\mu_i + \mu_{i+1})$,

while in the TM case they tend to $(\epsilon_i - \epsilon_{i+1})/(\epsilon_i + \epsilon_{i+1})$. It happens only when both source and field points are on the interface of two different layers.

The second step is to extract the surface-wave contributions F_{sw} , which can make the kernel smooth. The F_{sw} can be written as

$$F_{sw} = 2jk_{zm} \sum_i \frac{2k_{pi} Res_i}{k_p^2 - k_{pi}^2} \quad (2.46)$$

where Res_i is the residue for the pole k_{pi} . In the previous work of the DCIM, Res_i is treated analytically by using residue calculus, which makes it difficult to extend to multilayer cases. Here, we can obtain Res_i by recursively evaluating the contour integral numerically in the complex k_p -plane. As described earlier, the integral begins with the contour enclosing the region we are interested in. If it is nonzero, then subdivide into four pieces and evaluate the contour integral of each piece. Repeat this process until the location k_{pi} and residues Res_i for all the poles are found. These procedures can be illustrated by the following two examples. One is a five-layer medium with the top layer being free space, as shown in Fig. 2.3, which plots the magnitude of \bar{G}^Φ in the first and fourth quadrants. The contour integral is repeated until we find the surface-wave poles at $k_p = 1.736k_0, 2.435k_0$. Since the top layer is the unbounded free space, there is a branch cut associated with k_{z0} , where the radiation modes lie on [68]. The branch cut is deliberately avoided. The other case is a shielded three-layer medium shown in Fig. 2.4, which plots the magnitude of \bar{G}^Φ in the first and fourth quadrants. The contour integral is repeated until we find the poles at $k_p = 0.671k_0, 0.719k_0, 1.055k_0$. The pole $k_p = 1.055k_0$ corresponds to the surface waves. The poles at $[0, k_0]$ are associated with the modes guided by two ground planes. The poles at the imaginary axis corresponds to the evanescent modes, which are not extracted in this method.

After these steps, the spectral domain Green's function can be written as

$$\bar{G} = A \frac{F - F_{pr} - F_{st} - F_{sw}}{2jk_{zm}} \quad (2.47)$$

The final step is to approximate the remainder of F as a sum of complex exponentials using the GPOF method. The deformed integration path in the complex k_{zm} is chosen as $k_{zm} = k_m [(1 - t/T_0) - jt]$, where T_0 is determined such that the remainder of F becomes negligible beyond T_0 . Uniformly sampling on $t \in [0, T_0]$ and applying the GPOF method, we can obtain

$$F - F_{pr} - F_{st} - F_{sw} = \sum_{i=1}^{N_c} a_i e^{-jk_{zm} b_i} \quad (2.48)$$

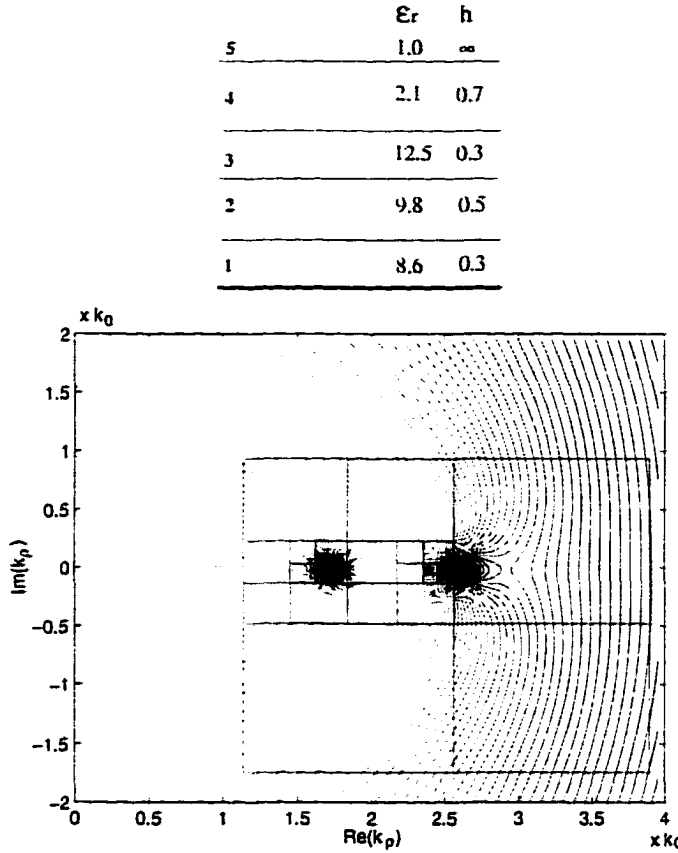


Figure 2.3 Magnitude of \tilde{G}^Φ in the first and fourth quadrants of the complex k_ρ -plane for a five-layer medium. The frequency is 30 GHz. Unit for thickness is mm.

With the aid of the Sommerfeld identity

$$\frac{e^{-jk_m r}}{4\pi r} = \frac{1}{2\pi} \int_0^\infty \frac{e^{-jk_{zm}|z|}}{2jk_{zm}} J_0(k_\rho \rho) k_\rho dk_\rho \quad (2.49)$$

we obtain

$$G = \frac{A}{4\pi} \left(\frac{e^{-jk_m r}}{r} + F_{st} \frac{e^{-jk_m \rho}}{\rho} - 2\pi j \sum_i \text{Res}_i H_0^{(2)}(k_{pi} \rho) k_{pi} + \sum_{i=1}^{N_c} a_i \frac{e^{-jk_m r_i}}{r_i} \right) \quad (2.50)$$

where $r_i = \sqrt{\rho^2 + b_i^2}$.

As pointed out in [60], for the multilayer medium with the top or bottom layer unbounded, there is a branch cut. For instance, when the top layer is free space, the branch cut is associated with k_{z0} . When the source is in the bounded region of multilayer media, the DCIM needs to be modified. In that case, we rewrite (2.45) as

$$\tilde{G} = A \frac{F'}{2jk_{z0}} \quad F' = F \frac{k_{z0}}{k_{zm}} \quad (2.51)$$

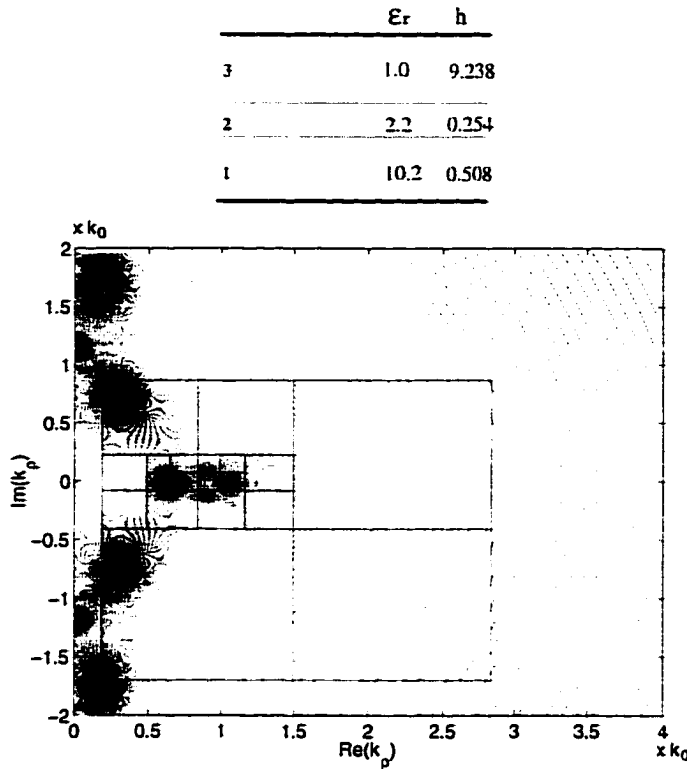
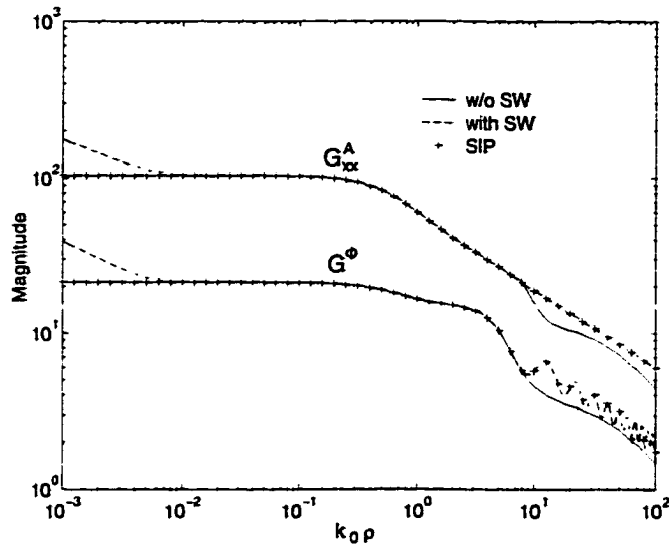


Figure 2.4 Magnitude of \tilde{G}^Φ in the first and fourth quadrants of the complex k_ρ -plane for a shield three-layer medium. The frequency is 20 GHz. Unit for thickness is mm.

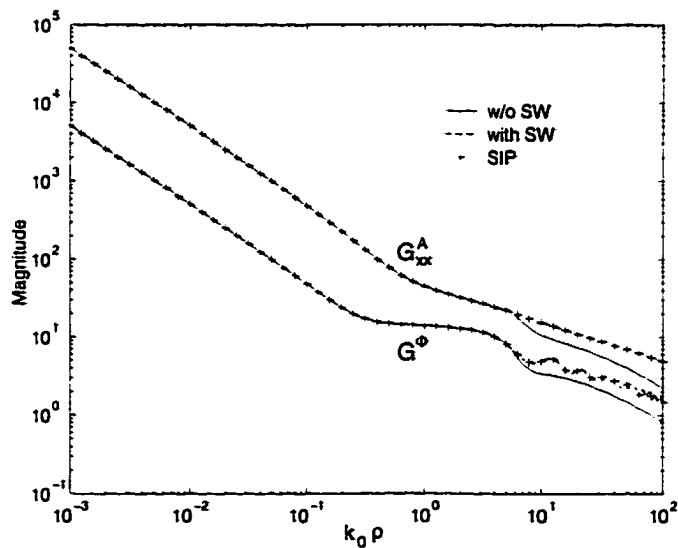
As a consequence, k_{zm} in F_{pr} and F_{sw} is replaced by k_{z0} . The GPOF approximation in (2.48) is performed in terms of k_{z0} . For a shielded multilayer medium, since there are no branch-cuts, such a modification is not required.

With the surface-wave extraction, the DCIM works well in the far field. However, a problem is encountered for the near field evaluation. As we know, when $z \neq z'$, the Green's function is not singular at $\rho = 0$; however, the surface-wave term carries the singularity. When $z = z'$, since the singularity in the surface-wave term is weaker than that in the primary field term, the DCIM with surface-wave extraction still works in the near field region. This phenomenon is shown in Fig. 2.5, where a five-layer medium problem is investigated for $z = z'$ and $z \neq z'$, respectively. In the figure, the dashed and solid lines represent those obtained by the DCIM with and without the surface-wave extraction, respectively. The crosses represent those obtained by direct numerical integration along the Sommerfeld integration path (SIP).

To overcome this difficulty, a transition point is introduced, as is done in [57] and



(a)



(b)

Figure 2.5 Magnitude of Green's functions G_{xx}^A and G^ϕ for a five-layer medium. The frequency is 30 GHz. Unit for thickness is mm. (a) $z' = 0.4, z = 1.4$. (b) $z' = 0.4, z = 0.4$.

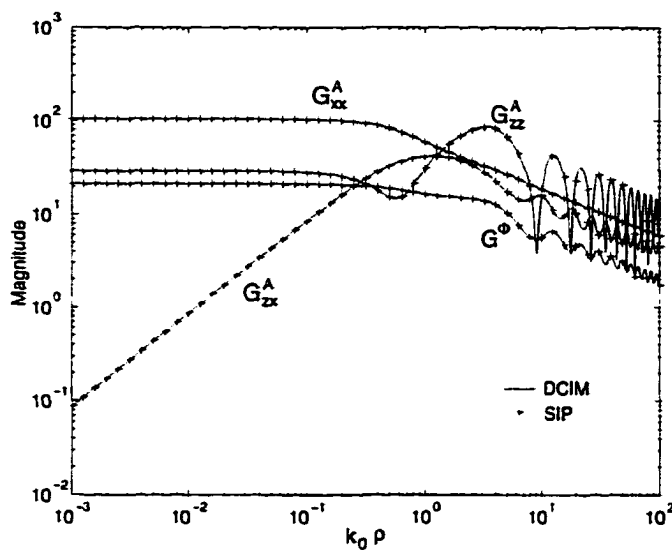
[63]. The near field and far field are divided by the transition point. Therefore, the DCIM is applied twice, one with and the other without the surface-wave extraction. For the near field region, the Green's function can be evaluated by the first approach. For the far field region, the Green's function can be evaluated by the second approach. From Fig. 2.5, we can see that the two approaches overlap in the middle region and the transition point can be easily picked up, say, $\log_{10} k_0 \rho = 0$. With this modification, the DCIM works for all the regions. The magnitudes of four Green's functions G_{xx}^A , G_{yy}^A , G_{zz}^A , and G_ϕ are shown in Fig. 2.6 for $z = z'$ and $z \neq z'$, respectively. Note that G_{xx}^A approaches zero as $\rho \rightarrow 0$ except in the case that both source and field points are at the different interfaces.

The shielded three-layer medium is investigated [54]. The frequency is at $f = 20$ GHz. Both the source and observation points are at the interface between the second and third layers. Again, the magnitudes of all the four Green's functions are plotted in Fig. 2.7, compared with the numerical integration results. Again, a good agreement can be observed.

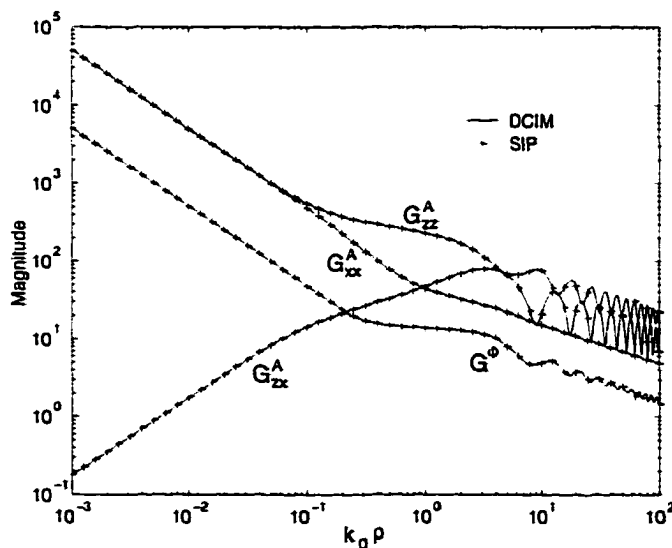
2.5 Green's Function Interpolations

The DCIM provides an efficient way to evaluate the Green's functions; however, issues about computer time have to be considered since the number of Green's functions to be evaluated is proportional to $O(N^2)$ in the MoM analysis. One is to evaluate the Hankel function, which is expensive compared to the evaluation of the remaining part. For the structures supporting vertical currents, the Green's functions for all the different combinations of z and z' are needed. The DCIM has to be performed at every combination, although it is possible for some cases to generate the complex images that are independent of z and z' . To circumvent these problems, the interpolation scheme is usually employed [44], [45], [50], [64], [53]. First, determine the sections in the z axis where the structure is located, and subdivide it into N sheets. There are a total of N^2 combinations of z and z' . For each pair of sheets, the DCIM is performed and the Chebyshev interpolation is applied to the variable ρ [80]. For G_{xx}^A , G_{zz}^A , and G^Φ , the reciprocity can reduce the number of times to perform the DCIM to $N(N + 1)/2$. For G_{yy}^A , the reciprocity does not hold. When z and z' are located between those sheets, the Lagrange polynomial interpolation is employed for the variables z and z' .

With the interpolation strategy, the computer time to evaluate the Green's func-

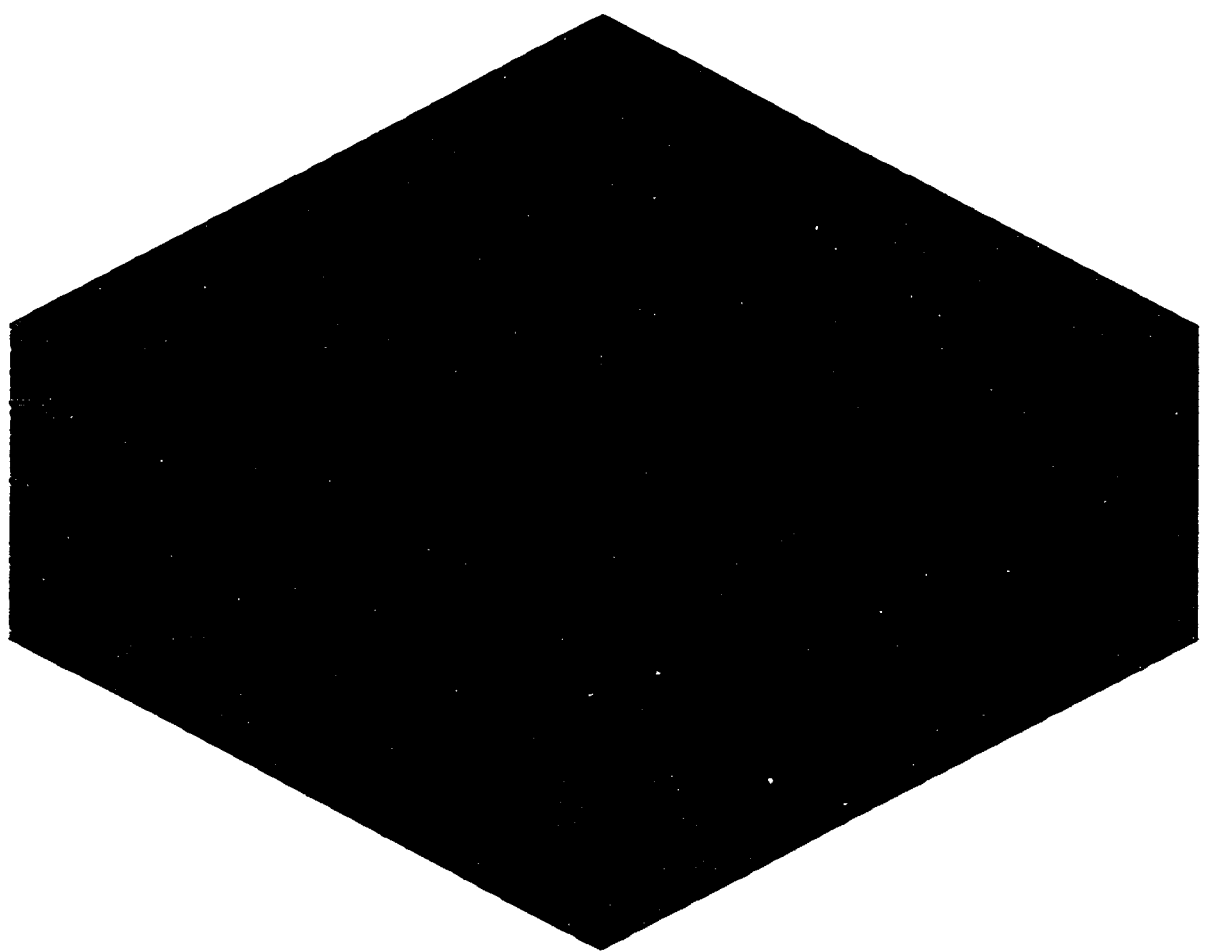


(a)



(b)

Figure 2.6 Magnitude of Green's functions, G_{xx}^A , G_{zx}^A , G_{zz}^A , and G^Φ for a five-layer medium. The frequency is 30 GHz. Unit for thickness is mm. (a) $z' = 0.4, z = 1.4$. (b) $z' = 0.4, z = 0.4$.



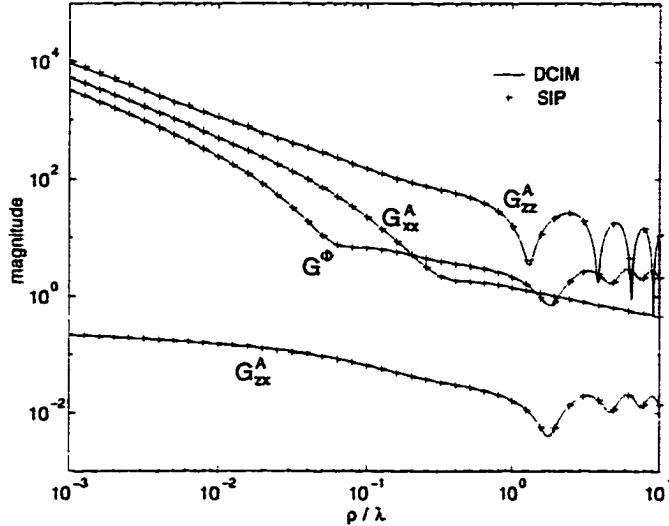


Figure 2.7 Magnitude of Green's functions, G_{xx}^A , G_{zz}^A , G_ϕ^A , and G_{zx}^A for a shielded three-layer medium. The frequency is 20 GHz. $z = z' = 0.762$. Unit for thickness is mm.

tions for multilayer media is further reduced in the MoM analysis. Also, it is possible to store the interpolation coefficients as a database instead of performing the interpolations on-line. Therefore, the generation of Green's functions is decoupled from circuit geometries.

2.6 Transmission Line Green's Functions

Now we derive the solution of the transmission line equation. Let $V_v^p(z|z')$ and $I_v^p(z|z')$ be the voltage and current at z , respectively, due to a 1-A shunt current source at z' , and $V_i^p(z|z')$ and $I_i^p(z|z')$ be the voltage and current at z , respectively, due to a 1-V series current source at z' . They satisfy the following equations:

$$\frac{d}{dz} V_i^p = -jk_z Z^p I_i^p \quad (2.52)$$

$$\frac{d}{dz} I_i^p = -jk_z Y^p V_i^p + \delta(z - z') \quad (2.53)$$

$$\frac{d}{dz} V_v^p = -jk_z Z^p I_v^p + \delta(z - z') \quad (2.54)$$

$$\frac{d}{dz} I_v^p = -jk_z Y^p V_v^p \quad (2.55)$$

First we represent each layer as a transmission line section, which is characterized

by the propagation constant k_z and the characteristic impedance (admittance) Z (Y). Consider the unit-strength source at z' in section m and compute the voltage and current at z in section n . The general forms are given for different combinations of the source and observation sections.

When the source and observation points are in the same section ($m = n$), V_i^p is given by

$$V_i^p(z|z') = \frac{Z_m^p}{2} \left[e^{-jk_{zm}|z-z'|} + M_m^p \sum_{s=1}^4 B_{ms}^p e^{-jk_{zm}\gamma_{ms}} \right] \quad (2.56)$$

where

$$\begin{aligned} B_{m1}^p &= \bar{R}_{m,m+1}^p, \quad \gamma_{m1} = 2z_m - (z + z') \\ B_{m2}^p &= \bar{R}_{m,m-1}^p, \quad \gamma_{m2} = -2z_{m-1} + (z + z') \\ B_{m3}^p &= \bar{R}_{m,m-1}^p \bar{R}_{m,m+1}^p, \quad \gamma_{m3} = 2(z_m - z_{m-1}) - (z - z') \\ B_{m4}^p &= B_{m3}^p, \quad \gamma_{m4} = 2(z_m - z_{m-1}) + (z - z') \\ M_m^p &= \left[1 - \bar{R}_{m,m-1}^p \bar{R}_{m,m+1}^p e^{-2jk_{zm}(z_m - z_{m-1})} \right]^{-1} \end{aligned}$$

From (2.52), we can derive I_i^p as

$$I_i^p(z|z') = \frac{1}{2} \left[\pm e^{-jk_{zm}|z-z'|} + M_m^p \sum_{s=1}^4 (-1)^s B_{ms}^p e^{-jk_{zm}\gamma_{ms}} \right] \quad (2.57)$$

The generalized reflection coefficient $\bar{R}_{m,m+1}^p$ is given by

$$\bar{R}_{m,m+1}^p = \frac{R_{m,m+1}^p + \bar{R}_{m+1,m+2}^p e^{-j2k_{zm+1}(z_{m+1} - z_m)}}{1 + R_{m,m+1}^p \bar{R}_{m+1,m+2}^p e^{-j2k_{zm+1}(z_{m+1} - z_m)}} \quad (2.58)$$

where \bar{R}^p can be recursively obtained and R^p is given by

$$R_{m,m+1}^p = \frac{Z_{m+1}^p - Z_m^p}{Z_{m+1}^p + Z_m^p} \quad (2.59)$$

When the source section is below the observation section ($m < n$), the voltage and current at z in section n can be derived recursively from those in section m . The final solution of V_i and I_i is

$$\begin{aligned} V_i^p(z|z') &= \frac{Z_m^p}{2} T_{mn}^{p,+} \left[e^{jk_{zm}(-z_m + z')} + \bar{R}_{m,m-1}^p e^{-jk_{zm}(-2z_{m-1} + z_m + z')} \right] \\ &\quad \cdot \left[e^{-jk_{zn}(-z_{n-1} + z)} + \bar{R}_{n,n+1}^p e^{-jk_{zn}(-z_{n-1} + 2z_n - z)} \right] \bar{M}_m^p \end{aligned} \quad (2.60)$$

and

$$\begin{aligned} I_i^p(z|z') &= \frac{Z_m^p}{2} T_{mn}^{p,+} Y_n^p \left[e^{jk_{zm}(-z_m + z')} + \bar{R}_{m,m-1}^p e^{-jk_{zm}(-2z_{m-1} + z_m + z')} \right] \\ &\quad \cdot \left[e^{-jk_{zn}(-z_{n-1} + z)} - \bar{R}_{n,n+1}^p e^{-jk_{zn}(-z_{n-1} + 2z_n - z)} \right] \bar{M}_m^p \end{aligned} \quad (2.61)$$

Here, $T_{mn}^{p,+}$ is the generalized transmission coefficient from section m to section n , which can be written in a general form

$$T_{mn}^{p,+} = \prod_{i=m}^{n-1} e^{-jk_{zi}(z_i - z_{i-1})} S_{i,i+1}^{p,+} \quad (2.62)$$

where $z_{m-1} = z_m$ is assumed and $S_{i,i+1}^{p,+}$ is given by

$$S_{i,i+1}^{p,+} = \frac{1 + R_{i,i+1}^p}{1 - R_{i+1,i}^p \tilde{R}_{i+1,i+2}^p e^{-2jk_{zi+1}(z_{i+1} - z_i)}} \quad (2.63)$$

When the source section is above the observation section ($m > n$), the voltage and current at z in section n can be derived recursively from those in section m . The final solution of V_i and I_i is

$$\begin{aligned} V_i^p(z|z') = & \frac{Z_m^p}{2} T_{mn}^{p,-} \left[e^{-jk_{zm}(-z_{m-1} + z')} + \tilde{R}_{m,m+1}^p e^{-jk_{zm}(2z_m - z_{m-1} - z')} \right] \\ & \cdot \left[e^{-jk_{zn}(z_n - z)} + \tilde{R}_{n,n-1}^p e^{-jk_{zn}(-2z_{n-1} + z_n + z)} \right] \tilde{M}_m^p \end{aligned} \quad (2.64)$$

and

$$\begin{aligned} I_i^p(z|z') = & \frac{Z_m^p}{2} T_{mn}^{p,-} Y_n^p \left[e^{-jk_{zm}(-z_{m-1} + z')} + \tilde{R}_{m,m+1}^{TM} e^{-jk_{zm}(2z_m - z_{m-1} - z')} \right] \\ & \cdot \left[-e^{-jk_{zn}(z_n - z)} + \tilde{R}_{n,n-1}^p e^{-jk_{zn}(-2z_{n-1} + z_n + z)} \right] \tilde{M}_m^p \end{aligned} \quad (2.65)$$

Here, $T_{mn}^{p,-}$ is written as

$$T_{mn}^{p,-} = \prod_{i=n+1}^m e^{-jk_{zi}(z_i - z_{i-1})} S_{i,i-1}^{p,-} \quad (2.66)$$

where $z_m = z_{m-1}$ is assumed and $S_{i,i-1}^{p,-}$ is given by

$$S_{i,i-1}^{p,-} = \frac{1 + R_{i,i-1}^p}{1 - R_{i-1,i}^p \tilde{R}_{i-1,i-2}^p e^{-2jk_{zi-1}(z_{i-1} - z_{i-2})}} \quad (2.67)$$

Knowing V_i^p and I_i^p , we can derive I_v^p and V_v^p by duality. Therefore, I_v^p and V_v^p are obtained by making the following substitutions:

$$V_i^p \rightarrow I_v^p, I_i^p \rightarrow V_v^p, Z_n^p \rightarrow Y_n^p, Y_n^p \rightarrow Z_n^p \quad (2.68)$$

From the above, we can further show that

$$\frac{1}{Z_m^p} V_i^p(z|z') = \frac{1}{Z_n^p} V_i^p(z'|z) \quad (2.69)$$

$$I_i^p(z|z') = -V_v^p(z'|z) \quad (2.70)$$

With this relationship, two cases $m > n$ and $m < n$ do not have to be written in different expressions, which makes programming easy.

2.7 Conclusion

This chapter presents an efficient approach to evaluate the spatial domain Green's functions for multilayer media. The spectral domain Green's functions for multilayer media are first derived by the transmission line analogy, and the spatial domain Green's functions in the form of SIs are then evaluated by the DCIM, which obviates the time-consuming numerical integration. In the DCIM, a novel approach to determine the surface-wave poles and their residues is proposed. An interpolation scheme is employed to further reduce the time to evaluate Green's functions in the MoM analysis.

CHAPTER 3

MOM SOLUTION FOR MULTILAYER MICROSTRIP STRUCTURES

3.1 Introduction

With the integral equation and the Green's functions available, the method of moments (MoM) is employed to solve the integral equation. A critical factor for an efficient and accurate MoM analysis is the choice of basis functions. Traditional numerical modeling employs roof-top functions for rectangular discretization or Rao-Wilton-Glisson (RWG) functions [73] for triangular discretization. These functions are complete to the zeroth order. As a result, a very fine discretization is often required to yield an accurate solution. This leads to a large matrix equation, which is expensive to solve. In addition, the numerical solution converges slowly to the exact one when the discretization is made finer. A solution to this problem is to employ higher-order basis functions, which have a better convergence rate and can yield an accurate solution with a rather coarse discretization. The better convergence of higher-order basis functions has been demonstrated in the literature [74]–[76]. The higher-order interpolatory basis functions developed by Graglia et al. [75] are employed in this work. Also, the curvilinear discretization is used, which provides more flexibility to model arbitrary shapes.

This chapter begins with the MPIE formulation for a 3-D microstrip structure in multilayer media and the MoM solution to this equation. The construction of the higher-order interpolatory basis functions is given. The right-hand side in the MoM formulation is discussed for different problems, and the parameter extraction is also presented. Finally, some representative examples are analyzed to demonstrate the accuracy and efficiency of this algorithm.

3.2 MPIE Formulation

The mixed-potential form of the electric field is given by (2.36). With excitation by an applied field \mathbf{E}^a , the induced current on the microstrips can be found by solving

the following MPIE

$$\hat{n} \times \left[-j\omega\mu_0 \langle \bar{K}^A(\mathbf{r}, \mathbf{r}'); \mathbf{J}(\mathbf{r}') \rangle + \frac{1}{j\omega\epsilon_0} \nabla \langle G^\Phi(\mathbf{r}, \mathbf{r}'), \nabla' \cdot \mathbf{J}(\mathbf{r}') \rangle \right] = -\hat{n} \times \mathbf{E}^a(\mathbf{r}) \quad (3.1)$$

To solve the integral equation (3.1) by the MoM, the surface is first divided into curvilinear triangular patches, which offer more flexibility to model the arbitrary shapes than flat triangular patches. As shown in Fig. 3.1(a), the quadratic triangular patch is employed, which is described by six nodes. After the coordinate transformation, shown in Fig. 3.1(b), we can easily describe any vector \mathbf{r} on the patch in terms of the quadratic shape function φ

$$\mathbf{r} = \sum_{i=1}^6 \varphi_i(\xi_1, \xi_2, \xi_3) \mathbf{r}_i \quad (3.2)$$

where the coordinates ξ_1, ξ_2, ξ_3 have the dependence relation as $\xi_1 + \xi_2 + \xi_3 = 1$ and the shape functions are given by

$$\begin{aligned} \varphi_1 &= \xi_1(2\xi_1 - 1) & \varphi_2 &= \xi_2(2\xi_2 - 1) & \varphi_3 &= \xi_3(2\xi_3 - 1) \\ \varphi_4 &= 4\xi_1\xi_2 & \varphi_5 &= 4\xi_2\xi_3 & \varphi_6 &= 4\xi_3\xi_1 \end{aligned} \quad (3.3)$$

The edge vectors can be calculated as

$$\ell_1 = -\frac{\partial \mathbf{r}}{\partial \xi_2}, \quad \ell_2 = -\frac{\partial \mathbf{r}}{\partial \xi_1}, \quad \ell_3 = \frac{\partial \mathbf{r}}{\partial \xi_2} - \frac{\partial \mathbf{r}}{\partial \xi_1} \quad (3.4)$$

The gradient vectors are evaluated by

$$\nabla \xi_1 = \frac{\hat{n} \times \ell_1}{J}, \quad \nabla \xi_2 = \frac{\hat{n} \times \ell_2}{J}, \quad \nabla \xi_3 = -\nabla \xi_1 - \nabla \xi_2 \quad (3.5)$$

where J is the *Jacobian*.

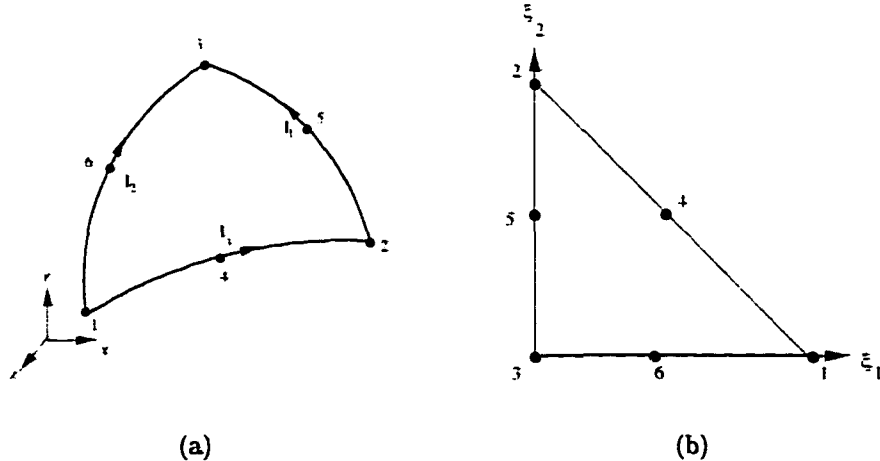


Figure 3.1 A curvilinear patch in (x, y, z) and (ξ_1, ξ_2, ξ_3) coordinates.

The building block of the higher-order interpolatory basis functions is the zeroth-order basis function, which is given by

$$\Lambda_\beta(\mathbf{r}) = \frac{1}{J} (\xi_{\beta+1} \ell_{\beta-1} - \xi_{\beta-1} \ell_{\beta+1}), \quad \beta = 1, 2, 3 \quad (3.6)$$

The zeroth-order basis function on the flat triangular patch is also known as the RWG basis function [73]. Figure 3.2 shows that the zeroth-order basis function has constant normal and linear tangential variation along edges and linear variation over faces.

The higher-order interpolatory vector basis functions on a given triangular element are constructed by multiplying the zeroth-order basis functions with a set of polynomial functions [75]

$$\Lambda_{ijk}^\beta(\mathbf{r}) = N_\beta \frac{(p+2)\xi_\beta \hat{\alpha}_{ijk}(\xi)}{i_\beta} \Lambda_\beta(\mathbf{r}) \quad (3.7)$$

where β denotes the edge number associated with the zeroth-order basis function; i, j , and k are the indexes for labeling the interpolation points, which satisfy $i + j + k = p + 2$; and i_β takes i, j , or k for $\beta = 1, 2$, or 3, respectively. The normalization coefficients N_{ijk}^β are given by

$$N_\beta = \frac{p+2}{p+2-i_\beta} \ell_\beta \quad (3.8)$$

The $\hat{\alpha}_{ijk}(\xi)$ is the polynomial function defined in terms of shifted Silvester-Lagrange polynomials \hat{R} as

$$\hat{\alpha}_{ijk}(\xi) = \hat{R}_i(p+2, \xi_1) \hat{R}_j(p+2, \xi_2) \hat{R}_k(p+2, \xi_3) \quad (3.9)$$

where the shifted Silvester-Lagrange polynomial is given by

$$\hat{R}_i(p, \xi) = \begin{cases} \frac{1}{(i-1)!} \prod_{k=1}^{i-1} (p\xi - k), & 2 \leq i \leq p+1 \\ 1, & i = 1. \end{cases} \quad (3.10)$$

The number of degrees of freedom is $N_e = (p+1)(p+3)$ on a triangular element for the basis functions of order p . The first-order basis functions so obtained are shown in Fig. 3.3, which shows linear normal and quadratic tangential variation at edges and quadratic variation over faces.

Therefore, the current density on each patch is expanded as

$$\mathbf{J}(\mathbf{r}) = \sum_{i=1}^{N_e} I_i \Lambda_i(\mathbf{r}) \quad (3.11)$$

Substituting (3.11) into (3.1) and applying Galerkin's procedures, we obtain a matrix equation

$$\bar{\mathbf{Z}} \cdot \mathbf{I} = \mathbf{V} \quad (3.12)$$

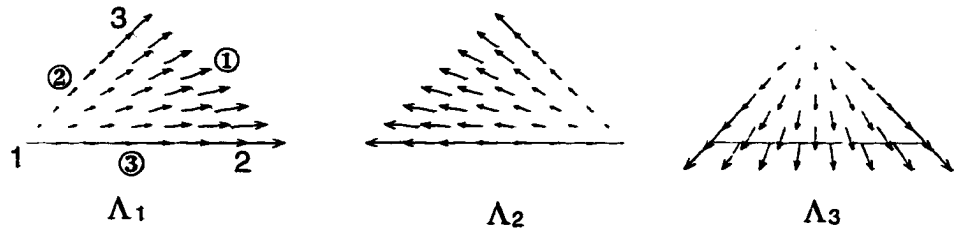


Figure 3.2 The zeroth-order basis function.

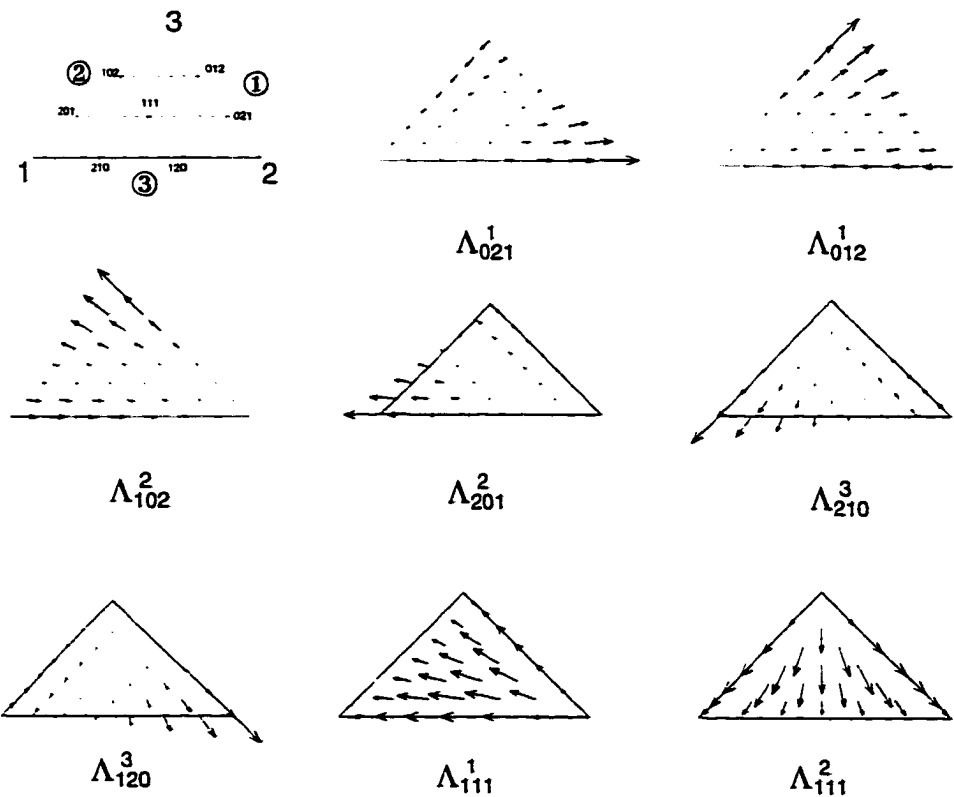


Figure 3.3 The first-order basis function.

where the global impedance matrix $\bar{\mathbf{Z}}$ and the right-hand side (RHS) vector are assembled from the local impedance matrix and local RHS vector, respectively. For example, the local impedance matrix for patch m and patch n has the dimension $N_e \times N_e$, and the local RHS vector has the dimension N_e , whose elements Z_{ij} and V_i

are given by

$$Z_{ij}^{mn} = -j\omega\mu_0 \langle \Lambda_i; \langle \bar{\mathbf{K}}^A; \Lambda_j \rangle_{S_n} \rangle_{S_m} - \frac{1}{j\omega\epsilon_0} \langle \nabla \cdot \Lambda_i, \langle G^\Phi, \nabla' \cdot \Lambda \rangle_{S_n} \rangle_{S_m} \quad (3.13)$$

$$V_i^m = -\langle \Lambda_i, \mathbf{E}^a \rangle_{S_m} \quad (3.14)$$

The double surface integrals are involved in the matrix element, which are evaluated by using Gaussian quadrature when the two elements do not overlap. When they do, the method proposed by Duffy [77] is employed to evaluate the singular integral.

3.3 Excitation and Parameter Extraction

The excitation, or equivalently the right-hand side of (3.1), is different for different problems. When the scattering properties of microstrip antennas are of interest, the applied field \mathbf{E}^a should be the electric field in the multilayer media environment without conductors. When we are simulating circuit problems, a voltage delta source is usually applied to the excitation port.

First consider scattering problems. For a microstrip structure embedded in multilayer media, the applied field \mathbf{E}^a is the electric field in the absence of the conductors, which can be easily obtained if we understand the derivation in Chapter 2. For radiation/circuit problems, we can use a voltage delta source at the excitation port. As a result, only a few patches have a contribution to V in (3.12).

Once the current distribution on the microstrips are obtained. The parameters associated with the current distribution are then extracted. For the scattering/radiation problems, those parameters are far fields, which can be calculated by the standard stationary phase method. A simpler approach is to employ the reciprocity theorem [51]. In accordance with the reciprocity theorem, the field (\mathbf{E}^{sc}) radiated by \mathbf{J} in the presence of multilayer media is related to \mathbf{J} by

$$\iiint_V \mathbf{E}^{sc} \cdot \mathbf{J}_2 d\mathbf{r} = \iint_S \mathbf{E}_2 \cdot \mathbf{J} d\mathbf{r} \quad (3.15)$$

where \mathbf{J}_2 denotes an arbitrary electric current and \mathbf{E}_2 is the field radiated by \mathbf{J}_2 in the presence of multilayer media. Choosing an infinitesimal electric current element, either θ -polarized or ϕ -polarized, and placing it at the observation point in the far zone, we can compute the electric field ($\mathbf{E}_{\theta,\phi}$) in the presence of multilayer media without the microstrip antenna, where \mathbf{E}_θ is due to the θ -polarized electric current element and \mathbf{E}_ϕ due to the ϕ -polarized electric current element. In the backscatter case, they are the same as \mathbf{E}^a in (3.1). Hence, from the reciprocity theorem, we can

obtain the scattered field as

$$E_{\theta,\phi}^{sc}(\mathbf{r}) = -\frac{j\omega\mu_0 e^{-jk_0 r}}{4\pi r} \iint_S \mathbf{J}(\mathbf{r}') \cdot \mathbf{E}_{\theta,\phi}(\mathbf{r}') d\mathbf{r}' \quad (3.16)$$

If the incident field is polarized in the u direction and the v component of the scattered field is considered, where u and v can be θ or ϕ , then the radar cross section (RCS) is given by

$$\sigma_{uv} = \lim_{r \rightarrow \infty} 4\pi r^2 \frac{|E_v^{sc}|^2}{|E_u^i|^2} \quad (3.17)$$

For the circuit problems, the S-parameters are usually extracted. For N -port circuit problems, it is necessary to extract the scattering parameters. In general, N linearly independent excitations are required for N -port network. The current distribution along the microstrip line associated with the i th port can be expressed as

$$I_i(x) = \frac{1}{\sqrt{Z_{0i}}} (a_i e^{-j\beta_i x} - b_i e^{j\beta_i x}) \quad (3.18)$$

Here, port i is assumed to be in the x -direction, and Z_{0i} and β_i are the characteristic impedance and the propagation constant of the microstrip line at port i , respectively, which can be determined in advance. The coefficients a_i and b_i can be extracted by the three-point curve-fitting scheme proposed in [44]. The least-square fit of more current samples can result in a more accurate solution. To obtain correct results, one has to make sure that the sampling points are away from the discontinuity and the excitation plane, which also indicates that the microstrip line should be long enough to have the standing wave pattern. Once all a_i 's and b_i 's are obtained, one can obtain the following equations associated with the S-parameters:

$$\sum_{i=1}^N a_i S_{ji} = b_j \quad (j = 1, 2, \dots, N). \quad (3.19)$$

Repeating this process N times for N different excitation schemes, one can obtain N^2 equations for all the S-parameters. In some practical cases, the properties of symmetry and reciprocity can be utilized to reduce the number of excitations. Another de-embedding algorithm is proposed in [78], which is widely used for parameter extraction.

3.4 Numerical Results

3.4.1 Convergence behavior of higher-order methods

The convergence behavior of the higher-order MoM is first analyzed using a microstrip patch antenna as an example. The patch is 40 mm by 40 mm, which resides

on a substrate with relative permittivity 2.17 and thickness 1.58 mm. The incident plane wave is assumed to be $\hat{\theta}$ polarized with the incident angle $(\theta^i, \phi^i) = (60^\circ, 45^\circ)$. The frequency is 10 GHz. The $\hat{\theta}$ component of backscattered RCS is calculated. The simulation is carried out at various levels of discretization for basis functions with different orders. The error is plotted in Fig. 3.4(a) by computing $|\sigma - \sigma_{ref}|/|\sigma_{ref}|$ where σ_{ref} is the reference RCS result by running the third-order scheme at a discretization of 400 triangles. The corresponding CPU time for matrix filling is given in Fig. 3.4(b). From the figures, we observe that for the same number of unknowns, the higher-order scheme gives more accurate results and the CPU times are comparable for different order schemes. For small problems, the higher-order schemes have more CPU time because the singular and near interaction terms are relatively dominant. When the problem size becomes large, the higher-order schemes become more efficient than the lower-order ones.

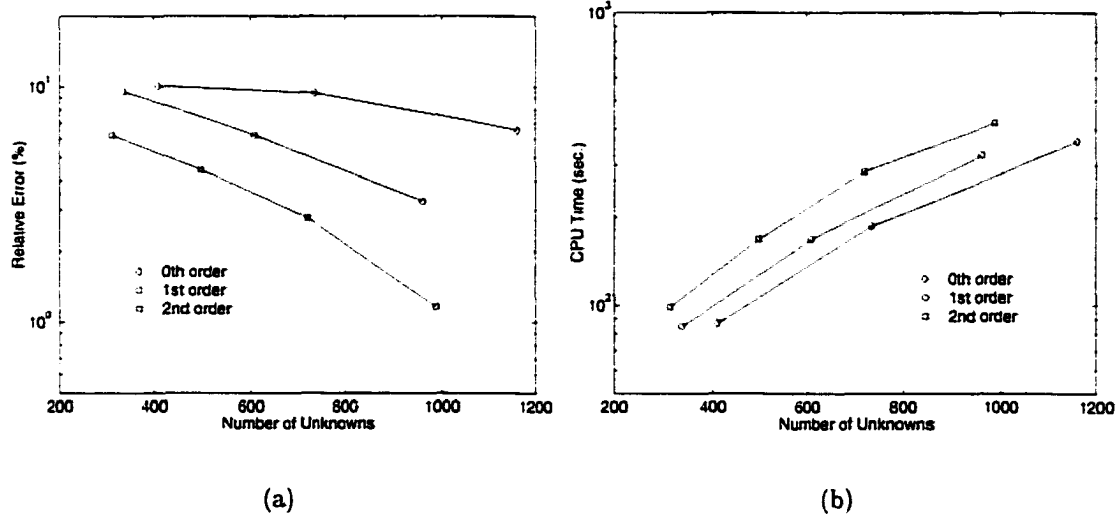


Figure 3.4 Convergence behavior of the high-order basis function. (a) Relative error versus number of unknowns. (b) CPU time versus number of unknowns.

3.4.2 Antenna and circuit examples

The scattering properties of microstrip antennas are investigated first. The rectangular and circular patch antennas are taken as examples. The backscatter RCS $\sigma_{\theta\theta}$ is given in Fig. 3.5 as the function of frequency. The zeroth-, first-, and second-order schemes are employed for a coarse discretization with 24 triangles. As can be seen from Fig. 3.5, the zeroth-order scheme does not give an accurate result,

especially at high frequencies, whereas the first- and second-order schemes converge to the accurate result. The numbers of unknowns for the zeroth-, first-, and second-order approaches are 29, 106, and 231, respectively. The result for the rectangular patch antenna is compared with those from [17]. It is seen that the RCS peaks occur at the frequencies corresponding to the cavity resonant modes. For example, the first two peaks in Fig. 3.5 around 2.7 and 3.7 GHz correspond, respectively, to the first two dominant cavity modes $(1,0)$ and $(0,1)$.

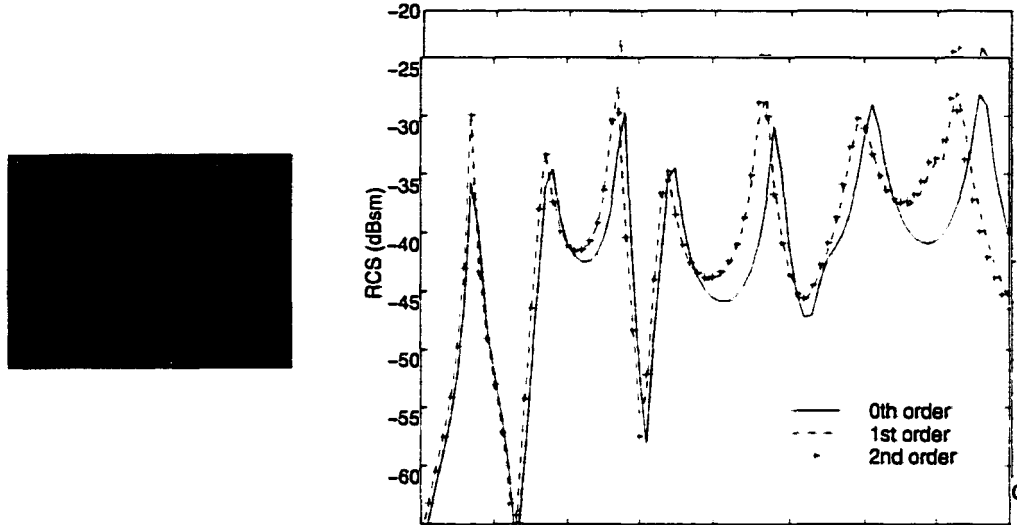


Figure 3.5 Backscatter RCS ($\sigma_{\theta\theta}$) versus frequency for a rectangular microstrip patch antenna. $L = 36.6$ mm, $W = 26$ mm, $h = 1.58$ mm, $\epsilon_r = 2.17$, $\theta^i = 60^\circ$, $\phi^i = 45^\circ$.

The second example is to investigate the reflection and transmission properties of a microstrip periodic filter [81]. The bandgap effect can be achieved from this structure. The coarse discretization is shown in Fig. 3.6(a). The zeroth- and first-order approaches are employed here, which have 273 and 1022 unknowns, respectively. The S-parameters are given by Fig. 3.6(b) and (c), which are in good agreement with those in [81].

As the third example, we consider a proximity-coupled circular patch antenna [21]. The two substrate layers have the same relative permittivity 2.62 and thickness 1.59 mm. The microstrip line is on the bottom layer and the patch is on the top layer. The radius of the patch is 17.5 mm and the width of the microstrip line is 4.372 mm. The overlapping length may be used to control the coupling. Here it is 17.5 mm. The input impedance with the reference plane 79.0 mm away from the patch center is given in Fig. 3.7, which agrees well with the measured data from [21].

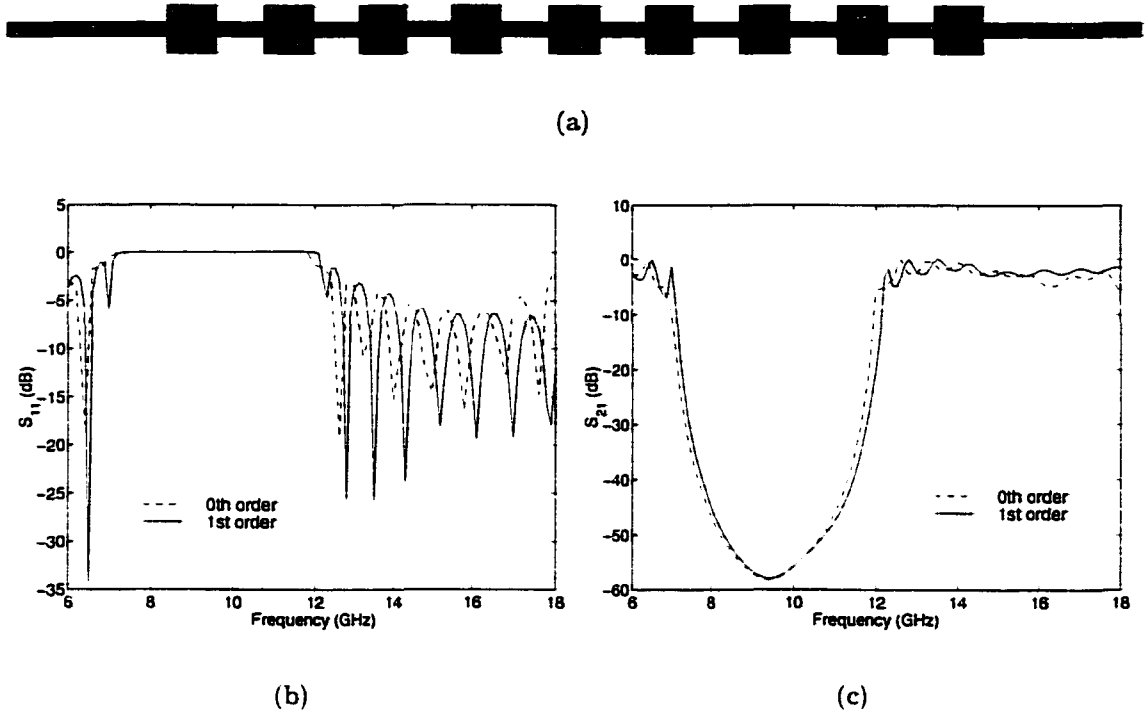
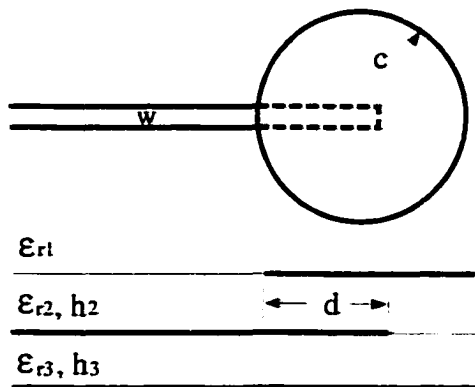


Figure 3.6 S-parameters of a microstrip periodic filter. $\epsilon_r = 10.5$, $h = 0.635$ mm. The line width is 0.686 mm. The patch size is 2.54 mm \times 2.54 mm. The spacing is 5.08 mm.

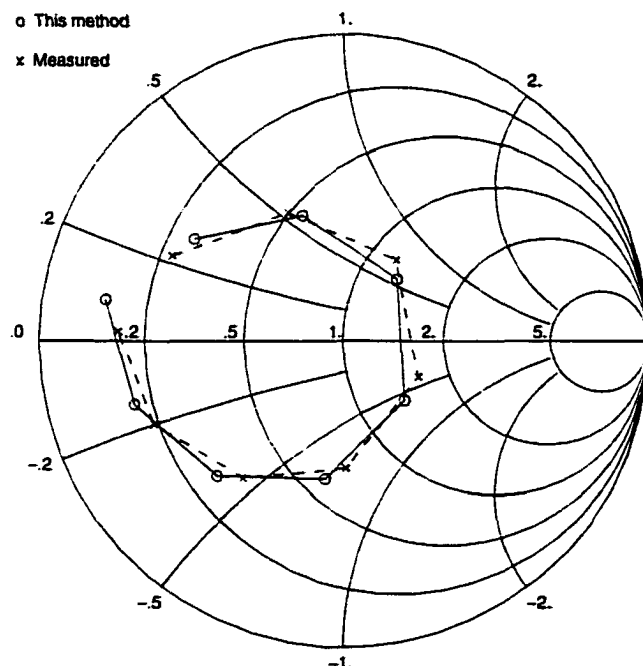
The fourth example presented here is a microstrip meander line [29]. The substrate has the relative permittivity 9.978 and thickness 0.635 mm. The discretization is shown in Fig. 3.8(a). The second-order approach with 597 unknowns is employed. The S-parameters are shown in Fig. 3.8. The measured results from [29] are also presented. An agreement is observed.

The fifth example is a four-port branch line coupler. This structure has been analyzed using the finite-difference time-domain (FDTD) method [3], and it is found difficult for regular FDTD grids to match all of the circuit dimensions exactly. In contrast, all the dimensions in our case are precisely modeled. With the mesh shown in Fig. 3.9, we employ the second-order scheme, which has 968 unknowns. The S-parameters obtained are shown in Fig. 3.9, compared with the measured data from [3]. A good agreement can be seen.

To show advantages of the curvilinear discretization, the sixth example is a four-port annular-ring power-divider, which has been analyzed using the approximated



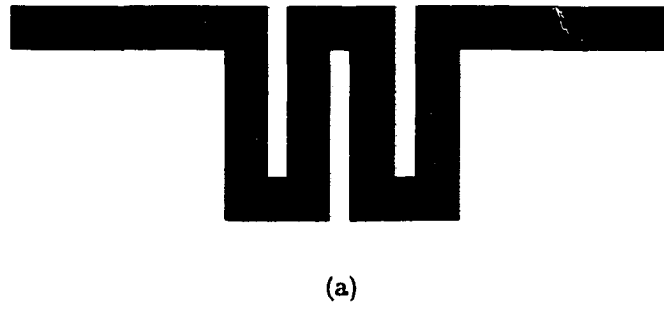
(a)



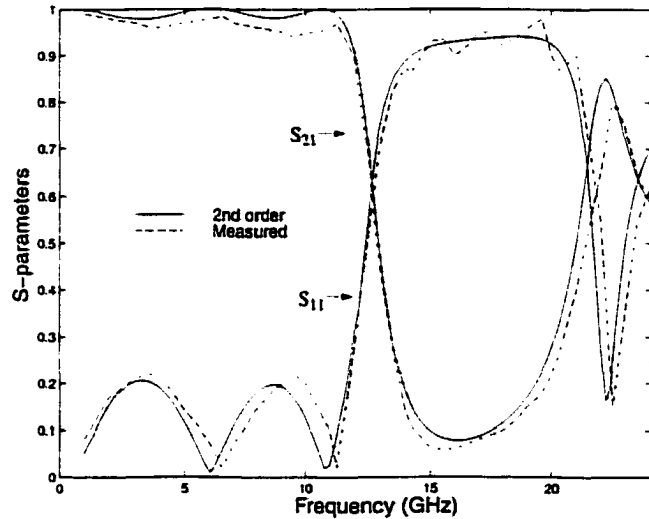
(b)

Figure 3.7 Input impedance for a proximity-coupled microstrip antenna. $\epsilon_{r1} = 1.0$, $\epsilon_{r2} = \epsilon_{r3} = 2.62$, $h_2 = h_3 = 1.59$ mm, $w = 4.372$ mm, $c = 17.5$ mm, $d = 17.5$ mm. The frequency is from 2.80 GHz to 3.15 GHz with increment 0.05 GHz.

planar waveguide models [82]. Here, the circular boundary is precisely modeled by the curvilinear patches, as shown in Fig. 3.10. The numbers of unknowns for the



(a)



(b)

Figure 3.8 Current distributions and S-parameters of microstrip meander line. $\epsilon_r = 9.978$, $h = 0.635$ mm. The line width is 0.61 mm. The gap is 0.305 mm wide and 2.44 mm deep.

zeroth-, first-, and second-order approaches are 172, 612, and 1320, respectively. The second-order results are given in Fig. 3.10, which agrees reasonably with those in [82].

All the above examples have no vertical current so that only one component G_{xx}^A in \bar{K}^A is required to build the impedance matrix. In the next two examples, we will show the capability of the method to deal with the 3-D structures with both horizontal and vertical currents. Both of them are the spiral inductors, one with the

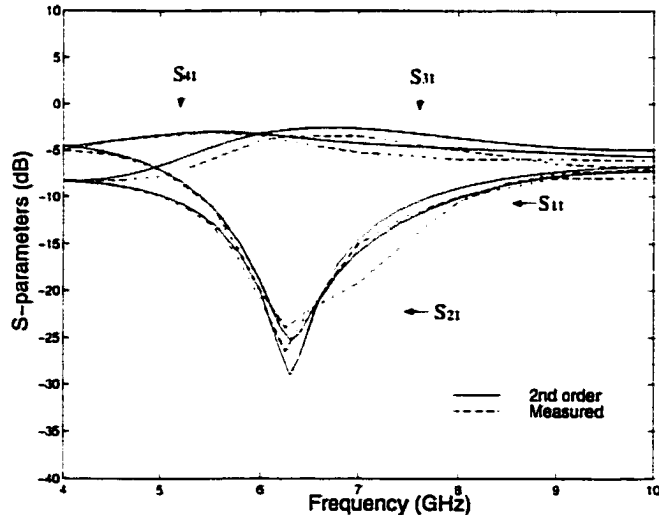
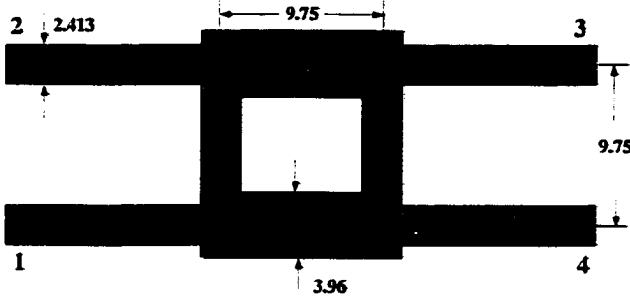


Figure 3.9 S-parameters for a branch line coupler (dimensions in mm). $\epsilon_r = 2.2$, $h = 0.794$ mm.

rectangular shape and the other with curvilinear boundary. The first one is previously analyzed using the FDTD method [8]. In Fig. 3.11, the discretization is shown in (a), the top view of the current distribution at $f = 3.5$ GHz is shown in (b), and the second-order results with 1263 unknowns are given by (c). The S-parameters are in good agreement with those in [8]. The second one is previously calculated using the FEM [12]. The second-order basis functions are employed. To avoid multiple patches sharing a common edge, which is beyond the scope of this chapter, we modify the

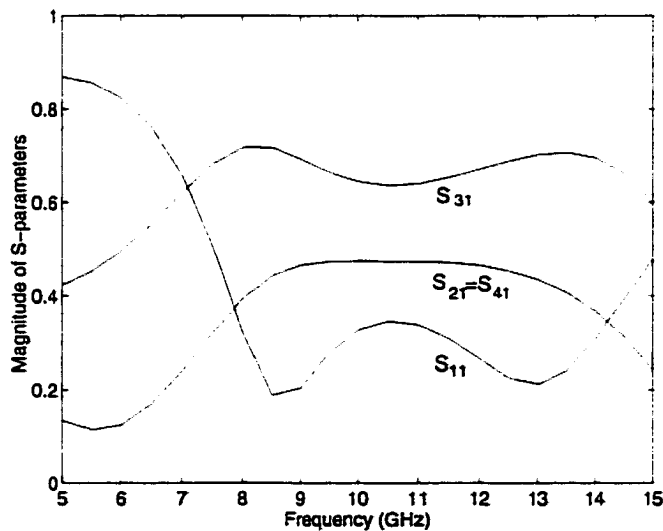
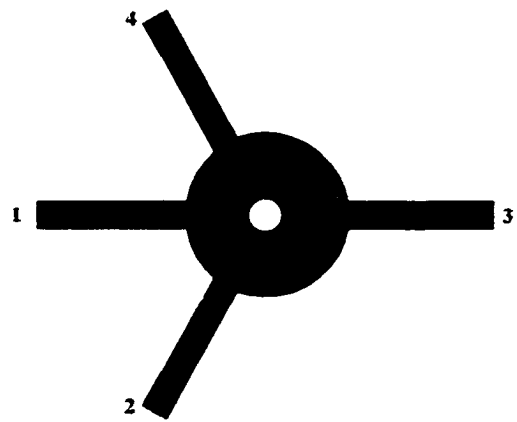


Figure 3.10 S-parameters of an annular-ring power-divider. $\epsilon_r = 2.2$, $h = 0.79$ mm. The line width is 2.4 mm. The inner and outer radii of the annular ring are 1.5 mm and 7.2 mm, respectively. The angle between port 1 and port 2 is 60° .

original structure by shifting the bonding edge of the bridge and the spire from the center to the boundary, which gives the S-parameters in Fig. 3.12, different from those in [12]. However, we still observe a similarity between them.

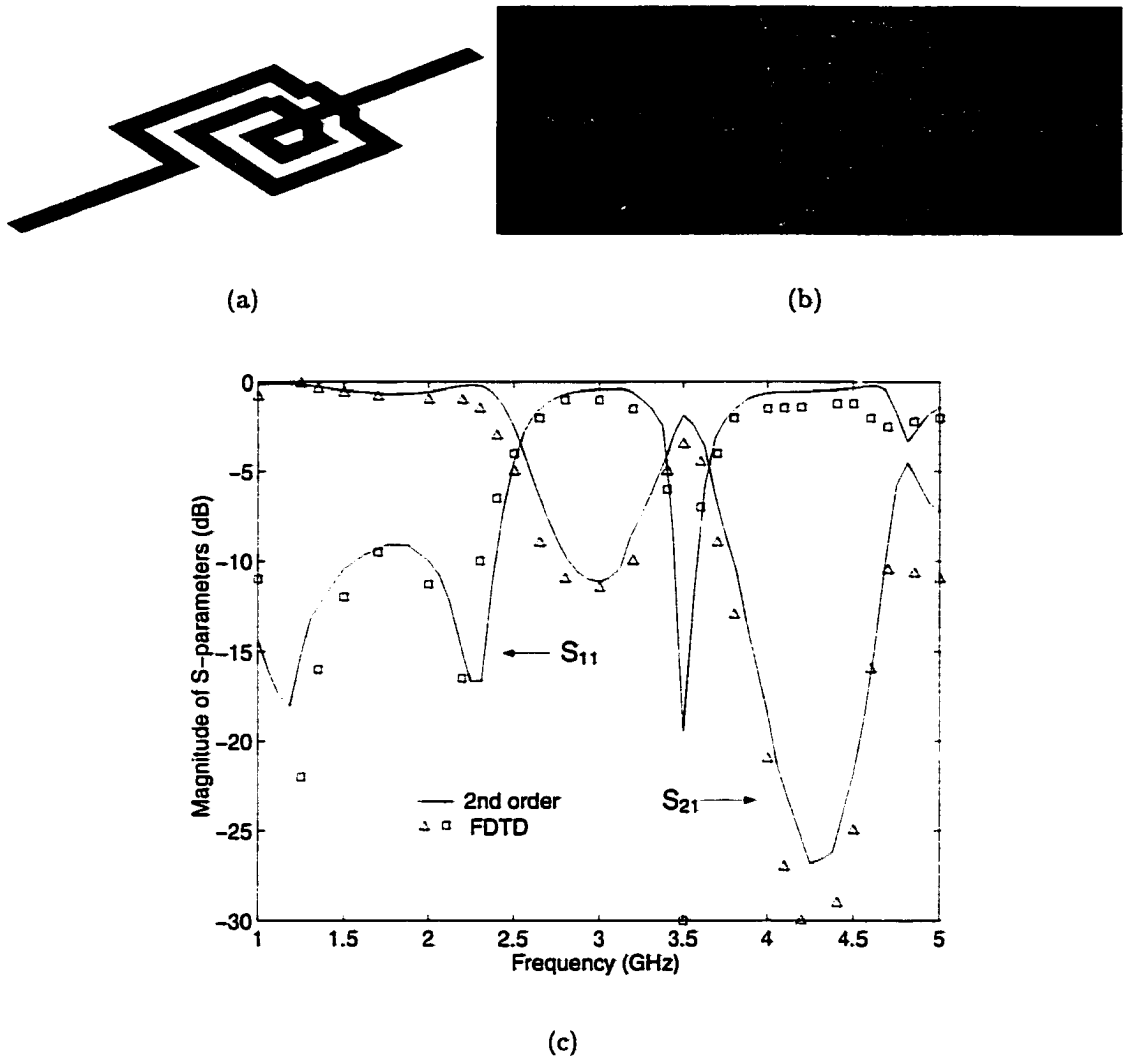
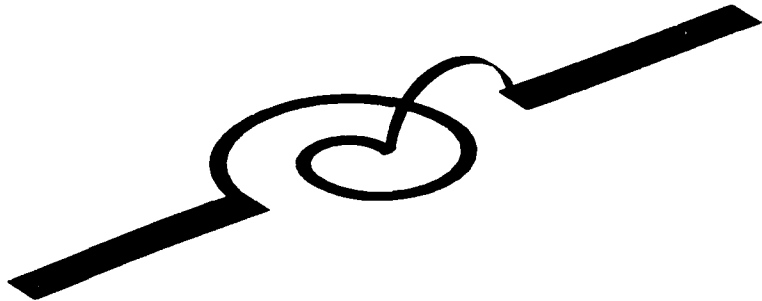


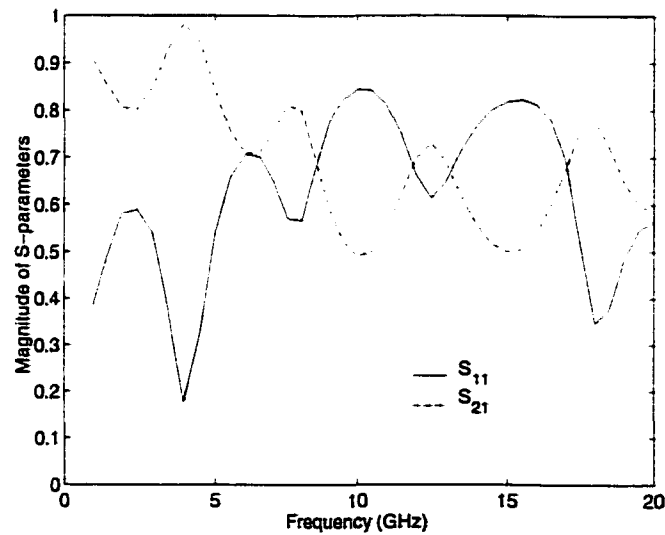
Figure 3.11 S-parameters of a spiral inductor. $\epsilon_r = 9.6$, $h = 2.0$ mm. The line widths and spacings are all 2.0 mm. The height and the span of the air bridges are 1.0 mm and 6.0 mm, respectively.

3.5 Conclusion

Combination of the higher-order interpolatory curvilinear basis functions with the DCIM presented in the previous chapter results in an efficient and accurate MoM solution for microstrip structures in multilayer media. Several antenna and circuit examples are analyzed and good results are obtained.



(a)



(b)

Figure 3.12 S-parameters of a spiral inductor. $\epsilon_r = 9.8$, $h = 0.635$ mm.

CHAPTER 4

REDUCED-ORDER MODEL

4.1 Introduction

The MoM analysis in the previous chapter is implemented in the frequency domain. To obtain frequency responses over a band of interest, we have to repeat the calculation at each discrete frequency. This can be computationally intensive for electromagnetic devices with complicated frequency responses. For this reason, several different techniques have been proposed to characterize the device by using the reduced-order model, such as the asymptotic waveform evaluation (AWE) [85], the complex frequency hopping (CFH) [86], and the Padé via Lanczos (PVL) [87], [88]. All of them were originally developed in the circuit community. The basic idea of these techniques is to approximate the frequency response, or the transfer function, by a low-order rational function, the Padé approximant. In AWE and CFH, the Padé approximant of the frequency response is obtained by the moment matching process. In PVL, the Padé approximant is obtained by the Lanczos process so that the direct calculation of moments is eluded. Recently, these techniques have been extended for electromagnetic analysis [89]–[92]. A parallel effort ongoing in the electromagnetic community is the development of the model-based parameter estimation (MBPE) [93], [94]. Instead of matching moments in AWE, MBPE matches the derivatives of the transfer function to find the Padé approximant.

Although PVL is more stable than AWE, the algorithm requires the submatrices to be frequency independent. This is not the case in MoM since the submatrices are frequency dependent through the Green's functions. Therefore, the AWE is employed in this work to achieve the fast frequency sweep. The unknown current is first expanded as a Taylor series at the expansion point. The Taylor series coefficients, or the moments, are associated with the frequency derivatives of the impedance matrix, which can be derived because of the use of the DCIM. The Padé approximant is then obtained by matching the moments. The response over a frequency band near the expansion point can be easily obtained. To obtain the broadband response, more expansion points are required. A simple binary search algorithm, as proposed in [89],

is employed to automatically determine the expansion points and obtain the accurate solution over the entire broadband.

In this chapter, we apply the AWE to the MoM solution of microstrip structures in multilayer media so that the computation of frequency response over a bandwidth is expedited. Numerical results show the speedup of AWE.

4.2 AWE Implementation

The MoM solution can be achieved by solving (3.12). Given a frequency band, we have to repeat the solution of (3.12) at a set of frequencies. For structures with a highly oscillatory frequency response, this process is computationally expensive. Several techniques to realize the fast frequency sweep have been developed, such as MBPE, AWE, CFH, and PVL. The basic principle of these techniques is to extract the dominant poles and residues of the frequency response and represent it by a reduced-order model, which is accomplished by constructing the Padé approximant of the frequency response.

In AWE, the solution of (3.12) can be expanded as a Taylor series at a given frequency point ω_0

$$\mathbf{I}(\omega_0 + \sigma) = \sum_{n=0}^{\infty} \mathbf{M}_n \sigma^n \quad (4.1)$$

where \mathbf{M}_n is the n th moment vector and is given by

$$\mathbf{M}_n = \frac{1}{n!} \left. \frac{\partial^n}{\partial \omega^n} [\bar{\mathbf{Z}}^{-1}(\omega) \mathbf{V}] \right|_{\omega=\omega_0} \quad (4.2)$$

The moments can be evaluated by the recursive relation

$$\bar{\mathbf{Z}}(\omega_0) \mathbf{M}_n = - \sum_{r=1}^n \frac{1}{r!} \left. \frac{\partial^r}{\partial \omega^r} \bar{\mathbf{Z}}(\omega) \right|_{\omega=\omega_0} \mathbf{M}_{n-r} \quad (4.3)$$

with the initial vector

$$\mathbf{M}_0 = \bar{\mathbf{Z}}^{-1}(\omega_0) \mathbf{V} \quad (4.4)$$

To overcome the problem associated with the radius of convergence of the Taylor series expansion, the Padé approximant of $\mathbf{I}(\omega_0 + \sigma)$ is used, which can be written as

$$\mathbf{I}(\omega_0 + \sigma) = \frac{\mathbf{a}_0 + \mathbf{a}_1 \sigma + \dots + \mathbf{a}_p \sigma^p}{1 + \mathbf{b}_1 \sigma + \dots + \mathbf{b}_q \sigma^q} \quad (4.5)$$

where typically $p = q - 1$ and the $p + q + 1$ unknown coefficients of the numerator and denominator are uniquely determined by matching the first $p + q + 1$ moments of (4.1), as done in [89] and [90]. Once we obtain the Padé approximant, the frequency response over a frequency band can be rapidly evaluated.

Therefore, the first step of AWE is to evaluate the derivative matrices at the expansion point. As we know, the impedance matrix is the function of frequency through the Green's functions. Unlike in [94], the Green's functions in this method have the simple expression $\frac{e^{-jkr}}{r}$ due to the use of the DCIM. Therefore, the derivative matrices here can be simply formulated. Then the moment vectors can be obtained recursively by (4.3). After the moment matching process, the Padé approximant for each element can be obtained. Therefore, the frequency response over a band near the expansion point is obtained.

In many practical problems with broadband response, one expansion point is not sufficient to cover the entire bandwidth. In such cases, multiple expansion points are necessary. Here, a simple binary search algorithm, as described in [89], is employed to automatically choose the expansion points. Assume that we are interested in the frequency response over the band $[f_{min}, f_{max}]$. We first compute the reduced-order models using f_{min} and f_{max} as two different expansion points. We then compute the frequency response over the entire band $[f_{min}, f_{max}]$. If the two responses are within an acceptable error tolerance, the procedure has converged. If not, an additional reduced-order model is then computed at a new expansion point $(f_{min} + f_{max})/2$, and the error checking process is repeated in the two new subintervals. This process is repeated until the two reduced-order models bordering all subintervals give the frequency responses within the prescribed error tolerance.

It is known that AWE has the problem of instability in the computation of the Padé approximation due to the ill-conditioned moment-matching process [87]. However, this is not a problem in our method because the order of the Padé approximant is typically chosen as $q \leq 8$, for which the instability has never been observed.

4.3 Numerical Results

In the next three examples, AWE is applied to expedite the calculation of frequency response over a bandwidth. In all the cases, we use $q = 8$. The CPU time using AWE is compared with that employing the direct calculation to demonstrate the efficiency, as shown in Table 4.1. We first consider a microstrip double-stub on a single layer, which has the relative permittivity $\epsilon_r = 9.9$ and the thickness 0.127 mm [42], [44]. The number of unknowns is 205. Current distributions at two different frequencies are shown in Figs. 4.1(a) and 4.1(b). The direct calculation gives a very good result comparing with the measured data [42], [44], as shown in Fig. 4.1(c). In

Table 4.1 Comparison of the CPU time using the direct calculation and AWE

	Direct			AWE			Speed-up
	T_{freq} (sec)	N_{freq}	T_1 (sec)	T_{expn} (sec)	N_{expn}	T_2 (sec)	
Ex. 1	6.4	60	384.0	18.1	1	18.1	21.2
Ex. 2	104.0	80	8320.0	350.2	3	1050.6	7.9
Ex. 3	27.0	400	10800.0	95.9	9	863.1	12.5

T_{freq} : CPU time per frequency in the direct calculation;

N_{freq} : Number of frequencies in the direct calculation;

T_1 : Total CPU time by the direct calculation;

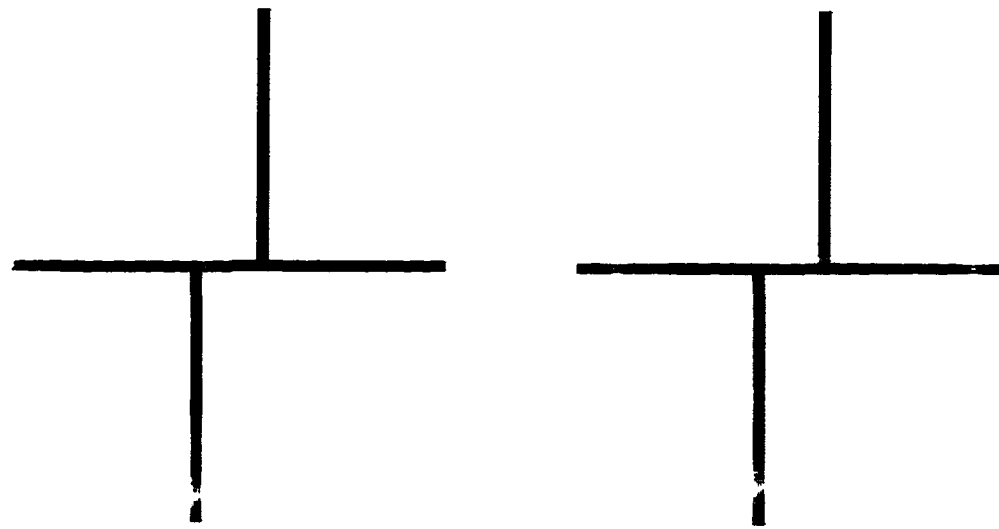
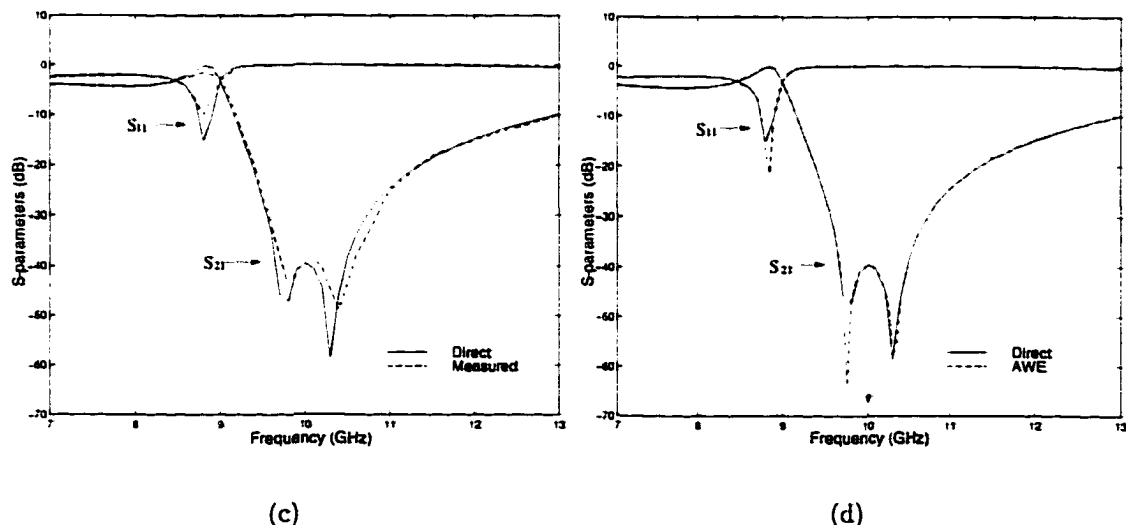
T_{expn} : CPU time per expansion point with AWE;

N_{expn} : Number of expansion points with AWE;

T_2 : Total CPU time with AWE.

this calculation, the CPU time at each frequency is 6.4 s and a total of 60 frequencies are sampled to obtain the accurate results. Therefore the total CPU time is 384 s. Using AWE and choosing only one expansion point $f = 10.0$ GHz, we can obtain a very good result, as given by Fig. 4.1(d). In the calculation with AWE, the CPU time is 18.1 s. Thus, using AWE is approximately 21 times faster. Note that the sampling points are not dense enough to catch the null at about 9.75 GHz for the direct calculation.

We next consider a two-port asymmetric antenna [48]. There are two orthogonally crossed dipoles on the top layer. They have the different lengths so that dual frequency operation is achieved. The transversal one has length 11.9 mm and the longitudinal one has length 10.2 mm. The width of both is 1.7 mm. The two substrate layers have the same relative permittivity $\epsilon_r = 2.17$. The top layer has thickness 1.6 mm and the bottom layer has thickness 0.8 mm. On the bottom layer, the feeding lines are 2.2 mm wide. Fed from port 1, the longitudinal dipole is excited at the resonant frequency of 8.4 GHz. The current distribution is given in Fig. 4.2(a). Fed from port 2, the transversal dipole is excited at its resonant frequency 9.6 GHz. The current is shown in Fig. 4.2(b). At 11.3 GHz, the coupling bend consisting of two perpendicular half-dipoles is resonant. The incident power is essentially transmitted from one port to the other, and the current distribution is shown in Fig. 4.2(c).

(a) $f=10.0$ GHz(b) $f=13.0$ GHz

(c)

(d)

Figure 4.1 Current distributions and S-parameters for a microstrip double-stub. $\epsilon_r = 9.9$, $h = 0.127$ mm. The line width is 0.122 mm. The stub length is 2.921 mm. The spacing between two stubs is 0.757 mm.

The magnitude of S-parameters is given in Fig. 4.2(d). The measured data are available from [48]. Good agreement can be observed. In this example, the number of unknowns is 912. The direct method takes 104 s for each frequency, and a total of 80 sampling frequencies are used to obtain the accurate results. Therefore, the total

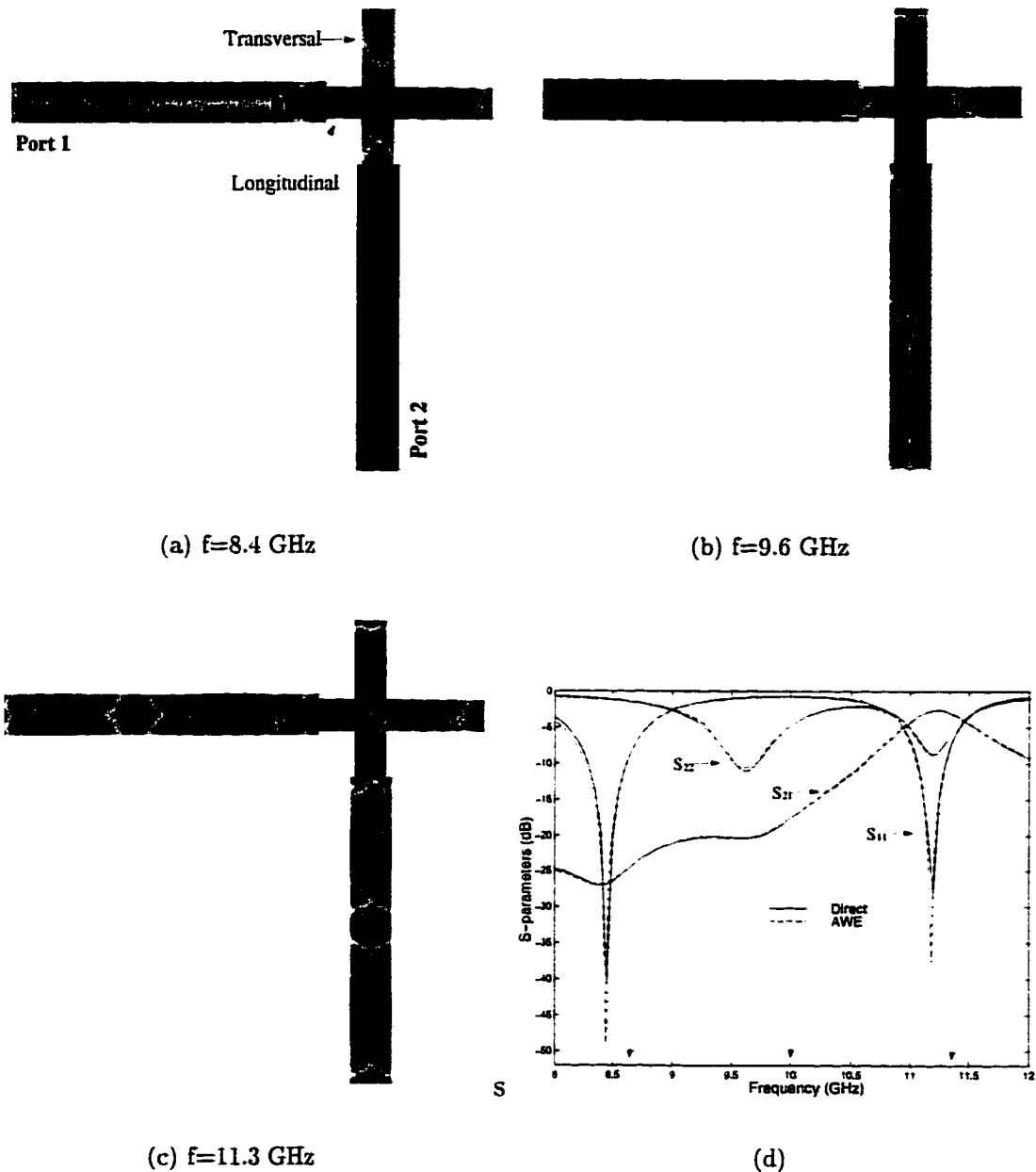
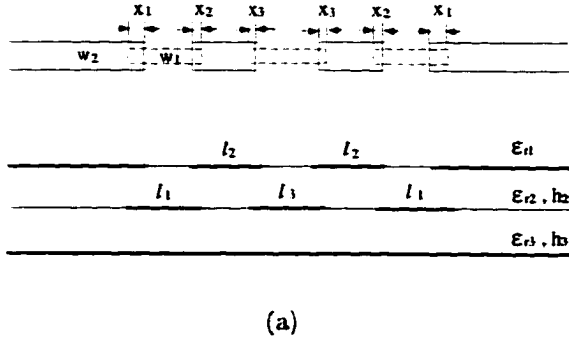


Figure 4.2 Current distributions and S-parameters for a two-port asymmetric antenna.

CPU time is about 139 min. In contrast, with AWE only three expansion frequencies are needed. At each expansion point, the CPU time is 350.2 s. Totally, the CPU time is 17.5 min. Thus, using AWE is approximately 8 times faster.

The last example is an overlap-gap-coupled microstrip filter [50], [79], illustrated



(a)

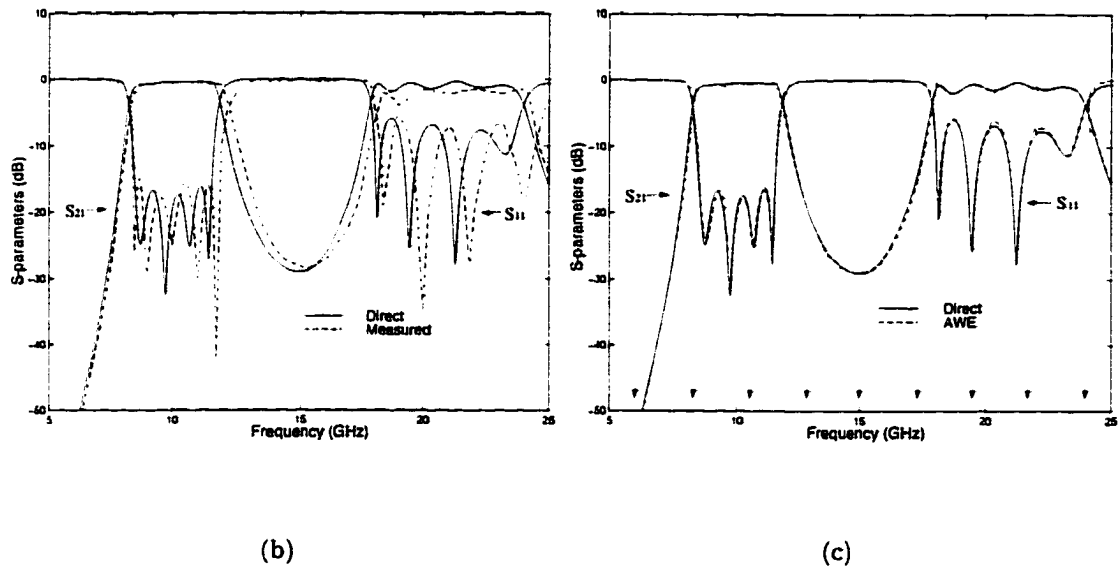


Figure 4.3 S-parameters for an overlap-gap-coupled microstrip filter. $\epsilon_{r1} = 1.0$, $\epsilon_{r2} = 9.8$, $\epsilon_{r3} = 2.2$, $h_2 = h_3 = 0.01$, $l_1 = 0.2752$, $l_2 = 0.2542$, $l_3 = 0.2851$, $x_1 = 0.0516$, $x_2 = 0.0152$, $x_3 = 0.0106$. Unit of dimension: inch.

in Fig. 4.3(a). It is a two-layer geometry. The top layer is alumina with relative permittivity 9.8 and thickness 0.254 mm. The bottom layer is duroid with relative permittivity 2.2 and thickness 0.254 mm. The geometrical parameters are the same as those in [79]. The number of unknowns is 503. In the direct calculation, the CPU time at each frequency is 27 s and a total of 400 sampling frequencies are used to obtain the accurate results. Therefore, the total CPU time is approximately 3 h. The computed S-parameters in comparison with the measured data are shown in Fig. 4.3(b). The small discrepancy with the measured data is due to the finite thickness of metalization and the manufacturer's tolerance of substrates, as discussed

in [50] and [79]. In contrast, with AWE only nine expansion frequencies are chosen automatically by the binary search. At each expansion point, the CPU time is 95.9 s. The CPU time totals 863.1 s. Thus, the method with AWE is approximately 12.5 times faster than the direct calculation. The results without and with AWE agree excellently, as shown in Fig. 4.3(c).

4.4 Conclusion

In this chapter, the AWE is applied to the MoM solution of microstrip structures in multilayer media so that the reduced-order model is obtained for efficient evaluation of the frequency response over a broadband. Some multilayer circuits and antennas are analyzed to demonstrate the efficiency of this technique.

CHAPTER 5

ADAPTIVE INTEGRAL METHOD

5.1 Introduction

To simulate large-scale microstrip problems, it is often necessary to employ a large number of unknowns. For the conventional MoM, whether in the spectral or the spatial domain, the memory requirement is always proportional to $O(N^2)$, where N denotes the number of unknowns. This requirement can easily become prohibitive even on the most powerful computers. Even if the memory permits, the computing time can become very excessive because direct matrix inversion solvers, such as Gaussian elimination and *LU* decomposition methods, require $O(N^3)$ floating-point operations. When an iterative solver such as the conjugate gradient (CG) method is employed for solving the MoM matrix equation, the operation count is $O(N^2)$ per iteration because of the need to evaluate the matrix-by-vector product. This operation count is still too high for an efficient simulation. To make the iterative method more efficient, it is necessary to speed up the matrix-vector multiplication. As reviewed in Chapter 1, three fast schemes have been developed. In this thesis, two fast schemes are investigated and extended to microstrip structures. This chapter deals with the AIM. In the next chapter, the FMM will be discussed.

By exploiting the translational invariance of the Green's function, the matrix-by-vector product can be computed using the FFT. When this is combined with the CG method, the resulting algorithm is called the conjugate gradient fast Fourier transform (CGFFT) method [95]–[103]. Several different schemes of CGFFT have been implemented in the past, which differ primarily in the treatment of the Green's function and the del operators. A review of those works reveals that the spatially discretized Green's functions can eliminate the aliasing and truncation errors and the transfer of the del operators to the basis and testing functions can improve the accuracy and efficiency [101]–[103]. The resulting algorithm is suitable for analysis of large-scale problems because the CPU time per iteration is of $O(N \log N)$ and the memory requirement is of $O(N)$. However, CGFFT requires the uniform discretization to make use of the translational invariance of the Green's functions.

This limits the applicability of the method to complex geometries and results in a staircase approximation for curved boundaries. Meanwhile, it is well-known that the triangular discretization with the RWG basis functions provides a great capability to model arbitrary shapes [73]. But the triangular discretization does not allow the application of FFT to speed up the matrix-vector multiplication. The approach to overcome this problem is the adaptive integral method.

The basic principle of this method is to translate the triangular basis function onto a regular Cartesian grid and then to utilize FFT to carry out the matrix-vector multiplication. This idea was originally proposed by Bleszynski et al. for solving the scattering and radiation problems [104], [105]. It was later extended to large-scale microstrip structures [107], where the DCIM is employed to accelerate the computation of the spatial domain Green's functions. Similar approaches include the sparse-matrix/canonical grid method [108] and the precorrected-FFT method [109].

In this chapter, we first review the basic principle of AIM and describe how the triangular basis functions can be translated to the Cartesian grids and how FFT can be applied to calculate the matrix-by-vector product. Then, we apply this general procedure to some realistic problems. Finally, the numerical results for some microstrip structures are presented to demonstrate the efficiency and accuracy of the AIM.

5.2 AIM Formulation

To employ AIM to accelerate the matrix-vector multiplication, one first encloses the whole structure in a rectangular region and then recursively subdivides it into small rectangular grids, as illustrated in Fig. 5.1. Then the original basis functions on the triangular elements are translated to the rectangular grids.

Denote the RWG basis function as \mathbf{f}_i and rewrite the impedance matrix element

$$Z_{ij} = -j\omega\mu_0 \iint_{T_i} \iint_{T_j} \left[\mathbf{f}_i(\mathbf{r}) \cdot \mathbf{f}_j(\mathbf{r}') G_{xx}^A(\mathbf{r}, \mathbf{r}') - \frac{1}{k_0^2} \nabla \cdot \mathbf{f}_i(\mathbf{r}) \nabla' \cdot \mathbf{f}_j(\mathbf{r}') G^\Phi(\mathbf{r}, \mathbf{r}') \right] d\mathbf{r}' d\mathbf{r} \quad (5.1)$$

If any one of the Cartesian components of $\mathbf{f}_i(\mathbf{r})$ and $\nabla \cdot \mathbf{f}_i(\mathbf{r})$ is denoted as $\psi_i(\mathbf{r})$, the impedance matrix element of (5.1) can be expressed as a linear combination of

matrix elements in the form of

$$A_{ij} = \iint_{T_i} \iint_{T_j} \psi_i(\mathbf{r}) g(\mathbf{r}, \mathbf{r}') \psi_j(\mathbf{r}') d\mathbf{r}' d\mathbf{r} \quad (5.2)$$

where g can be either G_{xx}^A or G^Φ . $\psi_i(\mathbf{r})$ can be approximated as a combination of the Dirac delta functions on the rectangular grids:

$$\psi_i(\mathbf{r}) \simeq \hat{\psi}_i(\mathbf{r}) = \sum_{u=1}^{(M+1)^2} \Lambda_{iu} \delta(\mathbf{r} - \mathbf{r}_{iu}) \quad (5.3)$$

where Λ_{iu} is the translation coefficient for the basis function $\psi_i(\mathbf{r})$, M is the order of the translation, and $\mathbf{r}_{iu} = (x_{iu}, y_{iu})$ is the coordinate of the grid.

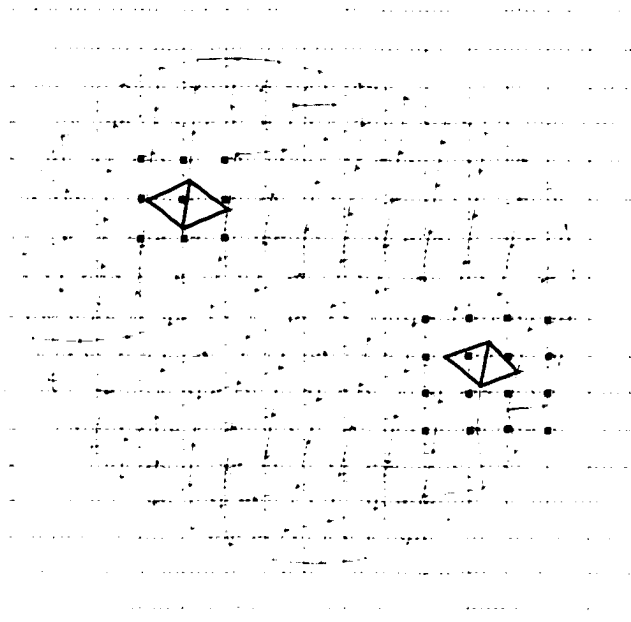


Figure 5.1 Translation of RWG basis functions to rectangular grids. The highlighted triangular basis function on the left is approximated by $(M + 1)^2 = 9$ rectangular grids. The highlighted triangular basis function on the right is approximated by $(M + 1)^2 = 16$ rectangular grids.

The translation coefficient can be found based on the criterion that the translated basis function produces the same multipole moments as the original basis function

$$\sum_{u=1}^{(M+1)^2} (x_{iu} - x_0)^{q_1} (y_{iu} - y_0)^{q_2} \Lambda_{iu} = \iint_{T_i} \psi_i(\mathbf{r}) (x - x_0)^{q_1} (y - y_0)^{q_2} d\mathbf{r} \quad \text{for } 0 \leq q_1, q_2 \leq M \quad (5.4)$$

where the reference point $\mathbf{r}_0 = (x_0, y_0)$ is chosen as the center of the basis function. The closed-form solution of (5.4) has been given by Bleszynski et al. [105].

Once this translation is found, we can approximate the matrix element of (5.2) as

$$\hat{A}_{ij} = \sum_{u=1}^{(M+1)^2} \sum_{v=1}^{(M+1)^2} \Lambda_{iu} g(\mathbf{r}_u, \mathbf{r}'_v) \Lambda_{jv} \quad (5.5)$$

With the translation formula given above, we can now rewrite the impedance matrix element in the form of (5.1) as

$$\hat{Z}_{ij} = -j\omega \sum_{u=1}^{(M+1)^2} \sum_{v=1}^{(M+1)^2} \left[(\Lambda_{x,iu} \Lambda_{x,jv} + \Lambda_{y,iu} \Lambda_{y,jv}) G_{xx}^A(\mathbf{r}_u, \mathbf{r}'_v) - \frac{1}{k_0^2} \Lambda_{d,iu} \Lambda_{d,jv} G^\Phi(\mathbf{r}_u, \mathbf{r}'_v) \right] \quad (5.6)$$

where Λ_x , Λ_y and Λ_d denote the translation coefficients for the x -component, the y -component, and the divergence of the basis function, respectively.

\hat{Z}_{ij} in (5.6) offers a good accuracy to approximate Z_{ij} in (5.1) when the basis and testing functions are at a sufficiently large distance. The significant error which occurs when the basis and testing functions are close to each other is compensated for by introducing a residual matrix $\bar{\mathbf{R}}$. Therefore, the impedance matrix is decomposed into

$$\bar{\mathbf{Z}} = \hat{\mathbf{Z}} + \bar{\mathbf{R}} \quad (5.7)$$

Note that only when \mathbf{f}_i and \mathbf{f}_j are very close does R_{ij} have an appreciable value, which makes the residual matrix $\bar{\mathbf{R}}$ very sparse. In matrix form, $\hat{\mathbf{Z}}$ can be written as

$$\hat{\mathbf{Z}} = j\omega \left[\bar{\Lambda}_x \bar{\mathbf{G}}_{xx}^A \bar{\Lambda}_x^T + \bar{\Lambda}_y \bar{\mathbf{G}}_{yy}^A \bar{\Lambda}_y^T - \frac{1}{k_0^2} \bar{\Lambda}_d \bar{\mathbf{G}}^\Phi \bar{\Lambda}_d^T \right] \quad (5.8)$$

where $\bar{\Lambda}_x$, $\bar{\Lambda}_y$, and $\bar{\Lambda}_d$ are sparse matrices with each row containing only $(M+1)^2$ non-zero elements. The translational invariance of $\bar{\mathbf{G}}_{xx}^A$ and $\bar{\mathbf{G}}^\Phi$ enables the use of FFT to accelerate the computation of the product of this matrix $\hat{\mathbf{Z}}$ with a vector. These features make the algorithm less demanding memory and CPU time. Employing the CG method as the iterative solver, one can write the matrix-vector multiplication as

$$\bar{\mathbf{Z}} \cdot \mathbf{I} = \hat{\mathbf{Z}} \cdot \mathbf{I} + \bar{\mathbf{R}} \cdot \mathbf{I} \quad (5.9)$$

where $\hat{\mathbf{Z}} \cdot \mathbf{I}$ can be evaluated using FFT as

$$\begin{aligned} \hat{\mathbf{Z}} \cdot \mathbf{I} = j\omega & \left\{ \bar{\Lambda}_x \mathcal{F}^{-1} [\mathcal{F}(\bar{\mathbf{G}}_{xx}^A) \cdot \mathcal{F}(\bar{\Lambda}_x^T \mathbf{I})] + \bar{\Lambda}_y \mathcal{F}^{-1} [\mathcal{F}(\bar{\mathbf{G}}_{yy}^A) \cdot \mathcal{F}(\bar{\Lambda}_y^T \mathbf{I})] \right. \\ & \left. - \frac{1}{k_0^2} \bar{\Lambda}_d \mathcal{F}^{-1} [\mathcal{F}(\bar{\mathbf{G}}^\Phi) \cdot \mathcal{F}(\bar{\Lambda}_d^T \mathbf{I})] \right\} \end{aligned} \quad (5.10)$$

As we can see from the analysis described above, the memory requirement of AIM is proportional to $O(N)$ due to the sparsity of matrices $\bar{\mathbf{R}}$, $\bar{\Lambda}_x$ and $\bar{\Lambda}_y$. The CPU time

per iteration is dominated by the FFT computation of the matrix-by-vector product, which is proportional to $O(N \log N)$. In contrast, for the conventional MoM, the CPU time for the matrix fill is of $O(N^2)$ and the CPU time per iteration is also of $O(N^2)$.

5.3 Accuracy and Complexity

The accuracy of the AIM is first examined. Consider a microstrip line on a substrate with relative permittivity $\epsilon_r = 2.17$ and thickness $h = 1.58$ mm. The frequency is 3.0 GHz. The line is 5 mm wide and 400 mm long, as seen from Fig. 5.2(a). Enclose the line by rectangular grids with the grid size being 6.25 mm. Matrix elements calculated by using (5.1) and (5.6) are compared in Fig. 5.2(b) where $M = 3$ is chosen. The relative error is also given, which is defined as

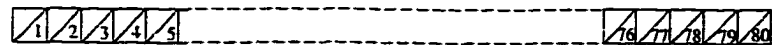
$$\Delta_{ij} = \frac{|Z_{ij} - \hat{Z}_{ij}|}{|Z_{ij}|} \quad (5.11)$$

Figure 5.2(c) gives the relative errors for $M = 1$ and $M = 3$, which shows that the accuracy increases with the increase of M .

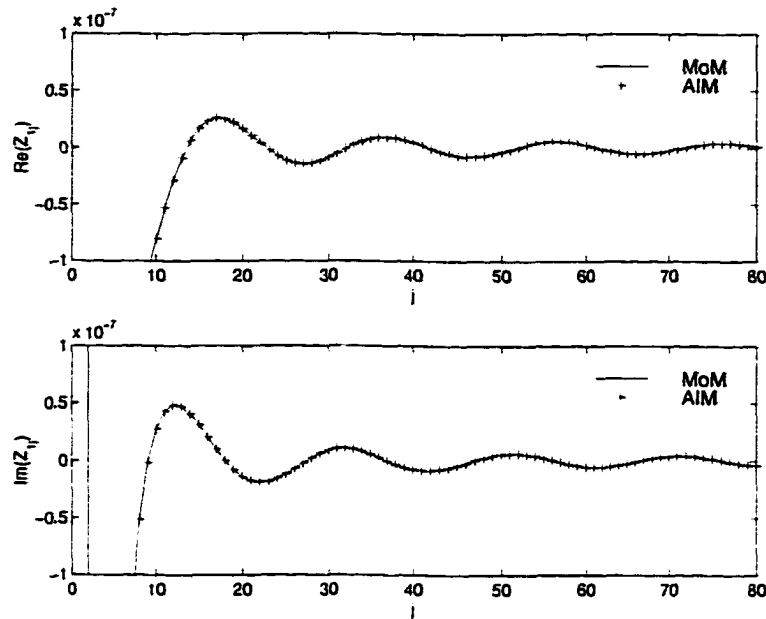
Next, the complexity of this algorithm is evaluated. The CPU time per iteration and the memory requirement versus the number of unknowns are plotted by considering a rectangular microstrip patch on the substrate with relative permittivity $\epsilon_r = 2.17$ and thickness $h = 1.58$ mm. The frequency is 3.0 GHz. The patch is discretized with 20 unknowns per wavelength λ_0 . It is seen from Fig. 5.3 that the CPU time per iteration is scaled as $O(N \log N)$ and the memory requirement is scaled as $O(N)$.

5.4 Numerical Results

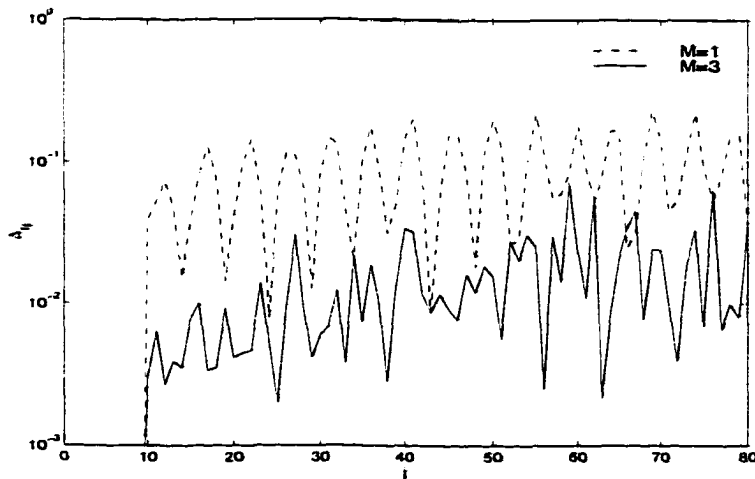
We first consider some simple circuits for the verification purpose. The first example is a microstrip radial stub analyzed in [83]. The substrate has permittivity $\epsilon_r = 10.0$ and thickness $h = 0.635$ mm. To cover the entire frequency band, we consider two different discretizations. The first one is for lower frequencies (below 8 GHz), which involves 364 facets and 457 edges. The microstrip line is truncated at the distance 16.5 mm from the center to make the S -parameter extraction accurate. The other discretization is for higher frequencies, which involves 862 facets and 1194 edges. To provide physical insight into the performance of the stub, we show the current distribution on the surface at two frequencies, $f = 8.0$ GHz and $f = 12.0$



(a)



(b)



(c)

Figure 5.2 Matrix elements Z_{ij} ($j = 1, 2, \dots, 80$) calculated by the conventional MoM and the AIM.

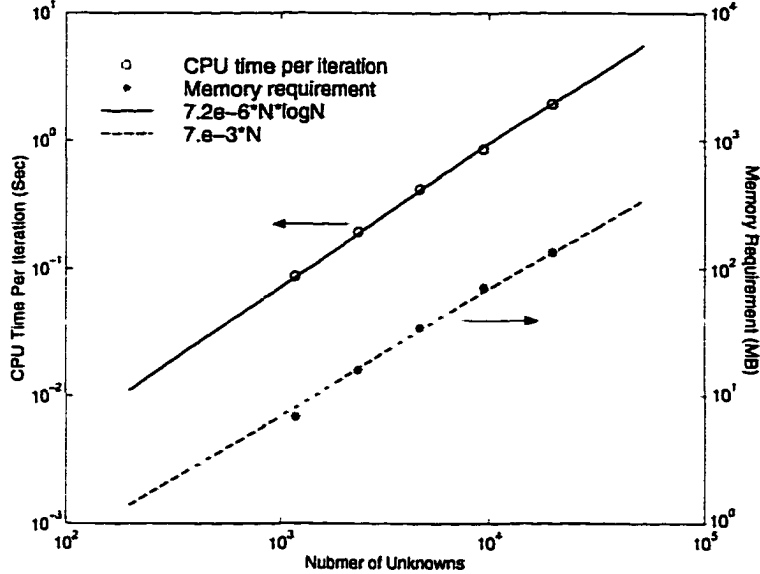


Figure 5.3 Complexity of the AIM. The CPU time per iteration is close to $9 \times 10^{-6} N \log N$ and the memory requirement is close to $7 \times 10^{-3} N$.

GHz. The stub is excited at the left port, and the other port is left open. We can see that most energy is reflected at $f = 8.0$ GHz, and is transmitted to the other port at $f = 12.0$ GHz. The S -parameters from the proposed method and MoM are given in Fig. 5.4, which shows a good agreement between two methods. The agreement between our results and the measured data from [83] is also satisfactory.

The second example is a parallel-coupled bandpass filter. The dimension of the filter is given by Fig. 8.26 in [84]. The substrate has permittivity $\epsilon_r = 10.0$ and thickness $h = 0.635$ mm. The numbers of facets and unknowns are 1086 and 1402, respectively. Again, the current distributions are shown at $f = 9.0$ GHz and $f = 11.0$ GHz. The S -parameters of this bandpass filter are shown in Fig. 5.5. Both MoM and AIM results agree very well. The measured data from [84] are also given in Fig. 5.5 for comparison. The discrepancy at the low frequency range is believed due to the fabrication error.

The examples above demonstrate the accuracy of this algorithm. Because the structures analyzed are relatively small (the number of unknowns is below 2000), the saving of CPU time is not expected, although the significant memory reduction has been achieved. For large-scale problems, we can predict a substantial reduction of CPU time in both the matrix fill and the matrix solve. To illustrate the efficiency

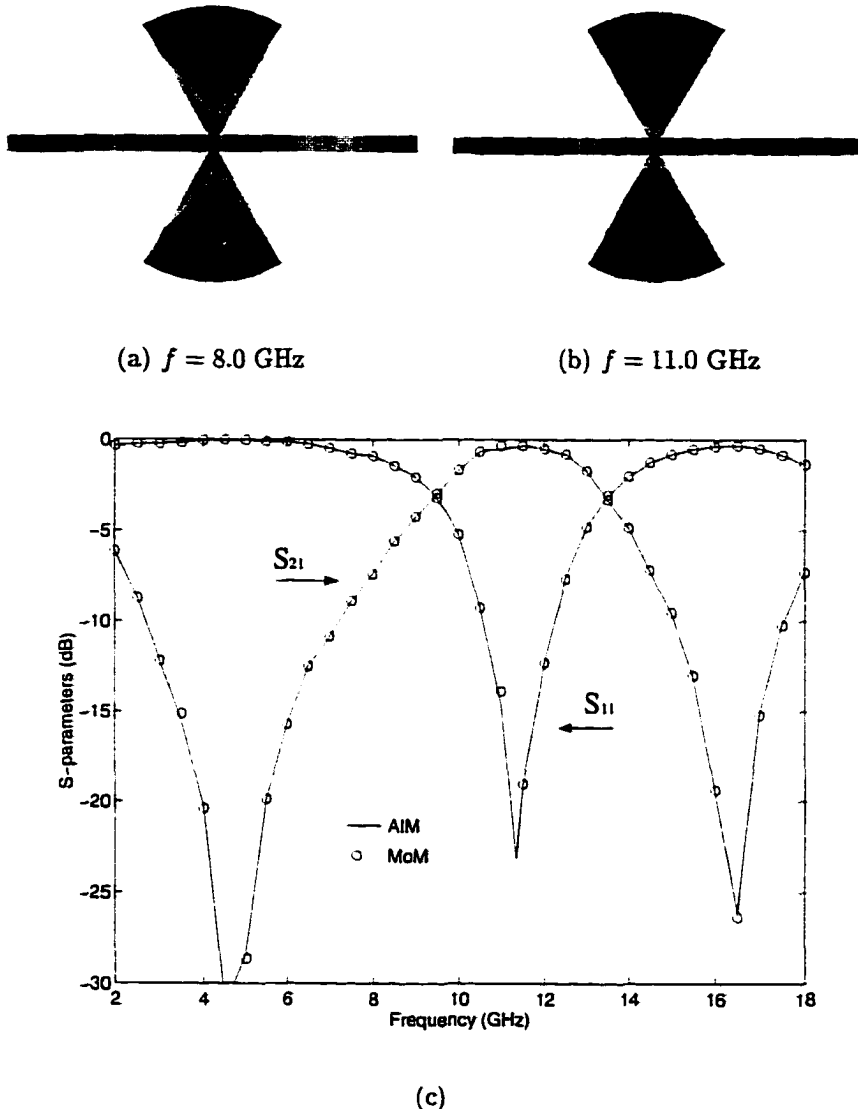
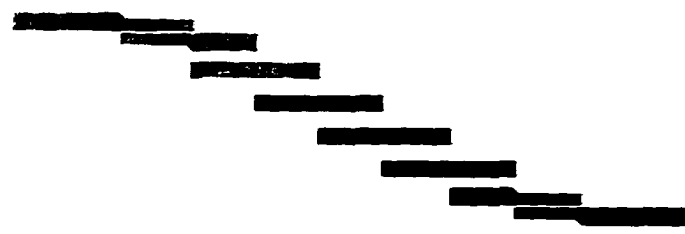
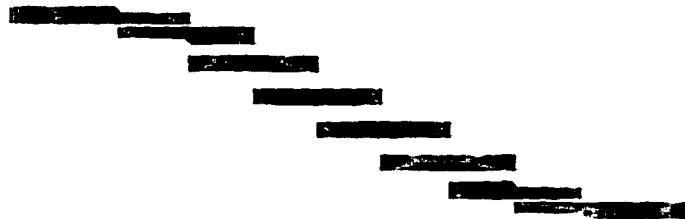


Figure 5.4 Current distributions and S-parameters for the radial stub. $\epsilon_r = 10.0$, $h = 0.635$ mm, width = 0.6 mm, radius = 5.0 mm, and angle = 60° . (a) Current distribution at $f = 8.0$ GHz. (b) Current distribution at $f = 11.0$ GHz. (c) S-parameters.

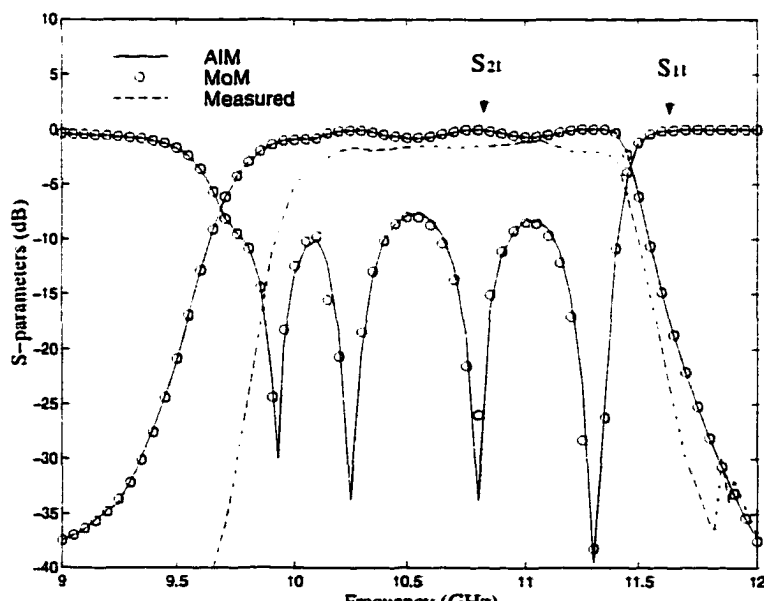
of this method, we now consider some large-scale microstrip structures. First, a structure consisting of five radial stubs is analyzed, as shown in Fig. 5.6. Each radial stub has the same dimension as in Fig. 5.4. The spacing between stubs is 7.5 mm. The numbers of facets and unknowns are 3982 and 5580, respectively. The memory requirement is 21 MB and the CPU time per iteration is 1.7 s in the AIM



(a) $f = 9.0$ GHz

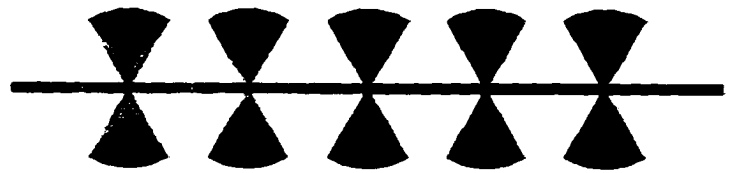


(b) $f = 11.0$ GHz

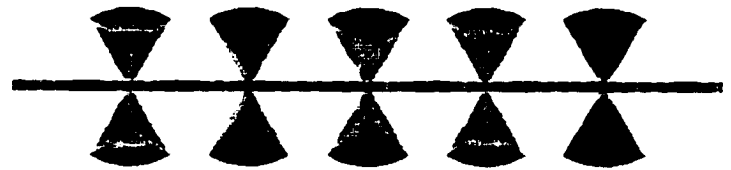


(c)

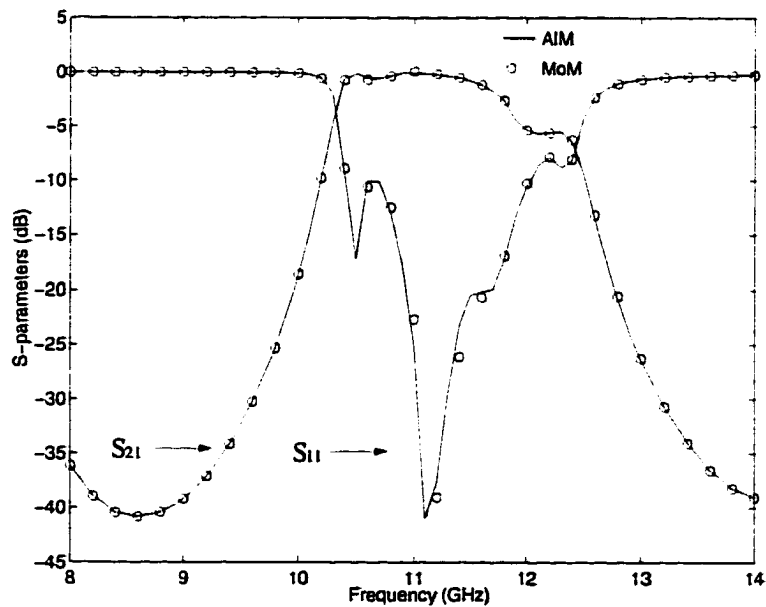
Figure 5.5 Current distributions and S-parameters for the parallel-coupled bandpass filter. $\epsilon_r = 10.0$, $h = 0.635$ mm. (a) Current distribution at $f = 9.0$ GHz. (b) Current distribution at $f = 11.0$ GHz. (c) S-parameters.



(a) $f = 9.0 \text{ GHz}$

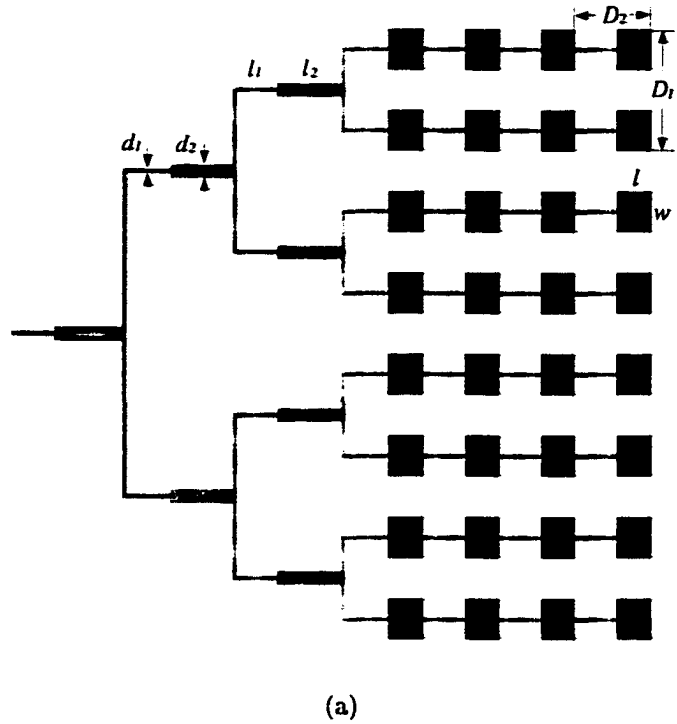


(b) $f = 11.0 \text{ GHz}$

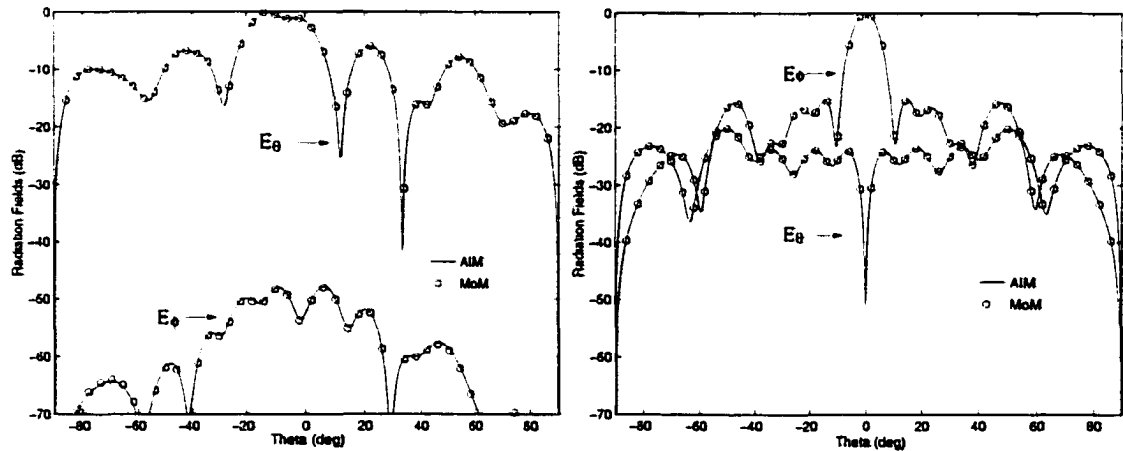


(c)

Figure 5.6 Current distributions and S-parameters for the cascaded microstrip radial stub. $\epsilon_r = 10.0$, $h = 0.635 \text{ mm}$. The spacing between stubs is 7.5 mm. (a) Current distribution at $f = 9.0 \text{ GHz}$. (b) Current distribution at $f = 11.0 \text{ GHz}$. (c) S-parameters.



(a)



(b) $\phi = 0^\circ$

(c) $\phi = 90^\circ$

Figure 5.7 Current distribution and radiation patterns of the corporate-fed microstrip antenna array. $\epsilon_r = 2.2$, $h = 1.59$ mm, $l = 10.08$ mm, $w = 11.79$ mm, $d_1 = 1.3$ mm, $d_2 = 3.93$ mm, $l_1 = 12.32$ mm, $l_2 = 18.48$ mm, $D_1 = 23.58$ mm, $D_2 = 22.40$ mm. (a) Current distribution at $f = 9.42$ GHz. (b) $\phi = 0^\circ$. (c) $\phi = 90^\circ$.

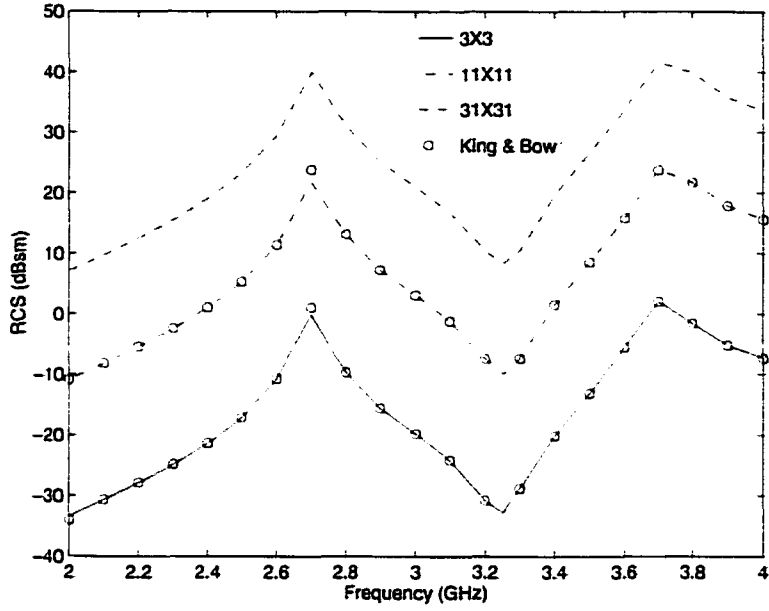


Figure 5.8 Backscatter RCS ($\sigma_{\theta\theta}$) for microstrip antenna arrays with various sizes as a function of frequency.

algorithm. In contrast, the conventional MoM requires 250 MB memory and 5.7 s CPU time per iteration. The CPU time for the matrix fill is only 40% of that in the conventional MoM. The S -parameters of this structure are shown in Fig. 5.6. The current distributions at two frequencies, $f = 8.0$ GHz and $f = 12.0$ GHz, are also given in the figure.

Next, a corporate-fed microstrip antenna array is considered, which involves 6569 facets and 8668 edges. For the conventional MoM, the memory requirement is over 600 MB and the CPU time per iteration is 15.8 s. However, it takes only 22.7 MB and 3.5 s for AIM, where FFT has the dimension of 128×128 . The AIM also yields an over 70% reduction in the CPU time for the matrix fill comparing to the conventional MoM. At the frequency $f = 9.42$ GHz, the current distribution is shown in Fig. 6. The radiation patterns in the two principal planes $\phi = 0^\circ$ and $\phi = 90^\circ$ are given in Fig. 5.7, which shows excellent agreement between the two solutions.

The third problem concerns the scattering properties of a microstrip antenna array. The substrate has relative permittivity $\epsilon_r = 2.17$ and thickness $h = 1.58$ mm. The rectangular element has length 36.6 mm and width 26.0 mm. The element spacing is 55.517 mm in both axes. The incident wave is θ -polarized with incident angles $\theta = 0^\circ$ and $\phi = 45^\circ$. The monostatic RCS (θ -component) of various size arrays

is given by Fig. 5.8 as a function of frequency, which exhibits good agreement with those data available in [25]. The 31×31 array has 141,267 unknowns. The standard MoM requires about 160 GB memory, which is far beyond the capability of most currently available computers. This method requires only 402 MB memory. The CPU time per iteration is 35.8 s.

5.5 Conclusion

In this chapter, the AIM is presented to solve large-scale microstrip antenna and circuit problems. This method accelerates the computation of the matrix-by-vector product by using FFT while still employing the triangular basis functions to model the arbitrarily shaped geometry. Compared with the conventional iterative solvers, this method is much less demanding of computer resources, the CPU time per iteration is of $O(N \log N)$ and the memory requirement is of $O(N)$.

CHAPTER 6

MULTILEVEL FAST MULTIPOLE ALGORITHM

6.1 Introduction

As mentioned in Chapter 5, another fast algorithm to speed up the matrix-vector multiplication is the fast multipole method (FMM), which is originally proposed to evaluate particle simulations [110] and later extended to solve electromagnetic problems [111]–[115]. Some successful examples using this technique include Fastcap [111], which applies the fast multipole method (FMM) to extract capacitance for objects in homogeneous media, and FISC (Fast Illinois Solver Code) [115], which uses the multilevel fast multipole algorithm (MLFMA) to deal with free-space scattering problems. After successfully being applied to homogeneous problems, this method has been investigated and extended to microstrip problem. One approach is to combine the FMM with the DCIM [117]–[119]. In [117] and [118], the equivalent problem is set up by adding N_c images at the corresponding complex coordinates, and therefore represented by $N(N_c+1)$ basis functions. In the FMM implementation, the translation is different for different images. Also, the static problem and the 2-D problem are treated in [117] and [118], respectively. In [119], both the 2-D and 3-D FMMs are employed because the surface-wave poles are extracted in the DCIM, which makes the implementation complicated. The multilevel algorithm is not implemented in those analyses. The other FMM approach is to express the Green’s function in terms of a rapidly converging steepest descent integral, and evaluate the Hankel function arising in the integrand by the FMM [120]. This approach is good for thin-stratified media.

In this chapter, the MLFMA combined with the DCIM is presented for efficient analysis of microstrip structures. Instead of being treated separately, the image sources are grouped with the original source. By the use of the multilevel algorithm, the complexity is reduced to $O(N \log N)$. The algorithm requires little extra computation compared with that applied to free space problems. Numerical results for microstrip antennas are presented to demonstrate the efficiency and accuracy of this method.

6.2 FMM Formulation

In general, both G_{xx}^A and G^Φ can be expressed in a closed form by using the DCIM

$$G(\mathbf{r}, \mathbf{r}') = \sum_{p=0}^{N_c} a_p \frac{e^{-jkr_p}}{4\pi r_p}, \quad r_p = |\mathbf{r} - (\mathbf{r}' + \hat{z}b_p)| \quad (6.1)$$

where a_p and b_p are the complex coefficients obtained from the DCIM.

To use the FMM, the entire structure is divided into groups denoted by G_m ($m = 1, 2, \dots, M$). Letting \mathbf{r}_i be the field point in group G_m centered at \mathbf{r}_m , and \mathbf{r}_j be the source point in group $G_{m'}$ centered at $\mathbf{r}_{m'}$, we have

$$\begin{aligned} \mathbf{r}_{ij} &= \mathbf{r}_i - (\mathbf{r}_j + \hat{z}b_p) \\ &= (\mathbf{r}_i - \mathbf{r}_m) + (\mathbf{r}_m - \mathbf{r}_{m'}) + (\mathbf{r}_{m'} - \mathbf{r}_j) - \hat{z}b_p \\ &= \mathbf{r}_{im} + \mathbf{r}_{mm'} - \mathbf{r}_{jm'} - \hat{z}b_p \end{aligned} \quad (6.2)$$

Employing the addition theorem and the elementary identity, we can rewrite the Green's function in (6.1) as

$$G(\mathbf{r}_i, \mathbf{r}_j) \approx \frac{k}{j16\pi^2} \iint \sum_{p=0}^{N_c} a_p e^{jk \cdot \hat{z}b_p} e^{-jk \cdot (\mathbf{r}_{im} + \mathbf{r}_{mm'} - \mathbf{r}_{jm'})} T(\hat{r}_{mm'} \cdot \hat{k}) d^2 \hat{k} \quad (6.3)$$

where

$$T(\hat{r}_{mm'} \cdot \hat{k}) = \sum_{l=0}^L (-j)^l (2l+1) h_l^{(2)}(kr_{mm'}) P_l(\hat{r}_{mm'} \cdot \hat{k}) \quad (6.4)$$

Substituting (6.3) into (5.1), we obtain

$$\begin{aligned} Z_{ij} &= \frac{\omega k}{16\pi^2} \left[\iint S^A(\hat{k}) \mathbf{U}_{im}(\hat{k}) \cdot T(\hat{r}_{mm'}, \hat{k}) \mathbf{U}_{jm'}^*(\hat{k}) d^2 \hat{k} \right. \\ &\quad \left. - \frac{1}{k_0^2} \iint S^\Phi(\hat{k}) V_{im}(\hat{k}) T(\hat{r}_{mm'}, \hat{k}) V_{jm'}^*(\hat{k}) \right] d^2 \hat{k} \end{aligned} \quad (6.5)$$

where

$$\mathbf{U}_{im}(\hat{k}) = \iint_{T_i} e^{-jk \cdot \mathbf{r}_{im}} \mathbf{f}_i d\mathbf{r} \quad (6.6)$$

$$V_{im}(\hat{k}) = \iint_{T_i} e^{-jk \cdot \mathbf{r}_{im}} \nabla \cdot \mathbf{f}_i d\mathbf{r} \quad (6.7)$$

$$S(\hat{k}) = \sum_{p=0}^{N_c} a_p e^{jk \cdot \hat{z}b_p} \quad (6.8)$$

When we use an iterative method to solve (3.12), the matrix-vector multiplication

performed in each iteration can be written as

$$\sum_{j=1}^N Z_{ij} I_j = \sum_{m' \in B_m} \sum_{j \in G_{m'}} Z_{ij} I_j + \frac{\omega k}{16\pi^2} \left[\iint S^A(\hat{k}) U_{im}(\hat{k}) \right. \\ \cdot \sum_{m' \notin B_m} T(\hat{r}_{mm'}, \hat{k}) \sum_{j \in G_{m'}} U_{jm'}^*(\hat{k}) I_j d^2 \hat{k} \\ \left. - \frac{1}{k_0^2} \iint S^\Phi(\hat{k}) V_{im}(\hat{k}) \sum_{m' \notin B_m} T(\hat{r}_{mm'}, \hat{k}) \sum_{j \in G_{m'}} V_{jm'}^*(\hat{k}) I_j d^2 \hat{k} \right] \quad (6.9)$$

for $i \in G_m$, where B_m denotes the neighboring groups of G_m including G_m itself. Therefore, the first term in (6.9) is the contribution from nearby groups and is calculated directly. The second term is the far interaction to be calculated by the FMM.

It has been shown that the operation count for calculating (6.9) is proportional to $O(N^{1.5})$ [113]. This complexity can be reduced to $O(N \log N)$ by using the multilevel algorithm [114].

6.3 Numerical Results

Before we apply the proposed method to realistic problems, the accuracy of this algorithm is examined. Consider a microstrip line on a substrate with relative permittivity $\epsilon_r = 2.17$ and thickness $h = 1.58$ mm. The frequency is 3.0 GHz. The line is 5 mm wide and 400 mm long. As shown in Fig. 6.1, the line is discretized into triangular elements with edge length 5 mm. We plot the values of matrix elements Z_{1j} ($j = 1, 2, \dots, 80$) obtained by using two different approaches. One approach is to use the original formulation (5.1). The other approach is to use the MLFMA, where group size d is $0.25\lambda_0$ with λ_0 being the wavelength in free space. Note that Z_{1j} ($j = 1, 2, \dots, 14$) is considered as the near interaction so it is calculated directly, and Z_{1j} ($j = 15, 16, \dots, 80$) is considered as the far interaction so it is calculated by the MLFMA. As seen from Fig. 6.1, these two approaches agree well. In this calculation, the number of modes L is chosen to be $kd + 3 \ln(\pi + kd)$.

Next, the complexity of this algorithm is evaluated. The CPU time per iteration and the memory requirement versus the number of unknowns are plotted by considering a rectangular microstrip patch on the substrate with relative permittivity $\epsilon_r = 2.17$ and thickness $h = 1.58$ mm. The frequency is 3.0 GHz. The patch is discretized with 20 unknowns per wavelength λ_0 . It is seen from Fig. 6.2 that the CPU time per iteration is scaled as $O(N \log N)$ and the memory requirement is scaled

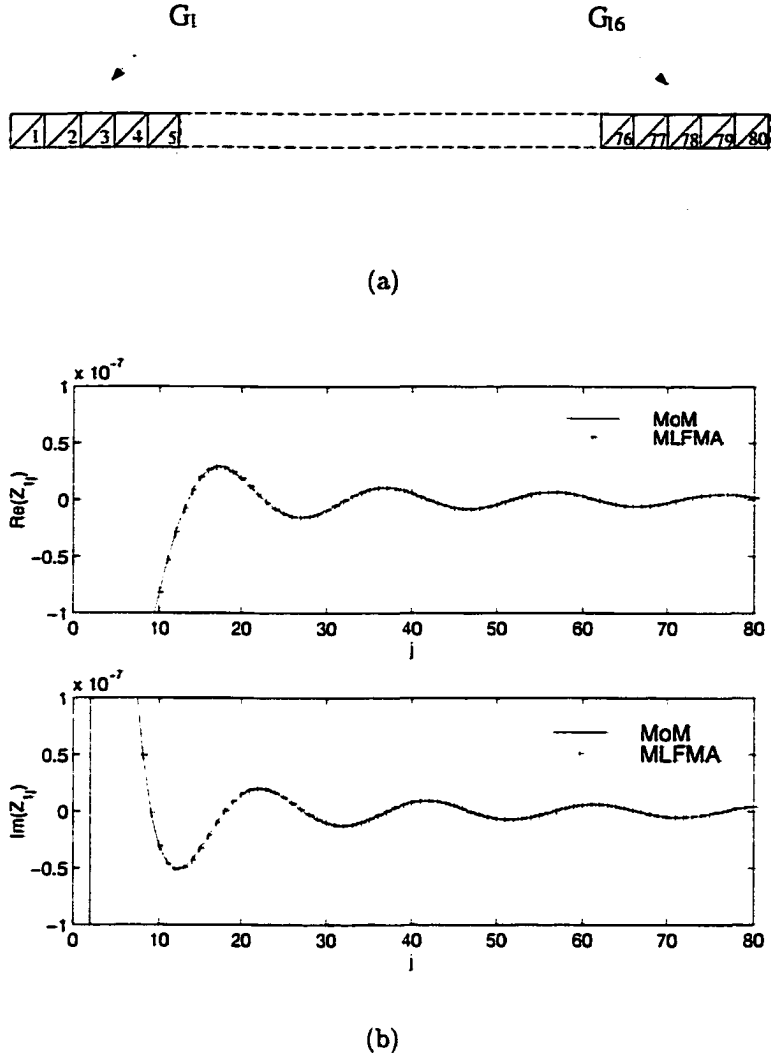


Figure 6.1 Matrix elements Z_{lj} ($j = 1, 2, \dots, 80$) calculated by the conventional MoM and the MLFMA.

as $O(N)$.

As an example, we recalculate the corporate-fed microstrip antenna array in Fig. 5.7, which involves 6569 facets and 8668 edges. At frequency $f = 9.42$ GHz, the radiation patterns in the two principal planes $\phi = 0^\circ$ and $\phi = 90^\circ$ are given in Fig. 6.3, which shows excellent agreement between this method and the conventional MoM. For the conventional MoM, the memory requirement is over 600 MB and the CPU time per iteration is 15.8 s. However, it takes only 36.3 MB and 3.0 s for the 5-level MLFMA. The MLFMA also yields more than a 70% reduction in the CPU

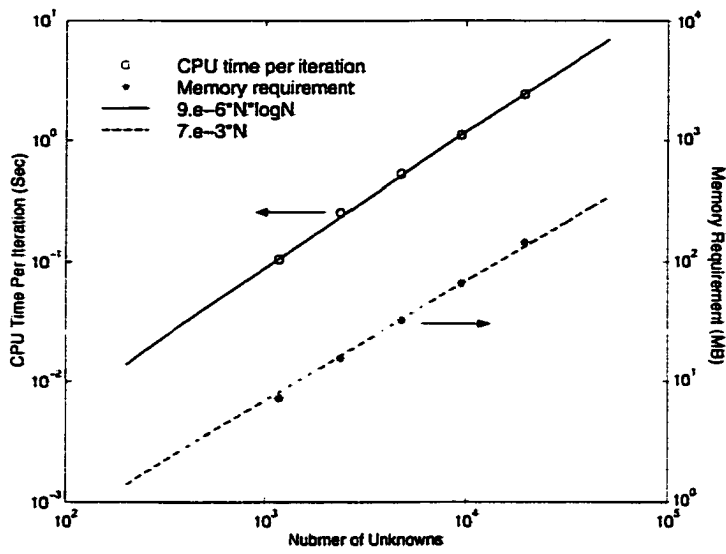


Figure 6.2 Complexity of the MLFMA. The CPU time per iteration is close to $9 \times 10^{-6} N \log N$ and the memory requirement is close to $7 \times 10^{-3} N$.

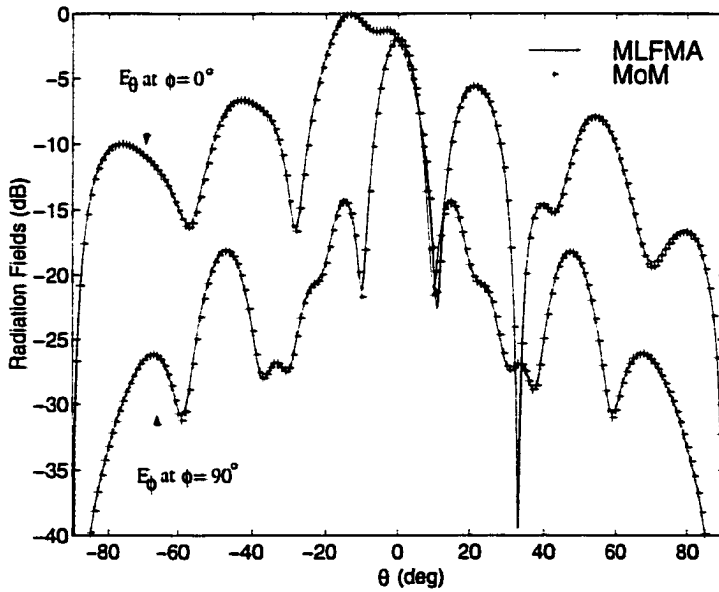


Figure 6.3 Radiation patterns of the corporate-fed microstrip antenna array. $\epsilon_r = 2.2$, $h = 1.59$ mm, $l = 10.08$ mm, $w = 11.79$ mm, $d_1 = 1.3$ mm, $d_2 = 3.93$ mm, $l_1 = 12.32$ mm, $l_2 = 18.48$ mm, $D_1 = 23.58$ mm, $D_2 = 22.40$ mm. $f = 9.42$ GHz.

time for the matrix fill comparing to the conventional MoM.

6.4 Conclusion

In this chapter, a fast algorithm to deal with large-scale microstrip problems is presented. The MLFMA originally developed for free space problems is extended to microstrip problem with the aid of the DCIM. The complexity of this algorithm is scaled as $O(N \log N)$. The efficiency and accuracy of this method are demonstrated by the numerical results.

CHAPTER 7

SUMMARY AND FUTURE WORK

A fast integral equation solver for microstrip structures in multilayer media is presented. In this method, the spectral domain Green's functions are derived from the simple transmission line perspective. The time-consuming numerical integration of the associated SIs is circumvented by applying the DCIM. Furthermore, the interpolation strategy is employed to evaluate the Green's functions, which makes the Green's function calculation in the MoM analysis very efficient. The higher-order interpolatory basis functions defined on the curvilinear triangular elements are employed, which offers a better convergence rate and gives an accurate solution with a rather coarse discretization.

To achieve the fast frequency sweep, a reduced-order model is incorporated into this MoM analysis, in which AWE is employed to obtain the Padé approximant at the expansion point. Then, the frequency response near the expansion point can be easily obtained. When one expansion point is not adequate, a binary search algorithm is employed to automatically determine the expansion points and obtain the accurate solution over the entire broadband. The numerical results show that the method using AWE results in 8 to 22 times faster than the direct calculation.

To simulate large-scale problems, two fast algorithms have been developed for planar structures in multilayer media. One is the FFT-accelerated scheme, AIM. The other is the multipole-accelerated scheme, MLFMA. Both of the algorithms reduce the computational complexity to $O(N \log N)$, which allows us to solve large-scale problems.

As one might see, several techniques have been developed to tackle the multilayer microstrip antennas and circuits, which leaves a plenty of room for future studies. The following are some possible work.

- The higher-order basis functions and the AIM have shown their advantages independently. We expect that the combination of both techniques can yield more improvement.

- The AIM in the work is confined to 2-D planar structures. The structures with vertical supporting can also be solved. Because most of the unknowns are on the planar surfaces, the matrix-vector multiplication associated with the vertical currents can be directly performed. The algorithm will maintain the computational complexity as $O(N \log N)$.

REFERENCES

- [1] K. S. Yee, "Numerical solution of initial boundary value problems in involving Maxwell's equations in isotropic media," *IEEE Trans. Antennas Propagat.*, vol. 14, pp. 302-307, May 1966.
- [2] X. Zhang and K. K. Mei, "Time-domain finite difference approach to the calculation of frequency-dependent characteristics of microstrip discontinuities," *IEEE Trans. Microwave Theory Tech.*, vol. 36, pp. 1775-1787, Dec. 1988.
- [3] D. M. Sheen, S. M. Ali, M. D. Abouzahra, and J. A. Kong, "Application of the three-dimensional finite-difference time-domain method to the analysis of planar microstrip circuits," *IEEE Trans. Microwave Theory Tech.*, vol. 38, pp. 849-857, July 1990.
- [4] I. Wolff, "Finite difference time-domain simulation of electromagnetic fields and microwave circuits," *Int. J. Numerical Modelling: Electron Networks, Devices and Fields*, vol. 5, pp. 163-182, 1992.
- [5] M. Gribbons, A. C. Cangellaris, and J. L. Prince, "Finite-difference time-domain analysis of pulse propagation in multichip module interconnects," *IEEE Trans. Compon. Hybr. and Manuf. Technol.*, vol. 16, pp. 490-497, Aug. 1993.
- [6] M. Piket-May, A. Taflove, and J. Baron, "FD-TD modeling of digital signal propagation in 3-D circuits with passive and active loads," *IEEE Trans. Microwave Theory Tech.*, vol. 42, pp. 1514-1523, Aug. 1994.
- [7] H. H. M. Ghous and E.B. EL-Sharawy, "An accurate equivalent circuit model of flip chip and via interconnects," *IEEE Trans. Microwave Theory Tech.*, vol. 44, pp. 2543-2553, Dec. 1996.
- [8] M. Fujii and W. J. R. Hoefer, "A three-dimensional Harr-wavelet-based multiresolution analysis similar to the FDTD method—Derivation and application," *IEEE Trans. Microwave Theory Tech.*, vol. 46, pp. 2463-2475, Dec. 1998.
- [9] J. M. Jin, *The Finite Element Method in Electromagnetics*. New York: Wiley, 1993.

- [10] J. S. Wang and R. Mittra, "Finite element analysis of MMIC structures and electronic packages using absorbing boundary conditions," *IEEE Trans. Microwave Theory Tech.*, vol. 42, pp. 441-449, Mar. 1994.
- [11] J. G. Yook, N. I. Dib, and L. P. B. Katehi, "Characterization of high frequency interconnects using finite difference time domain and finite element methods," *IEEE Trans. Microwave Theory Tech.*, vol. 42, pp. 1727-1736, Sept. 1994.
- [12] A. C. Polycarpou, P. A. Tirkas, and C. A. Balanis, "The finite-element method for modeling circuits and interconnects for electronic packaging," *IEEE Trans. Microwave Theory Tech.*, vol. 45, pp. 1868-1874, Oct. 1997.
- [13] D. M. Pozar, "Input impedance and mutual coupling of rectangular microstrip antennas," *IEEE Trans. Antennas Propagat.*, vol. 30, pp. 1191-1196, Nov. 1982.
- [14] R. W. Jackson and D. M. Pozar, "Full wave analysis of microstrip open-end and gap discontinuities," *IEEE Trans. Microwave Theory Tech.*, vol. 33, pp. 1036-1042, Oct. 1985.
- [15] R. H. Jansen, "The spectral-domain approach for microwave integrated circuits," *IEEE Trans. Microwave Theory Tech.*, vol. 33, pp. 1043-1056, Oct. 1985.
- [16] D. M. Pozar, "Analysis of finite phased arrays of printed dipoles," *IEEE Trans. Antennas Propagat.*, vol. 33, pp. 1045-1053, Oct. 1985.
- [17] E. H. Newman and D. Forrai, "Scattering from a microstrip patch," *IEEE Trans. Antennas Propagat.*, vol. 35, pp. 245-251, Mar. 1987.
- [18] D. M. Pozar and S. M. Voda, "A rigorous analysis of a microstrip feed patch antenna," *IEEE Trans. Antennas Propagat.*, vol. 35, pp. 1343-1350, Dec. 1987.
- [19] H. Y. Yang and N. G. Alexopoulos, "Basic blocks for high frequency interconnects: Theory and experiments," *IEEE Trans. Microwave Theory Tech.*, vol. 36, pp. 1258-1264, Aug. 1988.
- [20] R. W. Jackson, "Full-wave, finite element analysis of irregular microstrip discontinuities," *IEEE Trans. Microwave Theory Tech.*, vol. 37, pp. 81-89, Jan. 1989.

- [21] M. Davidovitz and Y. T. Lo, "Rigorous analysis of a circular patch antenna excited by a microstrip transmission line," *IEEE Trans. Antennas Propagat.*, vol. 37, pp. 949-958, Aug. 1989.
- [22] S. Wu, H. Y. Yang, N. G. Alexopoulos, and I. Wolff, "A rigorous dispersive characterization of microstrip cross and T junctions," *IEEE Trans. Microwave Theory Tech.*, vol. 38, pp. 1837-1844, Dec. 1990.
- [23] J. T. Aberle, D. M. Pozar, and C. R. Birtcher, "Evaluation of input impedance and radar cross section of probe-fed microstrip patch elements using an accurate feed model," *IEEE Trans. Antennas Propagat.*, vol. 39, pp. 1691-1696, Dec. 1991.
- [24] T. S. Horng, N. G. Alexopoulos, S. C. Wu, and H. Y. Yang, "Full-wave spectral-domain analysis for open microstrip discontinuities of arbitrary shape including radiation and surface-wave losses," *Int. J. Microwave Millimeter-Wave Comput. Aided Engg.*, vol. 2, pp. 224-240, 1992.
- [25] A. S. King and W. J. Bow, "Scattering from a finite array of microstrip patches," *IEEE Trans. Antennas Propagat.*, vol. 40, pp. 770-774, July 1992.
- [26] L. P. Dunleavy and P. B. Katehi, "A generalized method for analyzing shielded thin microstrip discontinuities," *IEEE Trans. Microwave Theory Tech.*, vol. 36, pp. 1758-1766, Dec. 1988.
- [27] W. Schwab and W. Menzel, "On the design of planar microwave components using multilayer structures," *IEEE Trans. Microwave Theory Tech.*, vol. 40, pp. 67-72, Jan. 1992.
- [28] J. C. Rautio and R. F. Harrington, "An electromagnetic time-harmonic analysis of shielded microstrip circuits," *IEEE Trans. Microwave Theory Tech.*, vol. 35, pp. 726-730, Aug. 1987.
- [29] W. Wertgen and R. H. Jansen, "Efficient direct and iterative electrodynamic analysis of geometrically complex MIC and MMIC structures," *Int. J. Numerical Modelling: Electron Networks, Devices and Fields*, vol. 2, pp. 153-186, 1989.
- [30] A. Hill and V. K. Tripathi, "An efficient algorithm for the three-dimensional analysis of passive microstrip components and discontinuities for microwave and

millimeter-wave integrated circuits," *IEEE Trans. Microwave Theory Tech.*, vol. 39, pp. 83-91, Jan. 1991.

- [31] C. J. Railton and S. A. Meade, "Fast rigorous analysis of shielded planar filters," *IEEE Trans. Microwave Theory Tech.*, vol. 40, pp. 978-985, May 1992.
- [32] G. V. Eleftheriades, J. R. Mosig, and M. Guglielmi, "A fast integral equation techniques for shielded planar circuits defined on nonuniform meshes," *IEEE Trans. Microwave Theory Tech.*, vol. 44, pp. 2293-2296, Dec. 1996.
- [33] B. Houshamnd, W. C. Chew, and S. W. Lee, "Fourier transform of a linear distribution with triangular support and its applications in electromagnetics," *IEEE Trans. Antennas Propagat.*, vol. 39, pp. 252-254, Feb. 1991.
- [34] T. Itoh and R. Mittra, "Spectral-domain approach for calculating dispersion characteristics of microstrip lines," *IEEE Trans. Microwave Theory Tech.*, vol. 21, pp. 496-498, 1973.
- [35] T. Itoh, "Spectral domain immitance approach for dispersion characteristics of generalized printed transmission lines," *IEEE Trans. Microwave Theory Tech.*, vol. 28, pp. 733-736, July 1980.
- [36] D. M. Pozar, "Improved computational efficiency for the method of moments solution of printed dipoles and patch," *Electromagn.*, vol. 3, pp. 299-309, 1983.
- [37] P. B. Katehi and N. G. Alexopoulos, "On the modeling of electromagnetically coupled microstrip antennas —The printed strip dipole," *IEEE Trans. Antennas Propagat.*, vol. 32, pp. 1179-1186, Nov. 1984.
- [38] J. R. Mosig, "Arbitrarily shaped microstrip structures and their analysis with a mixed potential integral equation," *IEEE Trans. Microwave Theory Tech.*, vol. 36, pp. 314-323, Feb. 1988.
- [39] J. R. Mosig, "Integral equation techniques," in *Numerical Techniques for Microwave and Millimeter-Wave Passive Structures*. Edited by T. Itoh. New York: Wiley, 1988.
- [40] W. P. Harokopus and P. B. Katehi, "Characterization of microstrip discontinuities on multilayer dielectric substrates including radiation losses," *IEEE Trans. Microwave Theory Tech.*, vol. 37, pp. 2058-2066, Dec. 1989.

- [41] K. L. Wu, J. Litva, R. Fralich, and C. Wu, "Full-wave analysis of arbitrarily shaped line-fed microstrip antennas using triangular finite-element method," *IEE Proc.-H*, vol. 138, pp. 421-428, Oct. 1991.
- [42] D. I. Wu, D. C. Chang, and B. L. Brim, "Accurate numerical modeling of microstrip junctions and discontinuities," *Int. J. Microwave Millimeter-Wave Comput. Aided Engg.*, vol. 1, pp. 48-58, 1991.
- [43] K. A. Michalski and D. Zheng, "Analysis of microstrip resonators of arbitrary shape," *IEEE Trans. Microwave Theory Tech.*, vol. 40, pp. 112-119, Jan. 1992.
- [44] D. C. Chang and J. X. Zhang, "Electromagnetic modeling of passive circuit elements in MMIC," *IEEE Trans. Microwave Theory Tech.*, vol. 40, pp. 1741-1747, Sept. 1992.
- [45] F. Alonso-Monferrer, A. A. Kishk, and A. W. Glisson, "Green's functions analysis of planar circuits in a two-layer grounded medium," *IEEE Trans. Antennas Propagat.*, vol. 40, pp. 690-696, June 1992.
- [46] R. A. Kipp, C. H. Chan, A. T. Yang, and J. T. Yao, "Simulation of high-frequency integrated circuits incorporating full-wave analysis of microstrip discontinuities," *IEEE Trans. Microwave Theory Tech.*, vol. 41, pp. 848-854, May 1993.
- [47] R. A. Kipp and C. H. Chan, "Triangular-domain basis functions for full-wave analysis of microstrip discontinuities," *IEEE Trans. Microwave Theory Tech.*, vol. 41, pp. 1187-1194, June/July 1993.
- [48] R. Gillard, J. Corre, M. Drissi and J. Citerne, "A general treatment of matched terminations using integral equations-modeling and application," *IEEE Trans. Microwave Theory Tech.*, vol. 42, pp. 2545-2553, Dec. 1994.
- [49] E. K. L. Yeung, J. C. Beal, and Y. M. M. Antar, "Multilayer microstrip structure analysis with matched load simulation," *IEEE Trans. Microwave Theory Tech.*, vol. 43, pp. 143-149, Jan. 1995.
- [50] M. J. Tsai, F. D. Flaviis, O. Fordham, and N. G. Alexopoulos, "Modeling planar arbitrarily shaped microstrip elements in multilayered media," *IEEE Trans. Microwave Theory Tech.*, vol. 45, pp. 330-337, Mar. 1997.

- [51] F. Ling and J. M. Jin, "Scattering and radiation analysis of microstrip antennas using discrete complex image method and reciprocity theorem," *Microwave Opt. Tech. Lett.*, vol. 16, pp. 212-216, Nov. 1997.
- [52] Q.-H. Liu and W. C. Chew, "Applications of the conjugate gradient fast Fourier Hankel transfer method with an improved fast Hankel transform algorithm," *Radio Science*, vol. 29, pp. 1009-1022, July-August 1994.
- [53] J. Zhao, S. Kapur, D. E. Long, and W. W.-M. Dai, "Efficient three-dimensional extraction based on static and full-wave layered Green's functions," *Proceedings of the 35th Design Automation Conference*, June 1998.
- [54] R. C. Hsieh and J. T. Kuo, "Fast full-wave analysis of planar microstrip circuit elements in stratified media," *IEEE Trans. Microwave Theory Tech.*, vol. 46, pp. 1291-1297, Sept. 1998.
- [55] T. J. Cui and W. C. Chew, "Fast evaluation of Sommerfeld integrals for EM scattering and radiation by three-dimensional buried objects," *IEEE Geosci. Remote Sensing*, vol. 37, pp. 887-900, Mar. 1999.
- [56] W. Cai and T. Yu, "Fast calculations of Dyadic Green's functions for electromagnetic scattering in a multilayer medium," submitted to *J. Comput. Phys.*, Nov. 1999.
- [57] D. G. Fang, J. J. Yang, and G. Y. Delisle, "Discrete image theory for horizontal electric dipole in a multilayer medium," *IEE Proc.-H*, vol. 135, pp. 297-303, Oct. 1988.
- [58] Y. L. Chow, J. J. Yang, D. G. Fang, and G. E. Howard, "A closed-form spatial Green's function for the thick microstrip substrate," *IEEE Trans. Microwave Theory Tech.*, vol. 39, pp. 588-592, Mar. 1991.
- [59] J. J. Yang, Y. L. Chow, G. E. Howard and D. G. Fang, "Complex images of an electric dipole in homogeneous and layered dielectrics between two ground planes," *IEEE Trans. Microwave Theory Tech.*, vol. 40, pp. 595-600, Mar. 1992.
- [60] R. A. Kipp and C. H. Chan, "Complex image method for sources in bounded regions of multilayer structures," *IEEE Trans. Microwave Theory Tech.*, vol. 42, pp. 860-865, May 1994.

- [61] G. Dural and M. I. Aksun, "Closed-form Green's functions for general sources and stratified media," *IEEE Trans. Microwave Theory Tech.*, vol. 43, pp. 1545-1552, July 1995.
- [62] M. I. Aksun, "A robust approach for the derivation of closed-form Green's functions," *IEEE Trans. Microwave Theory Tech.*, vol. 44, pp. 651-658, May 1996.
- [63] C. H. Chan and R. A. Kipp, "Application of the complex image method to multilevel, multiconductor microstrip lines," *Int. J. Microwave Millimeter-Wave Comput. Aided Engg.*, vol. 7, pp. 359-367, 1997.
- [64] C. H. Chan and R. A. Kipp, "Application of the complex image method to characterization of microstrip vias," *Int. J. Microwave Millimeter-Wave Comput. Aided Engg.*, vol. 7, pp. 368-379, 1997.
- [65] N. Hojjat, S. Safavi-Naeini, R. Faraji-Dana, and Y. L. Chow, "Fast computation of the nonsymmetrical components of the Green's function for multilayer media using complex images," *IEE Proc.-H*, vol. 145, pp. 285-288, Aug. 1998.
- [66] F. Ling, D. Jiao, and J. M. Jin, "Efficient electromagnetic modeling of microstrip structures in multilayer media," *IEEE Trans. Microwave Theory Tech.*, vol. 47, pp. 1810-1818, Sept. 1999.
- [67] Y. Hua and T. K. Sarkar, "Generalized pencil-of-function method for extracting poles of an EM system from its transient response," *IEEE Trans. Antennas Propagat.*, vol. 37, pp. 229-234, Feb. 1989.
- [68] W. C. Chew, *Waves and Fields in Inhomogeneous Media*. Piscataway: IEEE Press, 1995.
- [69] K. A. Michalski, "On the scalar potential of a point charge associated with a time-harmonic dipole in a layered medium," *IEEE Trans. Antennas Propagat.*, vol. 35, pp. 1299-1301, Nov. 1987.
- [70] K. A. Michalski and D. Zheng, "Electromagnetic scattering and radiation by surfaces of arbitrary shape in layered media, Part I: Theory," *IEEE Trans. Antennas Propagat.*, vol. 38, pp. 335-344, Mar. 1990.

- [71] K. A. Michalski and J. R. Mosig, "Multilayered media Green's functions in integral equation formulations," *IEEE Trans. Antennas Propagat.*, vol. 45, pp. 508-519, Mar. 1997.
- [72] Y. L. Chow, N. Hojjat, S. Safavi-Naeini, and R. Faraji-Dana, "Spectral Green's functions for multilayer media in a convenient computational form," *IEE Proc.-H*, vol. 145, pp. 85-91, Feb. 1998.
- [73] S. M. Rao, D. R. Wilton, and A. W. Glisson, "Electromagnetic scattering by surface of arbitrary shape," *IEEE Trans. Antennas Propagat.*, vol. 30, pp. 409-418, May 1982.
- [74] J. C. Nedelec, "Mixed finite elements in R^3 ," *Numer. Mathem.*, vol. 35, pp. 315-341, 1980.
- [75] R. D. Graglia, D. R. Wilton, and A. F. Peterson, "Higher order interpolatory vector bases for computational electromagnetics," *IEEE Trans. Antennas Propagat.*, vol. 45, pp. 329-342, March 1997.
- [76] J. P. Webb, "Hierarchical vector basis functions of arbitrary order for triangular and tetrahedral finite element," *IEEE Trans. Antennas Propagat.*, vol. 47, pp. 1244-1253, Aug. 1999.
- [77] M. G. Duffy, "Quadrature over a pyramid or cube of integrands with a singularity at a vertex," *J. Numer. Anal.*, vol. 19, pp. 1260-1262, Dec. 1982.
- [78] J. C. Rautio, "A de-embedding algorithm for electromagnetics", *Int. J. Microwave Millimeter-Wave Comput. Aided Engg.*, vol. 11, pp. 282-287, 1991.
- [79] O. Fordham, M. J. Tsai, and N. G. Alexopoulos, "Electromagnetic synthesis of overlap-gap-coupled microstrip filters," *IEEE MTT-S Int. Microwave Sym.*, pp. 1199-1202, 1995.
- [80] W. H. Press, S. A. Teukolsky, W. T. Vetterling, and B. P. Flannery, *Numerical Recipes in Fortran*. Cambridge: University Press, 1992.
- [81] H. Contopanagos, L. Zhang, and N. G. Alexopoulos, "Thin frequency-selective lattices integrated in novel compact MIC, MMIC, and PCA architectures," *IEEE Trans. Microwave Theory Tech.*, vol. 46, pp. 1936-1948, Nov. 1998.

- [82] F. Tefiku and E. Yamashita, "Improved analysis method for multiport microstrip annular-ring power divider," *IEEE Trans. Microwave Theory Tech.*, vol. 42, pp. 376-381, Mar. 1994.
- [83] F. Giannini, R. Sorrentino, and J. Vrba, "Planar circuit analysis of microstrip radial stub," *IEEE Trans. Microwave Theory Tech.*, vol. 32, pp. 1652-1655, Dec. 1984.
- [84] T. Edwards, *Foundations for Microstrip Circuit Design*. Chichester, UK: Wiley, 1991.
- [85] L. T. Pillage and R. A. Rohrer, "Asymptotic waveform evaluation for timing analysis," *IEEE Trans. Computer-Aided Design*, vol. 9, pp. 352-366, Apr. 1990.
- [86] E. Chiprout and M. S. Nakhla, "Analysis of interconnect networks using complex frequency hopping," *IEEE Trans. Computer-Aided Design*, vol. 14, pp. 186-200, Feb. 1995.
- [87] P. Feldmann and R. W. Freund, "Efficient linear circuit analysis by Padé approximation via the Lanczos process," *IEEE Trans. Computer-Aided Design*, vol. 14, pp. 639-649, May 1995.
- [88] M. Celik and A. C. Cangellaris, "Simulation of dispersive multiconductor transmission lines by Padé approximation via the Lanczos process," *IEEE Trans. Microwave Theory Tech.*, vol. 44, pp. 2525-2535, Dec. 1996.
- [89] M. A. Kolbehdari, M. Srinivasan, M. S. Nakhla, Q. J. Zhang, and R. Achar, "Simultaneous time and frequency domain solutions of EM problems using finite element and CFH techniques," *IEEE Trans. Microwave Theory Tech.*, vol. 44, pp. 1526-1534, Sept. 1996.
- [90] J. P. Zhang and J. M. Jin, "Preliminary study of AWE method for FEM analysis of scattering problems," *Microwave Opt. Tech. Lett.*, vol. 17, pp. 7-12, Jan. 1998.
- [91] C. J. Reddy, M. D. Deshpande, C. R. Cockrell, and F. B. Beck, "Fast RCS computation over a frequency band using method of moments in conjunction with asymptotic waveform evaluation technique," *IEEE Trans. Antennas Propagat.*, vol. 46, pp. 1229-1233, Aug. 1998.

- [92] J. E. Bracken, D. K. Sun, and Z. J. Cendes, "S-domain methods for simultaneous time and frequency characterization of electromagnetic devices," *IEEE Trans. Microwave Theory Tech.*, vol. 46, pp. 1277-1290, Sept. 1998.
- [93] G. J. Burke, E. K. Miller, S. Chakrabarti, and K. Demarest, "Using model-based parameter estimation to increase the efficiency of computing electromagnetic transfer functions," *IEEE Trans. Magn.*, vol. 25, pp. 2807-2809, July 1989.
- [94] J. E. Pekarek and T. Itoh, "Use of frequency derivatives in the three-dimensional full-wave spectral domain technique," *IEEE Trans. Microwave Theory Tech.*, vol. 44, pp. 2466-2472, Dec. 1996.
- [95] N. N. Bojarski, "*k*-space formulation of the electromagnetic scattering problem," Air Force Avionics Lab. Technical Report AFAL-TR-71-75, Mar. 1971.
- [96] T. K. Sarkar, E. Arvas, and S. M. Rao, "Application of FFT and the conjugate gradient method for the solution of electromagnetic radiation from electrically large and small conducting bodies," *IEEE Trans. Antennas Propagat.*, vol. 34, pp. 635-640, May 1986.
- [97] T. J. Peters and J. L. Volakis, "Application of a conjugate gradient FFT method to scattering from thin planar material plates," *IEEE Trans. Antennas Propagat.*, vol. 36, pp. 518-526, Apr. 1988.
- [98] M. F. Catedra, J. G. Cuevas, and L. Nuno, "A scheme to analyze conducting plates of resonant size using the conjugate gradient method and the fast Fourier transform," *IEEE Trans. Antennas Propagat.*, vol. 36, pp. 1744-1752, Dec. 1988.
- [99] M. F. Catedra and E. Gago, "Spectral domain analysis of conducting patches of arbitrary geometry in multilayer media using the CG-FFT method," *IEEE Trans. Antennas Propagat.*, vol. 38, pp. 1530-1536, Oct. 1990.
- [100] A. P. M. Zwamborn and P. M. van den Berg, "A weak form of the conjugate gradient FFT method for plate problems," *IEEE Trans. Antennas Propagat.*, vol. 39, pp. 224-228, Feb. 1991.
- [101] J. M. Jin and J. L. Volakis, "A biconjugate gradient solution for scattering by planar plates," *Electromagn.*, vol. 12, pp. 105-119, 1992.

- [102] Y. Zhuang, K. Wu, C. Wu, and J. Litva, "A combined full-wave CG-FFT method for rigorous analysis of large microstrip antenna array," *IEEE Trans. Antennas Propagat.*, vol. 44, pp. 102-109, Jan. 1996.
- [103] C. F. Wang, F. Ling, and J. M. Jin, "A fast full-wave analysis of scattering and radiation from large finite arrays of microstrip antennas" *IEEE Trans. Antennas Propagat.*, vol. 46, Oct. 1998.
- [104] E. Bleszynski, M. Bleszynski, and T. Jaroszewicz, "A fast integral-equation solver for electromagnetic scattering problem," *IEEE APS Int. Symp. Dig.*, pp. 416-419, 1994.
- [105] E. Bleszynski, M. Bleszynski, and T. Jaroszewicz, "AIM: Adaptive integral method for solving large-scale electromagnetic scattering and radiation problems," *Radio Science*, vol. 31, pp. 1225-1251, Sept.-Oct. 1996.
- [106] F. Ling, C. F. Wang, and J. M. Jin, "Application of adaptive integral method to scattering and radiation analysis of arbitrarily shaped planar structures," *J. Electromagn. Waves Appl.*, vol. 12, pp. 1021-1038, Aug. 1998.
- [107] F. Ling, C. F. Wang, and J. M. Jin, "An efficient algorithm for analyzing large-scale microstrip structures using adaptive integral method combined with discrete complex image method," *IEEE Trans. Microwave Theory Tech.*, accepted for publication.
- [108] C. H. Chan, C. M. Lin, L. Tsang, and Y. F. Leung, "A sparse-matrix / canonical grid method for analyzing microstrip structures," *IEICE Trans. Electron.*, vol. E80-C, pp. 1354-1359, Nov. 1997.
- [109] J. R. Phillips and J. K. White, "A precorrected-FFT method for electrostatic analysis of complicated 3-D structures," *IEEE Trans. Computer-Aided Design*, vol. 16, pp. 1059-1072, Oct. 1997.
- [110] V. Rokhlin, "Rapid solution of integral equations of scattering theory in two dimensions," *J. Comput. Phys.*, vol. 86, pp. 414-439, Feb. 1990.
- [111] K. Nabors and J. White, "Fastcap: A multipole-accelerated 3-D capacitance extraction program," *IEEE Trans. Computer-Aided Design*, vol. 10, pp. 1447-1459, Nov. 1991.

- [112] R. Coifman, V. Rokhlin, and S. Wandzura, "The fast multipole method for the wave equation: A pedestrian prescription," *IEEE Antennas Propagat. Mag.*, vol. 35, pp. 7-12, June 1993.
- [113] J. M. Song and W. C. Chew, "Fast multipole method solution using parametric geometry," *Microwave Opt. Tech. Lett.*, vol. 7, pp. 760-765, Nov. 1994.
- [114] J. M. Song, C. C. Lu, and W. C. Chew, "Multilevel fast multipole algorithm for electromagnetic scattering by large complex objects," *IEEE Trans. Antennas Propagat.*, vol. 45, pp. 1488-1493, Oct. 1997.
- [115] J. M. Song, C. C. Lu, W. C. Chew and S. W. Lee, "Fast Illinois Solver Code (FISC)," *IEEE Antennas Propagat. Mag.*, vol. 40, pp. 27-34, June 1998.
- [116] K. Nabors and J. White, "Multipole-accelerated capacitance extraction for 3-D structures with multilayer dielectrics," *IEEE Trans. Circ. Syst.*, vol. 39, pp. 946-954, Nov. 1992.
- [117] V. Jandhyala, E. Michielssen, and R. Mittra, "Multipole-accelerated capacitance computation for 3-D structures in a stratified dielectric medium using in a closed form Green's function," *Int. J. Microwave Millimeter-Wave Comput. Aided Engg.*, vol. 5, pp. 68-78, May 1995.
- [118] L. Gurel and M. I. Aksun, "Electromagnetic scattering solution of conducting strips in layered media using the fast multipole method," *IEEE Microwave Guided Wave Lett.*, vol. 6, pp. 277-279, Aug. 1996.
- [119] P. A. Macdonald and T. Itoh, "Fast simulation of microstrip structures using the fast multipole method," *Int. J. Numerical Modelling: Electron Networks, Devices and Fields*, vol. 9, pp. 345-357, 1996.
- [120] J. S. Zhao, W. C. Chew, C. C. Lu, E. Michielssen, and J. M. Song, "Thin-stratified medium fast-multipole algorithm for solving microstrip structures," *IEEE Trans. Microwave Theory Tech.*, vol. 46, pp. 395-403, Apr. 1998.
- [121] B. Hu, and W. C. Chew, "Fast Inhomogeneous Plane Wave Algorithm for Electromagnetic Solutions in Layered Medium Structures – 2D Case," *Radio Science*, Vol. 35, No. 1, 2000

- [122] S. Kapur and D. E. Long, "IES³: Efficient electrostatic and electromagnetic simulation," *IEEE Computational Science Engineering*, pp. 60-67, Oct.-Dec. 1998.
- [123] S. Kapur, D. E. Long, and J. Zhao, "Efficient full-wave simulation in layered, lossy media," *Proc. Custom Integrated Circuit Conference*, pp. 211-214, 1998.

VITA

Feng Ling was born in Jiangsu, China, in 1971. He received the B.S. and M.S. degrees in electrical engineering from Nanjing University of Science and Technology, Nanjing, China, in 1993 and 1996, respectively. He is currently working toward his Ph.D. degree in electrical engineering at the University of Illinois at Urbana-Champaign (UIUC).

He has been a research assistant at the Center for Computational Electromagnetics (CCEM) at UIUC since 1996. His research interests include electromagnetic modeling of multilayer microstrip circuits, antennas and interconnects, and fast algorithms for computational electromagnetics. He is a member of Phi Kappa Phi. He was the recipient of the 1999 Y. T. Lo Outstanding Research Award from the Department of Electrical and Computer Engineering at UIUC.

A listing of Feng Ling's refereed journal publications and refereed conference presentations follows.

Articles in Edited Volumes

1. F. Ling and J. M. Jin, "Hybridization of SBR and MoM for scattering by large bodies with inhomogeneous protrusions," *Progress in Electromagnetics Research*, PIER 17, pp. 25-34, 1997.

Journal Articles

1. D. G. Fang, F. Ling, and Y. Long, "Rectangular waveguide Green's function involving complex images," *Chinese Journal of Radio Science*, pp. 146-149, 1995.
2. F. Ling and D. G. Fang, "Derivation of generalized expressions of Green's functions for a multilayered medium using the spectral-domain immittance approach," *Journal of Microwaves*, vol. 12, no. 2, pp. 83-88, 1996.
3. F. Ling and D. G. Fang, "Analysis of millimeter-wave multilayered microstrip lines with spectral-domain Green's functions," *Journal of Applied Sciences*, vol. 15, pp. 265-271, Sept. 1997.

4. F. Ling and J. M. Jin, "Hybridization of SBR and MoM for scattering by large bodies with inhomogeneous protrusions—Summary," *J. Electromagn. Waves and Appl.*, vol. 11, pp. 1249-1255, 1997.
5. F. Ling and J. M. Jin, "Scattering and radiation analysis of microstrip antennas using discrete complex image method and reciprocity theorem," *Microwave Opt. Tech. Lett.*, vol. 16, no. 4, pp. 212-216, Nov. 1997.
6. C. F. Wang, F. Ling, and J. M. Jin, "A fast full-wave analysis of scattering and radiation from large finite arrays of microstrip antennas," *IEEE Trans. Antennas Propagat.*, vol. 46, Oct. 1998.
7. J. M. Jin, F. Ling, S. T. Carolan, J. M. Song, W. C. Gibson, W. C. Chew, C. C. Lu, and R. Kipp, "A hybrid SBR/MoM technique for analysis of scattering from small protrusions on a large conducting body," *IEEE Trans. Antennas Propagat.*, vol. 46, pp. 1349-1357, Sept. 1998.
8. F. Ling, C. F. Wang, and J. M. Jin, "Application of adaptive integral method to scattering and radiation analysis of arbitrarily shaped planar structures," *J. Electromagn. Waves and Appl.*, vol. 12, pp. 1021-1038, Aug. 1998.
9. F. Ling, C. F. Wang, and J. M. Jin, "An efficient algorithm for analyzing large-scale microstrip structures using adaptive integral method combined with discrete complex image method," *IEEE Trans. Microwave Theory Tech.*, accepted for publication.
10. C. F. Wang, F. Ling, J. M. Song, and J. M. Jin, "Adaptive integral solution of combined field integral equation," *Microwave Opt. Tech. Lett.*, vol. 19, no. 5, pp. 321-328, Dec. 1998.
11. F. Ling, C. F. Wang, and J. M. Jin, "A fast electromagnetic solver using adaptive integral method," *Chinese Journal of Electronics*, accepted for publication.
12. F. Ling, D. Jiao, and J. M. Jin, "Efficient electromagnetic modeling of microstrip structures in multilayer media," *IEEE Trans. Microwave Theory Tech.*, vol. 47, pp. 1810-1818, Sept. 1999.
13. F. Ling, J. M. Song, and J. M. Jin, "Multilevel fast multipole algorithm for analysis of large-scale microstrip structures," *Microwave Guided Wave Lett.*, accepted for publication.

14. F. Ling, K. Donepudi, and J. M. Jin, "Higher-order full-Wave analysis of multilayer microstrip structures," *Microwave Opt. Tech. Lett.*, accepted for publication.
15. F. Ling and J. M. Jin, "Discrete complex image method for general multilayer media," *Microwave Guided Wave Lett.*, submitted for publication.

Conference Presentations

1. D. G. Fang, F. Ling, and Y. Long, "Rectangular waveguide Green's function involving complex images," *IEEE Antennas and Propagation Society International Symposium*, Newport Beach, CA, 1995.
2. F. Ling and D. G. Fang, "Bandwidth enhancement of proximity-coupled microstrip antennas with an airgap," *China-Japan Joint Meeting on Microwave*, Hefei, China, 1996.
3. F. Ling, X. Q. Sheng, and J. M. Jin, "Hybrid MoM/SBR and FEM/SBR methods for scattering by large bodies with inhomogeneous protrusions," *IEEE Antennas and Propagation Society International Symposium*, Montreal, Canada, 1997.
4. J. M. Jin, G. X. Fan, F. Ling, C. C. Lu, J. M. Song, and W. C. Chew, "A hybrid SBR/MoM technique for analysis of scattering from small protrusions on a large conducting surface," *Progress in Electromagnetic Research Symposium*, Ridgefield, CT, July 1997.
5. C. F. Wang, F. Ling, and J. M. Jin, "A BCG-FFT solution for scattering and radiation by large finite arrays of microstrip antennas," *The 14th Annual Review of Progress in Applied Computational Electromagnetics*, Monterey, CA, 1998.
6. J. M. Jin, F. Ling, S. T. Carolan, J. M. Song, W. C. Gibson, W. C. Chew, C. C. Lu, and R. Kipp, "A hybrid SBR/MoM technique for analysis of scattering from small protrusions on a large conducting body," *IEEE Antennas and Propagation Society International Symposium*, Atlanta, GA, 1998.

7. F. Ling, C. F. Wang, and J. M. Jin, "Application of adaptive integral method to scattering and radiation analysis of arbitrarily shaped planar structures," *IEEE Antennas and Propagation Society International Symposium*, Atlanta, GA, 1998.
8. F. Ling, C. F. Wang, and J. M. Jin, "An efficient algorithm for analyzing large-scale microstrip structures using adaptive integral method combined with discrete complex image method," *International Conference on Microwave and Millimeter Wave Technology*, Beijing, China, 1998.
9. F. Ling, J. M. Jin, D. G. Fang, and N. Feng, "Electromagnetic modeling of microstrip structures in multilayer media," *The 14th Annual Review of Progress in Applied Computational Electromagnetics*, Monterey, CA, 1999.
10. F. Ling, D. Jiao, and J. M. Jin, "Efficient electromagnetic modeling of microstrip structures in multilayer media," *IEEE Antennas and Propagation Society International Symposium*, Orlando, FL, 1999.
11. C. F. Wang, F. Ling, J. M. Song, and J. M. Jin, "A fast algorithm for solving CFIE of EM scattering," *IEEE Antennas and Propagation Society International Symposium*, Orlando, FL, 1999.
12. D. Jiao, F. Ling, and J. M. Jin, "Fast electromagnetic analysising using the asymptotic wavesforms evaluation method," *International Conference on Electromagnetism on Advanced Application*, Torino, Italy, 1999.
13. F. Ling, K. Donepudi, and J. M. Jin, "Higher-order electromagnetic modeling of multilayer microstrip structures," *The 16th Annual Review of Progress in Applied Computational Electromagnetics*, Monterey, CA, 2000.